CHALMERS
UNIVERSITY OF TECHNOLOGY

Early-Age Behaviour of Post-Tensioned Low-CO_2 and Fibre-Reinforced Concrete

An Experimental Study Using Distributed Optical Fibre Sensing

Master's Thesis in the Master's Programme Structural Engineering and Building Technology

ELISABETH BRUHN
STINA DURLING

DEPARTMENT OF ARCHITECTURE AND CIVIL ENGINEERING
DIVISION OF STRUCTURAL ENGINEERING

CHALMERS UNIVERSITY OF TECHNOLOGY

Master's thesis ACEX30
Gothenburg, Sweden 2026

MASTER'S THESIS ACEX30

Early-Age Behaviour of Post-Tensioned Low-CO_2 and Fibre-Reinforced Concrete

An Experimental Study Using Distributed Optical Fibre Sensing

Master's Thesis in the Master's Programme Structural Engineering and Building Technology

ELISABETH BRUHN
STINA DURLING

Department of Architecture and Civil Engineering
Division of Structural Engineering
CHALMERS UNIVERSITY OF TECHNOLOGY
Gothenburg, Sweden 2026

Early-Age Behaviour of Post-Tensioned Low-CO_2 and Fibre-Reinforced Concrete
An Experimental Study Using Distributed Optical Fibre Sensing
Master's Thesis in the Master's Programme Structural Engineering and Building Technology

ELISABETH BRUHN
STINA DURLING

Supervisor: Ignasi Fernandez, Architecture and Civil Engineering
Daniel Ekström, WSP Sverige AB
Examiner: Rasmus Rempling, Architecture and Civil Engineering

Examensarbete ACEX30
Institutionen för Arkitektur och Samhällsbyggnadsteknik
Chalmers Tekniska Högskola, 2026

Department of Architecture and Civil Engineering
Division of Structural Engineering
Chalmers University of Technology
SE-412 96 Göteborg
Sweden
Telephone +46 31 772 1000

Cover: Monitoring of the three concrete specimens in Chalmers construction laboratory.

Department of Architecture and Civil Engineering
Göteborg, Sweden, 2026

Early-Age Behaviour of Post-Tensioned Low-CO_2 and Fibre-Reinforced Concrete
An Experimental Study Using Distributed Optical Fibre Sensing

Master's thesis in the Master's Programme Structural Engineering and Building Technology

ELISABETH BRUHN

STINA DURLING

Department of Architecture and Civil Engineering
Division of Structural Engineering
Chalmers University of Technology

ABSTRACT

The construction industry is under increasing pressure to reduce its environmental impact, driving the development of low-carbon concrete solutions. In parallel, prestressed concrete systems provide opportunities for improved material efficiency, while the inclusion of fibre-reinforced concrete in forthcoming Eurocode provisions promotes hybrid reinforcement strategies aimed at enhancing structural performance at the serviceability limit state. Utilizing distributed optical fibre sensing (DOFS) could help optimize structural designs.

The combined use of climate-improved concrete, fibre reinforcement, and post-tensioning still lacks comprehensive experimental validation. This study addresses this gap through an experimental investigation of the static and long-term behaviour of post-tensioned concrete beams with different concrete compositions. Particular focus is placed on time-dependent effects such as creep, shrinkage, and relaxation, analysed using DOFS and compared with analytical predictions according to Eurocode 2.

Three beam specimens were tested: a conventional reference beam, a low-CO_2 concrete beam, and a fibre-reinforced low-CO_2 concrete beam. All beams were cast using self-compacting concrete, where part of the Portland cement was replaced with ground granulated blast-furnace slag in the low-CO_2 mixes.

The results show consistent structural behaviour with expected prestress losses and deformation patterns. The low-CO_2 and fibre-reinforced concretes exhibited smaller long-term deformations than the conventional concrete, indicating reduced creep behaviour. In addition, the DOFS system accurately captured both the strain development and the overall structural response during tensioning and long-term monitoring.

The findings indicate that reduced cement content can provide comparable or improved structural performance when time-dependent behaviour is considered. Furthermore, the analytical predictions according to Eurocode 2 tended to overestimate the long-term prestress losses compared with the experimental observations, highlighting the conservative nature of the code-based approach.

Key words: Low CO_2-concrete, Fibre-reinforced concrete, Post-tension, Distributed Optical Fibre Sensing (DOFS), Prestress losses, Creep, Shrinkage, Relaxation

Tidigt beteende hos efterspänd klimatförbättrad- och fiber armerad betong
En experimentell studie utförd med distribuerade optiska fibersensorer

Examensarbete inom masterprogrammet Konstruktionsteknik och byggnadsteknologi

ELISABETH BRUHN

STINA DURLING

Institutionen för arkitektur och samhällsbyggnadsteknik
Avdelningen för Konstruktionsteknik
Chalmers tekniska högskola

SAMMANFATTNING

Byggbranschen står inför ett växande behov av att minska sin klimatpåverkan, vilket driver utvecklingen av mer hållbara betonglösningar med lägre koldioxidutsläpp. Samtidigt skapar efterspända betongkonstruktioner möjligheter till ökad materialeffektivitet, medan distribuerad optisk fibersensorik (DOFS) kan bidra till förbättrad förståelse av konstruktioners beteende.

Den kombinerade användningen av klimatförbättrad betong, fiberarmering och efterspänning saknar fortfarande omfattande experimentell verifiering. Denna studie undersöker därför det statiska och långsiktiga beteendet hos efterspända betongbalkar med olika betongsammansättningar. Fokus ligger på tidsberoende effekter såsom krypning, krympning och relaxation, analyserade med hjälp av DOFS och jämförda med analytiska beräkningar enligt Eurokod 2.

Tre balkar undersöktes: en konventionell referensbalk, en balk av låg-CO_2-betong samt en fiberarmerad låg-CO_2-betongbalk. Samtliga balkar tillverkades med självkompakterande betong där Portlandcementet delvis ersattes med masugnsslagg i låg-CO_2-betongerna.

Resultaten visar ett konsekvent strukturellt beteende med förväntade förspänningsförluster och deformationsmönster. Låg-CO_2- och fiberarmerade betongerna uppvisade mindre långsiktiga deformationer än den konventionella betongen, vilket indikerar minskad krypning. Resultaten visar dessutom att DOFS-systemet med hög noggrannhet kan registrera både töjningsutvecklingen och balkarnas övergripande strukturella respons under både uppspänning och långtidsmätningar.

Studien visar att en reducerad cementhalt kan ge jämförbar eller förbättrad strukturell prestanda när tidsberoende effekter beaktas. De analytiska prediktionerna enligt Eurokod 2 tenderade dessutom att överskatta de långsiktiga förspänningsförlusterna jämfört med de experimentella resultaten, vilket belyser den konservativa karaktären hos de normbaserade beräkningsmodellerna.

Nyckelord: Låg-CO_2-betong, fiberarmerad betong, efterspänning, distribuerad optisk fibersensorik (DOFS), förspänningsförluster, krypning, krympning, relaxation

Preface

This master's thesis was carried out at the Department of Architecture and Civil Engineering at Chalmers University of Technology during the spring of 2026. The work was conducted as a part of a research project supported by Svenska Byggbranschens Utvecklingsfond (SBUF). The experimental work was conducted in the Structures lab at Chalmers, and the Thesis was a cooperation between Chalmers and WSP.

Firstly, we want to express our sincere gratitude to our examiner Rasmus Rempling and our supervisor Daniel Ekström, for their valuable guidance insightful discussions and continuous support throughout the project and invite to India. We also want to extend our deepest thanks to our second supervisor, Ignasi Fernandez and offer a sincere apology for not always bringing fika to our meetings.

The assistance provided by Sebastian Almfeldt, Anders Karlson and Bruno Gonçalves, at the Structures Lab is gratefully acknowledged. We are thankful for their support during the experimental setup and especially for the orange caps. In connection with the experimental work, we want to thank Shea Hagy for teaching us how to use a circular saw with confidence and August Jansson for selecting pink and raspberry red colored connections for the distributed optical fibre sensing.

We also want to thank the work group for the SBUF-project, consisting of David Fall, Ingemar Löfgren, Rasmus Rempling, Ignasi Fernandez for their support and input throughout the spring. And the refrence-group, consisting of Alexander Kjellgren, Martin Laninge, Siri Salander and Daniel Ekström for their input during the meetings.

Finally, we want to thank everyone who are involved in the project in one way or another. Special thanks are extended to David Dackman for saving us with your Mathcad calculations, Carlos Gil Berrocal for always responding to emails fast and chitchatting on the 4th floor, the Bridge Department at WSP in Gothenburg for always knocking at the door when it is time for fika and our opponent group, Matilda Dahlgren and Ellen Nyholm, for letting us stay in Krabban even though they booked it.

This thesis marks the completion of our master's studies in Structural Engineering and Building Technology at Chalmers University of Technology.

Elisabeth Bruhn
Stina Durling
Gothenburg, June 2026

Notations

Acronyms

DOFS	Distributed optical fibre sensor
FRP	Fibre-reinforced polymer
GGBFS	Ground granulated blast-furnace slag
SCC	Self compacting concrete
SCM	Supplementary cementitious materials
SHM	Structural health monitoring

Roman upper case letters

A_c	Concrete cross-sectional area
A_p	Prestressing steel area
E	Modulus of elasticity
E_c	Modulus of elasticity of concrete
E_{cm}	Secant modulus of elasticity of concrete
E_p	Modulus of elasticity of prestressing steel
E_t	Modulus of elasticity of concrete at specific time
EI	Flexural stiffness of the cross-section
I_c	Moment of inertia of the concrete cross-section
$M(x,t)$	Bending moment
$P(x,t)$	Post-tensioning force
P_i	Initial prestressing force
$P_i(0)$	Tensioned force at active end
$P_i(s)$	Tendon force accounting for friction loss at distance s
ΔP	Pretensioning force loss

Roman lower case letters

$e(x)$	Tendon eccentricity along the beam
$f_{cm.cube.t}$	Compressive cube strength at a specific day
$h_{0,beam}$	Notional size of the beam cross-section
$h_{0,cyl}$	Notional size of the cylinder cross-section
k	Unintended angular displacement per unit length (wobble coefficient)
k_{β_c}	Ratio of creep development functions
$k_{notional}$	Ratio of notional creep
k_{φ}	Ratio of 50 year creep coefficients
s	Length of the duct from the active end to the section under consideration
t	Time
t_0	Age of concrete at loading
x	Position along the beam
$y(x,t)$	Vertical deflection of the beam
z	Vertical distance between top and bottom fibres

Greek lower case letters

α	Change of slope over a distance s
$\beta(t, t_0)$	Time function of the creep coefficient
$\beta_{as}(t)$	Time function of autogenous shrinkage
$\beta_{ds}(t)$	Time function of drying shrinkage
$\Delta\varepsilon_{DOFS}$	Change in strain measured by DOFS
$\varepsilon_{bottom(x,t)}$	Measured strain in the bottom fibre
$\varepsilon_{c,creep}$	Creep strain
$\varepsilon_{ca}(t)$	Autogenous hrinkage strain
$\varepsilon_{cd}(t)$	Drying shrinkage strain
$\varepsilon_{creep,beam}$	Beam creep strain
$\varepsilon_{cs}(t)$	Total shrinkage strain
$\varepsilon_{cs,beam}(t)$	Total shrinkage strain in the beam
$\varepsilon_{cs,cyl}(t)$	Total shrinkage strain in the cylinder
$\varepsilon_{el,beam}$	Elastic strain
$\varepsilon_{top}(x, t)$	Measured strain in the top fibre
$\theta(x, t)$	Rotation of the beam section
μ	Frictional coefficient
μ	Initial tensile strength of prestressing steel
σ_c	Concrete stress
σ_{cpi}	Initial concrete stress at prestressing steel level
σ_{pi}	Initial stress in prestressing steel
$\varphi(t, t_0)$	Creep coefficient
φ_0	Notional creep coefficient
$\varphi_{creep,EC}$	Creep coefficient calculated for the beam with Eurocde 2
$\varphi_{EC,beam}$	Creep coefficient derived for the beam with Eurocde 2
$\varphi_{EC,cyl}$	Creep coefficient derived for the cylinder with Eurocde 2
$\varphi_{exp,beam}$	Creep coefficient obtained from the measured beam strains
$\varphi_{exp,cyl}$	Creep coefficient obtained from the measured cylinder strains
$\chi(x, t)$	Curvature of the beam section
χ_{1000}	Relaxation loss after 1000 h
χ_t	Relaxation factor

Contents

1 Introduction

This project aims to experimentally investigate the static and long-term behaviour of post-tensioned beams in fibre-reinforced and low-CO_2 concrete. As the construction industry faces increasing demands for sustainable infrastructure, extended service life, and more efficient construction processes, new binders and reinforcement strategies are becoming essential. The thesis was conducted within the funded research project 14562 from Svenska Byggbranschens Utvecklingsfond (SBUF) and continues the research of SBUF-project 14134.

The experimental program includes three post-tensioned concrete beams with varying configurations. Advanced strain-monitoring techniques, distributed optical fibre sensors (DOFS), are used to capture detailed structural responses and enable meaningful comparisons between the different systems.

1.1 Background

Prestressed concrete has played an important role in structural engineering since the early twentieth century, when the technique was first developed to overcome the limitations of ordinary reinforced concrete (Collins and Mitchell, 1991). By introducing a controlled compressive force into the concrete, prestressing improves the material's ability to resist tensile stresses. This results in several advantages, such as reduced cracking, smaller deflections under load, the possibility of longer spans and a more efficient use of materials. These benefits have made prestressed concrete a widely used solution in bridges, buildings, and other large-scale infrastructure (Berrocal et al., 2025).

Both fibre reinforcement and post-tensioning are well-established methods for enhancing the performance of concrete structures, although they are not commonly used together (Mathern et al., 2024). Fibre reinforcement helps limit crack formation and propagation by distributing stresses more evenly throughout the material (Almgren et al., 2018). It can also improve toughness, impact resistance, and durability. The inclusion of fibre-reinforced concrete in the latest generation of the Eurocode 2 is expected to encourage broader adoption of combined reinforcement strategies (de la Fuente et al., 2023).

At the same time, the development of alternative and more sustainable construction materials is progressing (Monteiro et al., 2017). Low-CO_2 concrete is becoming increasingly important as the industry seeks to reduce its environmental impact. However, the combination of low-CO_2 concrete with post-tensioning systems is still relatively unexplored, and there is limited practical experience regarding their interaction (Mathern et al., 2024). As the demand for sustainable infrastructure continues to grow, understanding how these materials perform together will be beneficial.

To support such investigations, advanced monitoring techniques are becoming increasingly relevant (Fernandez et al., 2025). Distributed optical fibre sensors (DOFS) allow continuous measurement of strain along the entire length of a member, offering a level of detail that conventional sensors cannot provide (Berrocal et al., 2025). Their small size, low weight, and resistance to chemical and electromagnetic interference make them well suited for embedding in concrete structures.

1.2 Purpose

The purpose of this thesis was to investigate the static and long-term behaviour of post-tensioned concrete beams combining low-CO_2 concrete, fibre reinforcement, and post-tensioning. Particular focus is placed on the effects of creep, shrinkage, and prestress losses within the post-tensioning system to see how it effects the long term force loss.

1.3 Goals

The goal of this thesis is to examine the structural response of post-tensioned beams in order to evaluate how concrete composition and fibre reinforcement influence long-term performance. Another objective is to compare the experimental results with analytical predictions based on Eurocode 2.

By improving the understanding of these material interactions and evaluating the accuracy of current design methods, this research aims to contribute to the development and implementation of more sustainable concrete structures with reduced carbon footprint.

1.4 Limitations

The scope of this project is subject to several constraints. First, the study is bound by the timeframe of the master's thesis, consequently, the long-term data on the lifespan of the beams is restricted to the available testing period. Second, the number of physical specimens is limited by laboratory capacity and production schedules. Third, the calculations are performed based on Eurocode 2 (EN 1992-1-1:2004) if nothing else is specified. Finally, the research is conducted within a fixed budget provided by SBUF limiting the amount of test specimens that could be tested.

1.5 Scientific Approach

To achieve the goal of this study, a structured scientific approach is adopted. The work is divided into three main phases: design, experimentation, and analysis. The workflow of these phases are visually presented in Figure 1.1.

The design phase aims to determine a beam cross-section suitable for experimental testing, taking into account laboratory constraints as well as ultimate limit state requirements. Although the final failure test is conducted outside the scope of this master's thesis, the beams are designed to satisfy these requirements. The design is carried out using analytical calculations in accordance with the Eurocode 2.

The experimental phase focuses on obtaining both short-term (static) and long-term response data. Measurements are carried out using fibre optic sensors, complemented by material testing to determine key properties such as concrete compressive strength and modulus of elasticity. A creep and shrinkage test is also performed to obtain the long-term creep and shrinkage behavior of the concrete.

The post-processing and analysis phase involves interpreting the experimental results and comparing the performance of the different specimens. The results are also assessed against the analytical predictions established during the design phase in order to evaluate the accuracy of the applied design methods.

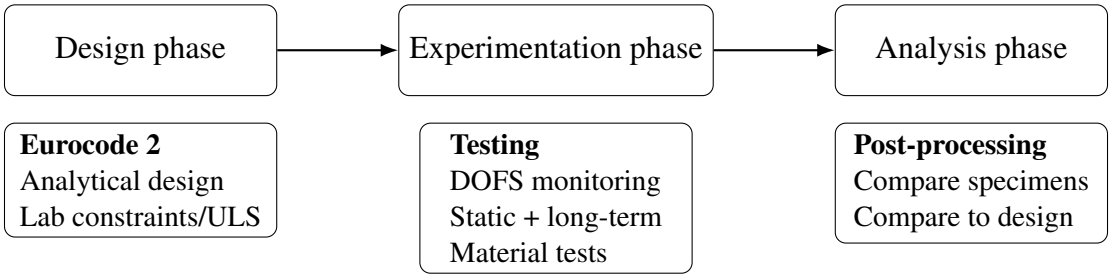

Figure 1.1: Scientific approach and main phases of the study.

2 Theoretical framework

The theoretical framework presented in this section provides the fundamental background relevant to the study. It introduces the key properties and behavior of concrete and steel, with particular emphasis on low-CO_2 concrete and fibre-reinforced concrete, as well as reinforcement and prestressing steel.

Furthermore, the section outlines the principles of prestressing and post-tensioning, followed by a description of the long-term behavior of concrete structures, including creep, shrinkage, and relaxation effects. Finally, an overview of structural health monitoring (SHM) using fiber optic techniques is presented, as this forms an important part of the experimental investigation.

2.1 Concrete

Concrete is one of the most widely used construction materials and plays a central role in modern infrastructure due to its versatility and high compressive strength (Al-Emrani et al., 2013). However, it is inherently brittle and has low tensile capacity, which necessitates reinforcement in structural applications. In addition, conventional concrete production has a significant environmental impact, mainly due to the CO_2 emissions associated with cement manufacturing .

To address these challenges, ongoing development focuses both on reducing the climate impact of concrete and improving its mechanical performance. Low-CO_2 concrete aims to decrease emissions by partially replacing clinker with supplementary cementitious materials (SCM) (Monteiro et al., 2017), while fibre-reinforced concrete enhances tensile behavior, crack control, and ductility through the addition of fibres (Singh, 2016).

The consistency of concrete can be adjusted depending on the desired properties. Self-compacting concrete (SCC) is one of the more flowable types of concrete (Almgren et al., 2018). SCC consolidate under its own weight without vibration. This facilitates the casting process and is particularly beneficial for fibre-reinforced concrete, as it promotes uniform fibre distribution and reduces the risk of defects.

2.1.1 Low-CO_2 Concrete

Concrete has a high environmental impact mainly because of the cement. The production of ordinary Portland cement causes substantial CO_2 emissions, primarily from the calcination of limestone and from fuel combustion during clinker production (Monteiro et al., 2017). As global cement demand is expected to continue increasing, reducing the clinker content in concrete is an important strategy for lowering the climate impact of the construction sector (Svensk Betong, 2025).

One way to reduce these emissions is to replace part of the Portland cement with supplementary cementitious materials (SCM), such as ground granulated blast-furnace slag (GGBFS) or fly ash (Monteiro et al., 2017). These materials can partially substitute the clinker and thereby reduce the embodied CO_2 of the binder system.

In the Swedish context, Svensk Betong (2025) defines climate-improved concrete as concrete with at least 10% lower climate impact than a reference concrete with the same function. Depending on the reduction level, climate-improved concrete is commonly classified into different levels, 1 to 4, where higher levels correspond to a larger share

of alternative binders and a lower CO_2 footprint (Svensk Betong, 2025).

An example of a sort of slag used as a SCM is Slag Bremen that is used in concrete mixes by Thomas Concrete. According to Thomas Concrete Group (2022), Slag Bremen has a significantly lower CO_2 equivalent per ton than ordinary cement, illustrating the climate benefit of clinker replacement. The reported CO_2 equivalent for Slag Bremen is 62 kg/tons, compared to 759 kg/tons for ordinary Portland-limestone cement.

Replacing Portland cement with GGBFS generally increases setting time and reduces early-age strength, because slag hydrates more slowly than ordinary cement. However, later-age strength often develops more favorably, and slag concrete may eventually match or exceed the strength of ordinary Portland cement concrete (Belie et al., 2018). This means that the use of slag must be considered both as a climate-reducing measure and as a mix-design variable that affects workability, early strength, and curing requirements (Thomas Concrete Group, 2022).

2.1.2 Fibre-Reinforced Concrete

Fibre-reinforced concrete is concrete with fibres added to the concrete mix. It could be fibres of steel, glass or plastic (Almgren et al., 2018). The incorporation of fibres enhance the ductility and the resistance of the concrete. Steel fibres are particularly effective as they distribute cracks and provide post-cracking load carrying capacity.

Concrete is a brittle material with low tensile strength and strain capacity under tension (ACI Committee 544, 2001). This is traditionally overcome by adding reinforcing bars or prestressing steel. Instead, or additionally, fibres can be mixed randomly, but uniformly, into the concrete to improve performance under both quasi-static loads and dynamic loads such as fatigue, shock, and impact (Singh, 2016). The random positioning of fibers around coarse aggregates forms a truss structure where fibres act as tension ties and the mortar matrix serves as compression struts. Fibers embedded in the mortar matrix carry the induced tensile forces while the concrete matrix handles compression and distribute internal tensile forces to the fibres.

Adding steel fibres to the concrete mix provides several advantages. Their random distribution throughout the concrete volume, at much closer spacing than practical for reinforcing bars, promotes distributed cracking with reduced crack widths (ACI Committee 544, 2001). The first crack also appears at an increased tensile strength as well as an increased ultimate limit strength. The shear friction strength is also improved through resistance to fibre pullout and the fibres bridging the cracks. Steel fibre also reduce the adverse effect of shrinkage cracking since they allow multiple cracking to occur, transfer tensile stresses across cracks and enable long-term stress transfer that permits healing or sealing of the cracks.

2.2 Steel in Concrete Structures

Steel is commonly used in concrete structures to compensate for the relatively low tensile capacity of concrete while taking advantage of its high compressive strength (Al-Emrani et al., 2013). Through composite action between steel and concrete, structural members can efficiently resist both tensile and compressive stresses while maintaining ductility and crack control. In reinforced and prestressed concrete systems, steel is generally categorized into passive reinforcement and active prestressing steel. Passive reinforcement primarily carries tensile stresses after cracking and contributes to

structural ductility, whereas prestressing steel introduces compressive stresses into the member before external loading is applied. The mechanical properties and behaviour of these steel types differ significantly and influence both the short-term and long-term response of concrete structures.

2.2.1 Reinforcement

Reinforcement is used to provide ductility and crack control in structural members (Almgren et al., 2018). In conventional reinforced concrete structures, reinforcement resists tensile stresses caused by external loading, temperature variations, and shrinkage. Reinforcement also contributes to load transfer, crack control, and structural durability. Load-carrying reinforcement may be placed in regions subjected to tension or compression, while shear reinforcement is commonly provided in the form of stirrups.

Reinforcing steel is typically manufactured as hot-rolled or cold-formed steel, where hot-rolled steel is more commonly used for reinforcing bars (Al-Emrani et al., 2013). The mechanical behaviour of steel can be described by its stress–strain relationship, shown in Figure 2.1. Both steel types initially exhibit elastic behaviour at low stress levels. Hot-rolled steel displays a distinct yield plateau followed by significant plastic deformation before failure, providing ductile behaviour. In contrast, cold-formed steel shows a more gradual transition without a pronounced yield plateau and generally exhibits lower ductility.

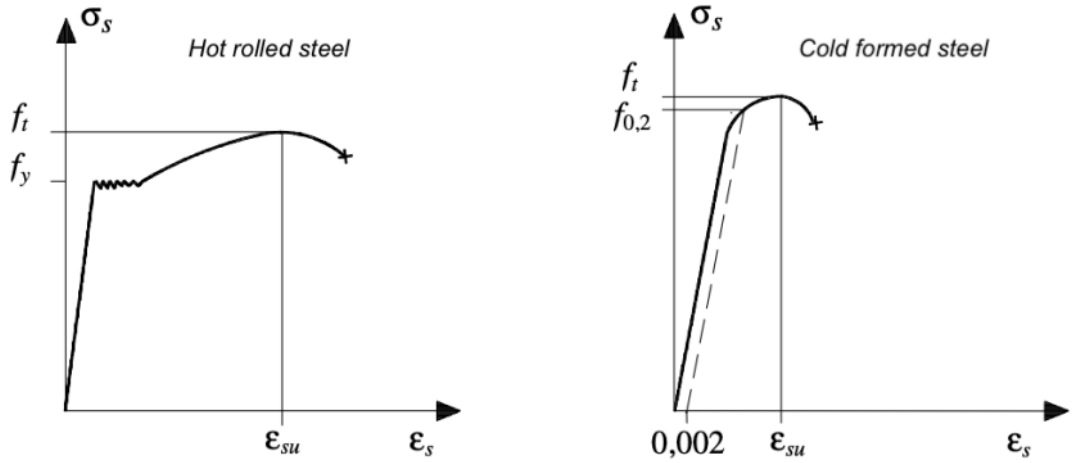

Figure 2.1: Stress-strain relation for hot rolled and cold formed steel. Figure from Al-Emrani et al. (2013)

Typical reinforcing steel grades, such as B500, have a yield strength of approximately 500 MPa and sufficient elongation capacity to ensure ductile structural performance (Al-Emrani et al., 2013). The ductility of reinforcing steel is important in concrete structures, as it enables stress redistribution and provides warning before failure.

Reinforcing bars are commonly ribbed to improve bond characteristics and interaction between steel and concrete (Almgren et al., 2018). A reliable bond enables composite action between the materials, ensuring efficient force transfer and allowing the concrete and reinforcement to deform together under loading. The concrete cover is therefore important to provide sufficient anchorage and to prevent local concrete failure around

the reinforcement.

When a concrete member cracks, the reinforcement carries the tensile forces in the cracked regions (Al-Emrani et al., 2013). In prestressed concrete systems designed as fully prestressed members, passive reinforcement generally remains unstressed during service conditions since cracking is prevented (Engström, 2011). However, if cracking occurs, either in partially prestressed members or due to increasing load levels approaching ultimate limit state, the passive reinforcement becomes activated and carries tensile stresses similarly to conventional reinforced concrete members.

2.2.2 Prestressing Steel

Prestressing strands, also referred to as active steel, are manufactured from high-strength steel specifically developed to withstand high tensile stresses and sustain large initial stress levels over long periods of time (Collins and Mitchell, 1991; Engström, 2011). Unlike conventional reinforcing steel, prestressing steel is subjected to high stress levels during service and therefore requires specific mechanical properties such as high tensile strength and low relaxation characteristics.

Prestressing strands typically consist of seven high-strength wires twisted together into a strand configuration (Almgren et al., 2018; Collins and Mitchell, 1991; Engström, 2011). Depending on the steel grade, tensile strengths commonly range between 1800 – 2000 MPa, which is significantly higher than for conventional reinforcement. The high tensile capacity enables the application of large prestressing forces while limiting the required steel area.

The stress–strain relationship of prestressing steel differs from that of passive reinforcement, as illustrated in Figure 2.2. Prestressing steel exhibits an almost linear elastic response up to high stress levels and lacks a pronounced yield plateau (Engström, 2011). Consequently, failure occurs with limited plastic deformation compared with hot-rolled reinforcing steel. The absence of a clear yielding region is compensated by the high strength and controlled material properties required for prestressed applications.

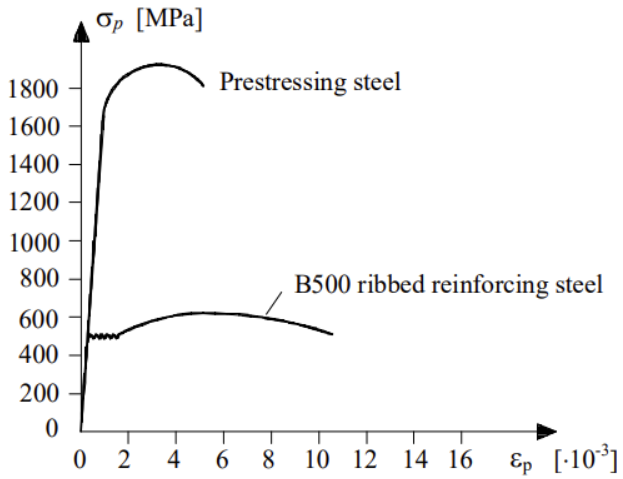

Figure 2.2: Stress-strain relation for prestressed steel and hot rolled passive steel. Figure from Engström (2011).

Prestressing strands are also characterized by their high modulus of elasticity and their time-dependent behaviour under sustained loading (Engström, 2011). When subjected to constant strain, the steel experiences relaxation, resulting in a gradual reduction of stress over time, as described in Section 2.4.3. To reduce these long-term effects, modern strands are commonly manufactured as low-relaxation steel.

Similar to passive reinforcement, prestressing strands may develop bond with the surrounding concrete along their length (Engström, 2011). This can be achieved through pretensioning or by grouting the duct in post-tensioned systems. Establishing a bond improves force transfer and reduces the risk of corrosion, thereby enhancing durability. Further details regarding prestressing systems are provided in Section 2.3.

Prestressing strands can be used in both post-tensioned and pretensioned systems and are specified in the European standard EN 10138 (Engström, 2011; European Committee for Standardization, 2009).

2.3 Prestressing of Concrete Structures

Compared with conventional reinforced concrete, prestressed concrete members provide several advantages, including improved crack control, reduced deflections, more slender structures, and enhanced material efficiency and prestressing enables longer spans (Berrocal et al., 2025; Fernandez et al., 2025). Prestressing is achieved by introducing compressive stresses into a concrete member prior to the application of external loads, thereby utilising the high tensile strength of prestressing steel (Collins & Mitchell, 1991). Since concrete exhibits high compressive strength but have relatively low tensile capacity, the induced compressive stresses improve structural performance by reducing tensile stresses under service conditions.

Two established methods are commonly used for prestressing: pretensioning and post-tensioning. In pretensioning, the prestressing steel is tensioned before casting the concrete, whereas in post-tensioning, the tendons are tensioned after the concrete has hardened (Engström, 2011). Prestressed members may be designed as fully prestressed systems, where cracking under service conditions is avoided, or as partially prestressed systems, where a limited amount of cracking is permitted. Although prestressing significantly improves serviceability performance, its influence on the ultimate load-carrying capacity is generally less pronounced (Al-Emrani et al., 2013).

The modern development of prestressed concrete is commonly attributed to the work of the French engineer Eugène Freyssinet, who introduced high-strength steel wire for prestressing concrete during the 1920s (Collins & Mitchell, 1991). Since then, prestressed concrete has become widely used in bridges, buildings, and other structural applications.

Prestressing is subjected to different time-dependent and instantaneous losses. These losses reduce the effective prestress force over the service life and need to be taken into consideration when designing. These losses include elastic shortening and long-term effects such as creep and shrinkage of concrete, friction between strands and duct, anchorage slip, as well as relaxation of the prestressing steel (Collins and Mitchell, 1991; Engström, 2011).

2.3.1 Post-Tensioning of Concrete

Post-tensioning introduces a compressive force into the concrete member to improve crack control and reduce deflections under service loading (Engström, 2011). In post-tensioned systems, the concrete member is cast with embedded ducts made of plastic or metal. The ducts are commonly arranged in a curved or parabolic profile to follow the bending moment distribution resulting from self-weight and external loading, thereby creating an eccentricity relative to the centroid of the cross-section, see Figure 2.3.

After the concrete has cured and reached sufficient strength, typically at least 70% of its 28-day strength, the prestressing tendons are pulled through the ducts and tensioned (Engström, 2011). Tensioning is performed using a hydraulic jack at the stressing end (active end), while the opposite end is fixed (passive end).

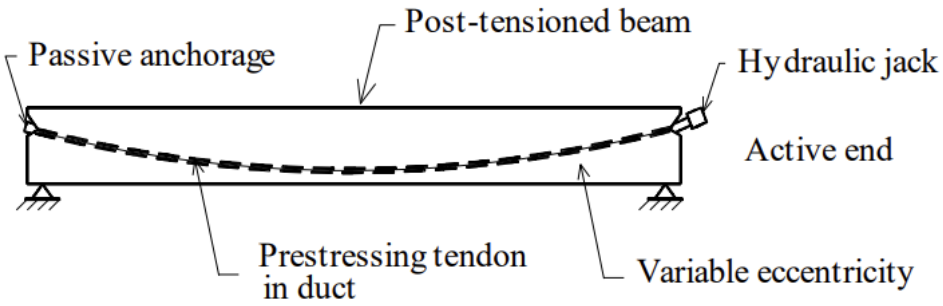

Figure 2.3: Post-tensioning system for a simply supported beam. Figure from (Engström, 2011).

Once the desired tendon force is reached, the tendon is anchored using wedges. The jack is removed and the beam is prestressed. The ducts may be either grouted or ungrouted. In grouted systems, the grout provides bond between the steel and concrete, enabling composite action, while also offering corrosion protection. It additionally pushes out possible water that may have entered the duct during construction (Almgren et al., 2018).

2.3.2 Losses due to Prestressing

Prestressed concrete members are subjected to both instantaneous and time-dependent prestress losses. Instantaneous losses occur during the stressing process and primarily consist of friction losses along the tendon, anchorage seating losses, and elastic shortening losses (Collins & Mitchell, 1991). Time-dependent losses develop gradually throughout the service life and mainly result from concrete creep, concrete shrinkage, and relaxation of the prestressing steel, as described in Section 2.4.

During stressing of the tendons, friction develops between the tendon and the surrounding duct (Collins & Mitchell, 1991). This friction reduces the prestressing force along the tendon length and depends on several factors, including duct curvature, unintended angular deviations (wobble effects), and the surface interaction between the tendon and duct, see Figure 2.4. As a result, the prestressing force decreases along the tendon and a non-uniform force distribution develops, with the largest losses occurring at the passive end.

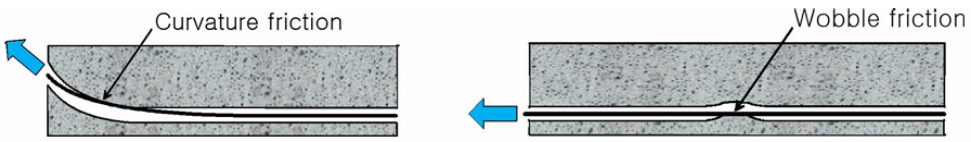

Fig. 1 Friction in a post-tensioning system.

Figure 2.4: Friction losses due to curvature and wobble losses. Figure from Jeon et al. (2015).

According to Eurocode 2, the tendon force accounting for friction loss is calculated as:

$$P_i(s) = P_i(0) \cdot e^{-\mu \cdot (\alpha + k \cdot s)} \tag{2.1}$$

where:

- $P_i(0)$ is the tensioned force,
- μ is the frictional coefficient,
- α is the change of slope over the distance s in radians, i.e. $\alpha(0)$-$\alpha(s)$,
- k is the unintended angular displacement per unit length (effect of wobble), and
- s is the the length of the duct from the active end to the section under consideration.

A study by Hong (2017) investigated repeated stressing of the same tendon and observed that repeated movement within the duct reduced friction between the tendon and the surrounding surface. Furthermore, friction losses may also be influenced by the interaction between adjacent strands within the same duct, resulting in different friction coefficients depending on strand position (Jeon et al., 2015). Therefore, both the friction coefficient and the contact conditions within the duct should be considered when estimating prestress losses.

Eurocode 2 provides recommended friction coefficients for different duct materials and tendon configurations. However, these values are primarily based on conventional stressing procedures where all tendons are tensioned simultaneously. Since simultaneous tensioning represents the standard approach in practice, limited information has been found regarding the influence of different tensioning sequences of multiple tendons on friction losses. Consequently, the effect of tendon stressing order on the resulting force distribution and friction behaviour remains insufficiently documented.

When the hydraulic jack is released after stressing, small movements of the anchorage wedges may occur, resulting in a reduction of the tendon force referred to as anchorage slip or seating loss (Engström, 2011). Additional prestress losses may also arise from local deformations within the anchorage zone, such as anchorage embedment into the surrounding concrete. The anchorage zone is subjected to high localized stresses, which may lead to splitting cracks and local concrete damage. Therefore, adequate reinforcement, commonly provided in the form of spiral reinforcement, is required to ensure sufficient confinement and load transfer.

Elastic shortening refers to the immediate shortening of the concrete member due to the compressive stresses introduced during prestressing. Collins and Mitchell (1991)

classify this as an instantaneous prestress loss. However, for post-tensioned systems, elastic shortening losses during stressing are often considered small because the tendons continue to be tensioned until the target prestress force is achieved which compensates for the shortening (Hong, 2017). Consequently, elastic shortening losses are generally of less significance in post-tensioned members compared with pretensioned systems.

2.4 Long-Term Behaviour of Prestressed Concrete

The long-term behavior of prestressed reinforced concrete is governed primarily by three time-dependent phenomena: creep and shrinkage of the concrete, and relaxation of the prestressing steel. These mechanisms act simultaneously and interact with each other, gradually altering the internal stress distribution and contributing to the total deformation of the structural member. Over time, these effects influence the prestress losses, deflection development, crack behavior, and ultimately the serviceability and durability of the structure.

2.4.1 Creep of Concrete

The stress–strain response of concrete is time-dependent and influenced by both the rate and history of loading (Almgren et al., 2018; Collins and Mitchell, 1991). When a constant stress is applied and maintained over time, the strain increases gradually. This phenomenon is known as creep. When a load is first applied, the resulting instantaneous deformation is referred to as the elastic strain. If the stress is sustained, additional strain develops over time and this is defined as the creep strain (Collins and Mitchell, 1991). Creep develops in the direction of the applied stress, meaning that concrete subjected to compression creeps by gradually shortening, while concrete in tension creeps by gradually elongating. To account for creep in structural analysis, it is common to consider a reduced effective stiffness, typically by modifying the modulus of elasticity.

Creep is composed of two components: basic creep and drying creep (Williams et al., 2024). Basic creep occurs under sealed conditions without moisture exchange, whereas drying creep develops when the concrete is allowed to dry and lose moisture to the surrounding environment. The similarity between the governing factors of creep and drying shrinkage indicates that internal moisture transport plays a key role in the creep mechanism (Engström, 2014). According to Williams et al. (2024), basic creep and drying creep should be considered separately for a more accurate estimation, like separating autogenous and drying shrinkage, but is describes together as a total creep in Eurocode 2 (EN 1992-1-1:2004). However, in the next generation of Eurocode (EN 1992-1-1:2023) the creep mechanisms are separated.

The magnitude of creep is commonly expressed as the creep coefficient, $\phi(t, t_0)$, where t is the time of interest and t_0 is the age of the concrete at the time of loading. If the load is applied at an early age, when the concrete is still maturing and has a lower stiffness, the resulting creep deformation will be substantially larger (Engström, 2014). In contrast, when loading occurs at a later age, such as after 28 days, the concrete has developed a higher modulus of elasticity and a more stable microstructure, resulting in reduced creep strains.

Several factors significantly influence creep, including (Engström, 2014; Almgren et al., 2018):

- the age of the concrete at loading (t_0),

- the magnitude and variation of the load,
- the composition and properties of the concrete,
- the ambient relative humidity, and
- the size and geometry of the structural element.

The creep coefficient develops gradually over time and is generally assumed to approach its final value after several decades, typically on the order of 70 years (Engström, 2014). The creep coefficient typically ranges between 1 and 3, with higher values often observed in dry environments, such as indoor conditions.

In structural members such as beams, this time-dependent creep behavior is observed as an increase in strain under sustained loading. According to Eurocode, the creep strain $\varepsilon_{c,creep}(t)$ can be expressed as:

$$\varepsilon_{c,creep}(t) = \varphi(t, t_0) \cdot \frac{\sigma_c}{E_c} \tag{2.2}$$

where:

- $\varphi(t, t_0)$ is the creep coefficient,
- σ_c is the concrete stress,
- E_c is the modulus of elasticity of concrete, and
- t_0 is the age of the concrete at loading.

The creep coefficient $\varphi(t, t_0)$, according to Eurocode 2, is calculated as

$$\varphi(t, t_0) = \beta(t, t_0) \cdot \varphi_0 \tag{2.3}$$

where:

- $\beta(t, t_0)$ is the time function of the creep coefficient, and
- φ_0 is the notional creep coefficient.

In a heavy reinforced member, with a steel to concrete ratio larger than normal, the reinforcement can reduce the creep strain (Williams et al., 2024). Having a bond between the prestressing steel and concrete, compared to an unbonded member, also reduce the creep.

In structural design, creep plays an important role in serviceability limit states. It contributes to increased long-term deflections, stress redistribution, and, in prestressed concrete structures, significant prestress losses. In practice, creep is typically estimated using prediction models provided in design standards such as Eurocode 2.

2.4.2 Shrinkage of Concrete

Concrete shrinkage is the time-dependent reduction in volume that occurs as concrete hardens and loses moisture (Almgren et al., 2018). This process initiates as the concrete hardens and continues to evolve over time, gradually approaching a final value. It consists of two main components: drying shrinkage and autogenous shrinkage (Engström, 2014). According to Eurocode 2, the total shrinkage strain $\varepsilon_{cs}(t)$ at a given age can be determined as:

$$\varepsilon_{cs}(t) = \varepsilon_{cd}(t) + \varepsilon_{ca}(t) \tag{2.4}$$

where:

- $\varepsilon_{cd}(t)$ is the drying shrinkage strain, and
- $\varepsilon_{ca}(t)$ is the autogenous shrinkage strain.

The drying shrinkage strain develops gradually over a long period and is governed by the exchange of moisture between the concrete and the surrounding environment (Engström, 2014). In normal-strength concrete, a significant portion of the mixing water does not participate in the hydration process but remains stored in the pore structure of the hardened concrete. When the concrete is exposed to an environment where drying can occur, this internal moisture is progressively lost, resulting in a reduction in volume, known as drying shrinkage (Collins and Mitchell, 1991).

The magnitude and rate of drying shrinkage are strongly influenced by the ambient relative humidity (Engström, 2014). Concrete placed in a dry environment will shrink more and at a faster rate compared to concrete in a humid environment. Additionally, the extent of exposed surface area plays an important role, as moisture transport occurs through these surfaces. Due to the generally low permeability of concrete, the drying process is slow and non-uniform across the cross-section. However, shrinkage models provided in design codes refer to the average shrinkage strain over the entire section.

According to Eurocode 2, the development of drying shrinkage strain can be determined as:

$$\varepsilon_{cd}(t) = \beta_{ds}(t) \cdot \varepsilon_{cd}(\infty) \tag{2.5}$$

where:

- $\beta_{ds}(t)$ is the time function of drying shrinkage, and
- $\varepsilon_{cd}(\infty)$ is the final value of drying shrinkage

Autogenous shrinkage, on the other hand, occurs without any moisture exchange with the surroundings (Engström, 2014). It develops as a result of the hydration process within the concrete and is most significant during the early stages after casting, approximately 50% of its final value is reached within the first 10 days after casting. Initially, hydration proceeds rapidly when sufficient water is available. Even after the concrete has hardened, unreacted cement remains and continues to hydrate using the internal moisture. This process leads to so-called chemical shrinkage. A notable effect of autogenous shrinkage is that the concrete becomes internally drier during the early period after casting. The final magnitude of autogenous shrinkage is generally assumed to depend linearly on the concrete strength class. According to Eurocode 2, its development can be expressed as:

$$\varepsilon_{ca}(t) = \beta_{as}(t) \cdot \varepsilon_{ca}(\infty) \tag{2.6}$$

where:

- $\beta_{ds}(t)$ is the time function of autogenous shrinkage, and
- $\varepsilon_{ca}(\infty)$ is the final value of autogenous shrinkage.

Furthermore, Svensk Byggtjänst (2017) describes plastic shrinkage as a mechanism that occurs in the early life of the concrete, while the material is still in its plastic state. It is driven by rapid evaporation of water from the surface, causing a reduction in volume. Plastic shrinkage is significantly greater than both drying shrinkage and autogenous shrinkage, and it can result in the formation of plastic shrinkage cracks on the surface. These cracks can be avoided by limiting evaporation from exposed surfaces immediately after casting. The GGBFS used to reduce CO_2 emissions is more sensitive to cracks from plastic shrinkage (Thomas Concrete Group, 2022).

2.4.3 Relaxation of Prestressing Steel

Relaxation is the phenomenon where the force required to maintain a highly stressed steel tendon at a constant elongation decreases over time (Collins & Mitchell, 1991). The relaxation losses are greatest immediately after tensioning and lessens progressively with time. It is estimated that approximately one-sixth of the total relaxation loss occurs within the first 10 hours.

In addition to relaxation, time-dependent effects in the concrete, creep and shrinkage, contribute to prestress losses (Collins & Mitchell, 1991). Both effects result in a shortening of the structure, which reduces the strain in the tendons and thereby lowers the prestressing force. At the same time, this shortening also reduces the rate of further relaxation in the steel.

Overall, the combined effects of relaxation, creep, and shrinkage typically lead to a reduction in prestressing force of approximately 15–20% over time (Al-Emrani et al., 2013; Engström, 2011). To compensate for these losses, tendons are initially tensioned to a higher force than the required effective prestress.

According to Eurocode 2, the relaxation factor for relaxation class 2 can be expressed as:

$$\chi_t = 0.66 \cdot \chi_{1000} \cdot e^{9.1 \cdot \mu} \cdot (\frac{t}{1000})^{0.75(1-\mu)} \cdot 10^{-3} \tag{2.7}$$

where:

- χ_t is the relaxation factor at time t,
- χ_{1000} is the relaxation loss after 1000h at 20 °C,
- μ is the initial tensile strength of the prestressing steel, and
- t is the time after tensioning.

The final value of relaxation is estimated at time 500 000 hours, ie 57 year.

2.5 Structural Health Monitoring Using Fibre Optics

Maintenance, repair, and replacement are essential to ensure the safety and long-term performance of civil engineering structures (Glišić & Inaudi, 2007). One way to do this is to monitor their behaviour. This is called structural health monitoring (SHM) and aims to provide in-time and reliable information about the condition of civil engineering structures so that damage or deterioration can be detected at an early stage (Glišić et al., 2013). The process consists of recording parameters that reflect the performance of the structure. Although SHM has many advantages, it is still not widely implemented in practice, as reliable, affordable, and scalable monitoring solutions remain limited.

One SHM method that have gained increasing attention in recent decades for strain and temperature monitoring in civil structures is distributed optical fibre sensors (DOFS) (Berrocal, Fernandez, & Rempling, 2021). A DOFS can be understood as a cable that is sensitive along its entire length, which means that one sensor can provide information over many points instead of only at a few discrete points (Glišić et al., 2013). This makes DOFS especially useful for large structures, since they can reduce the amount of wiring and allow more continuous monitoring than conventional sensor systems. Another advantage with DOFS compared to traditional sensors it that they are small, lightweight, resistant to corrosion and chemicals, and immune to electromagnetic interference (Berrocal, Fernandez, Bado, et al., 2021).

The sensing principle is based on light propagating through the fibre, where strain or temperature changes modify the optical signal that is scattered back to the interrogator (Glišić et al., 2013). Several scattering principles can be used in distributed sensing, namely Rayleigh, Brillouin, and Raman scattering. Rayleigh-based DOFS are particularly relevant in this context due to their high spatial resolution and suitability for detecting local strain changes. Rayleigh scattering occurs when light is elastically scattered by small variations in the refractive index and density inside the optical fibre (Berrocal, Fernandez, & Rempling, 2021). In Rayleigh-based DOFS, the backscatter pattern along the fibre is first recorded in an undisturbed reference state and then compared with later measurements. When the fibre is subjected to strain or temperature changes, the pattern shifts, and this shift can be converted into a strain response. The main advantage of this technique is its high spatial resolution, which can reach the sub-millimetre scale and makes it possible to identify local strain concentrations associated with cracks in reinforced concrete members.

Despite their advantages, distributed optical fibre sensors are inherently small and fragile, with a diameter typically ranging between 125 and 155 μm (Berrocal, Fernandez, Bado, et al., 2021). This means that the optical fibre are vulnerable to bending, local stress concentrations, and handling damage. To protect the thin and fragile optical fibre robust DOFS can be used instead. These have a protective coating that protects the glass core and reduces the risk of fibre breakage which makes them more suitable for reinforced concrete monitoring. They are also easier to install and more durable than thin fibres. According to Berrocal, Fernandez, Bado, et al. (2021), the robust DOFS still provided accurate measurements, and cracks could be identified as local peaks in the strain distribution. Another advantage was that they produced fewer strain reading anomalies, which are a known problem for thin fibres when they cross cracks. This means that robust DOFS can offer a more stable and practical solution when the main goal is reliable monitoring rather than maximum sensitivity.

3 Experimental Design and Testing

The methodology of this study was divided into three main stages: design, experimental work, and analysis. Each stage was structured to support the overall objective of evaluating the structural behaviour of the investigated beam specimens.

The first stage, the design phase, involved the design of a beam cross-section suitable for laboratory testing while satisfying the relevant ultimate limit state requirements. The design procedure was based on analytical calculations performed in accordance with Eurocode 2. Although destructive failure testing was not included within the scope of this thesis, the beams were designed to satisfy these design criteria.

The second stage, the experimental phase, comprised the experimental investigation of both short-term and long-term behaviour of the post-tensioned beam specimens. Three beams were considered: one with conventional concrete (P-RC), one with low-CO_2 concrete (P-RC^{CO_2}), and one with low-CO_2 fibre-reinforced concrete (P-FRC^{CO_2}). Strain measurements were obtained using fibre optic sensors, while additional material testing was conducted to determine important material properties, including concrete compressive strength and modulus of elasticity. A creep and shrinkage experiment was also performed to obtain creep and shrinkage strains.

The final stage, the post-processing and analysis phase, involved the processing and evaluation of the collected data. The experimental results were evaluated and compared between the different specimens, and the observed behaviour was further related to analytical predictions from the design stage to assess the applicability and accuracy of the chosen design methods.

3.1 Design Phase

This section presents the design methodology adopted for the dimensioning of the test specimens used in the experimental program. The designed was performed to ensure that the beams fulfill the practical laboratory constraints as well as the structural requirements necessary for the planned experimental testing. The design was conducted for conventional concrete and full calculations are provided in Appendix A.

Even though the beam dimensions are obtained through analytical calculations, they are presented here as part of the methodology, since they constitute essential input for the experimental program.

3.1.1 Design Requirements and Constraints

The design of the test specimens was governed by practical laboratory limitations, including a maximum beam length of 8.5 m and a maximum self-weight of 4.5 tons, in order to ensure that the beams could be safely handled and transported within the laboratory. In addition, the specimens were required to fail before a total applied load of 450 kN under four-point bending.

Although the final failure test lies outside the scope of this master's thesis, the specimens were designed to satisfy these criteria. This resulted in a required breaking load of 300 kN under four-point bending and a total beam length of 8.5 m, corresponding to an effective span of 8.0 m. The dimensioning of the beam was carried out in accordance with Eurocode 2, using analytical formulations presented in Engström (2011).

3.1.2 Cross Section and Reinforcement Layout

The final cross section that satisfied the requirements is presented in Figure 3.1. The specimens were designed with a total height of 640 mm and a total width of 320 mm.

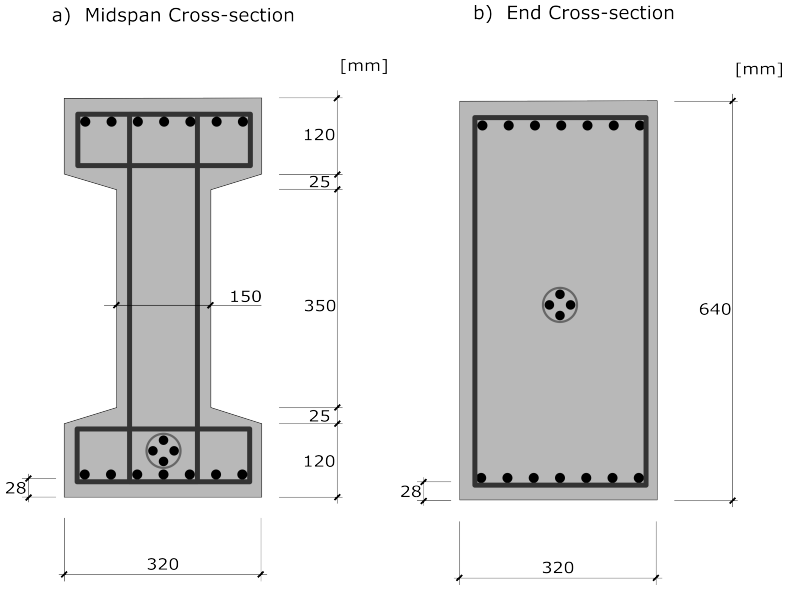

Figure 3.1: Beam cross section for a) the midspan and b) the end showing measurements and the reinforcement configuration including passive reinforcement, stirrups, tendons and duct.

For the passive reinforcement, B500B bars with a diameter of Φ16 were selected, with seven bars placed in both the top and bottom of the section. For the stirrups, Φ8 bars were used, arranged at a spacing of 260 mm. In the rectangular end regions, the stirrups are placed more closely to accommodate the increased forces in the anchorage zone. The stirrup layout is illustrated in Figure 3.2.

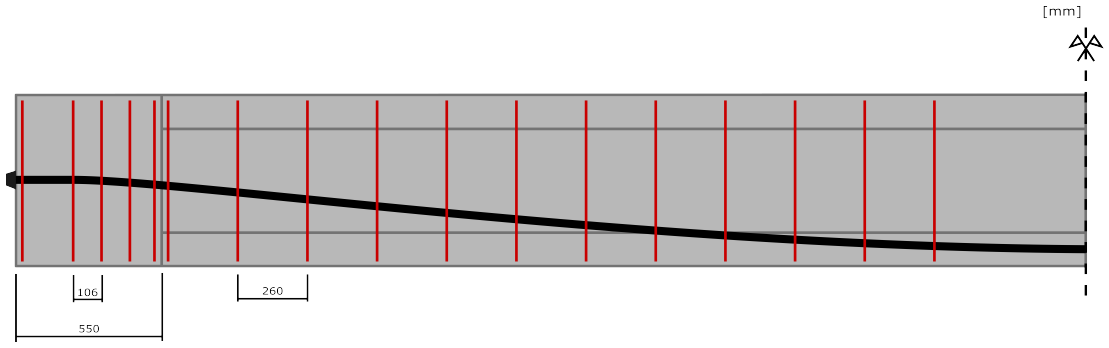

Figure 3.2: Stirrup placement and tendon profile along the beam. The stirrup placement is marked in red, while the tendon profile is shown in black.

3.1.3 Post-Tensioning Design

For post-tensioning, four steel tendons with a diameter of 15.2 mm were used, together with an XM20 anchorage system supplied by CCL and a corrugated plastic duct. The duct was shaped in a parabolic curve, see Figure 3.2, with the designed middle eccentricity of 230 mm.

For the dimensioning, each tendon was designed to be tensioned to a force of 160 kN, resulting in a total nominal prestressing force of 640 kN. The material properties of the prestressing steel tendons are summarised in Table 3.1, while the corresponding duct properties are presented in Table 3.2.

Table 3.1: Properties for 15.2 mm strand, steel designation Y1860S7 (CCL International, 2021).

Property	**Value**
Steel Designation	Y1860S7
Tensile Strength	1860 MPa
Nominal Diameter	15.2 mm
Steel Area	139 mm^2
Breaking Load F_m	259 kN
0.1% Proof Load $F_{p0.1}$	228 kN
Max Strand Load F_o	205 kN

Table 3.2: Duct properties for XM-20 plastic duct (CCL International, 2021).

Property	**Value**
Duct Inside Diameter	48 mm
Duct Outside Diameter	59 mm
Duct Wall Thickness	2 mm
Duct Area	1800 mm^2

3.1.4 Concrete Mixes

Three different concrete mixes were used in the experimental program, as summarized in Table 3.3. All mixes were supplied by Thomas Concrete and were designed with a maximum aggregate size of 8 mm, consistency class SF1, and a target strength class of C40/50. The use of consistency class SF1 implies that all concretes were produced as SCC, enabling proper casting and fibre distribution without the need for vibration.

Table 3.3: Summary of the concrete mixes used in the experimental program.

Concrete	**Strength class**	**Binder type**	**Dmax**	**Fibres**
P-RC	C40/50	CEM II/A-LL	8	—
P-FRC^{CO_2}	C40/50	Low-CO_2 binder	8	Steel fibres
P-RC^{CO_2}	C40/50	Low-CO_2 binder	8	—

The primary difference between the mixes lies in the binder composition. Two of the three mixes were produced as low-CO_2 concretes, P-RC^{CO_2} and P-FRC^{CO_2}, using a binder consisting of 50% CEM II/A–LL and 50% GGBFS of the type Slag Bremen. These mixes correspond to climate-improved concrete level 4 according to the Swedish classification introduced in Section 2.1.1. The remaining mix, P-RC was produced using conventional CEM II/A–LL cement and served as a reference concrete.

In addition, one of the low-CO_2 mixes, P-FRC^{CO_2}, contained steel fibres of type Dramix 4D 65/35. The hooked-end steel fibres were added at a dosage of 40.5 kg/m^3, while the remaining two mixes contained no fibres. Detailed concrete mix designs, including aggregate fractions and binder content, are provided in Appendix B.

3.2 Experiment Phase

The construction process was carried out in the Structures Lab at Chalmers University of Technology. Two formworks and three reinforcement cages were built. The Architecture workshop was used for cutting the plywood pieces. Both the formwork and the reinforcement were cut and assembled manually. The reinforcement drawings can be found in Appendix C and the form drawings can be found in Appendix D.

Together with the casting of the beams, small test specimens were cast to evaluate the compressive strength and modulus of elasticity of the concrete. Cubes were prepared for the compressive strength test, while cylinders were cast for the determination of the modulus of elasticity. All specimens were stored in water until testing. The tests were carried out at 3, 7, and 28 days after casting.

A long-term creep and shrinkage test was also conducted to obtain comparable creep and shrinkage strains to the results from the beams. The test started 29 days after casting and continued throughout the duration of the master's thesis.

3.2.1 Form and Reinforcement

The formwork was constructed from plywood and braced with timber studs. The two forms were built as one combined unit in order to reduce material usage and create a level surface, since the laboratory floor had a maximum inclination difference of approximately 2.5 cm. Parts of the formwork together with the reinforcement cage can be seen in Figure 3.3a.

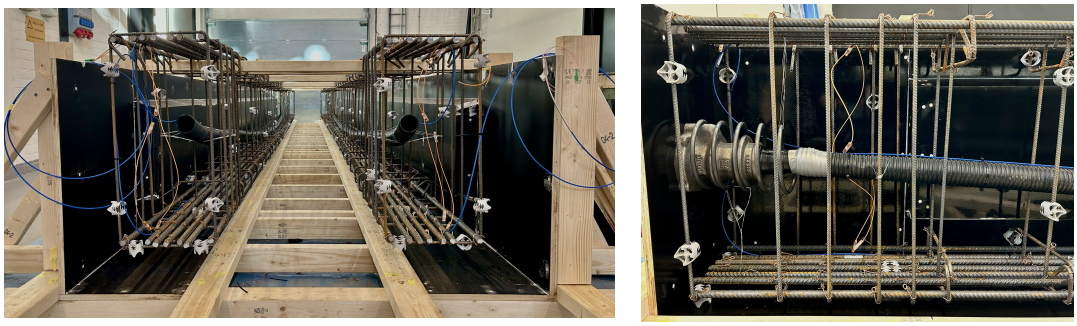

Figure 3.3: a) Form and reinforcement cage. b) Anchorage system XM20 from CCL attached in the form.

The stirrups consisted of three separate rectangular parts combined to form an I-shaped configuration. The passive reinforcement bars were tied together with the stirrups. In the anchorage zone, rectangular stirrups were used due to the rectangular geometry of the section.

Circular XM20 anchorages from CCL were attached to the side formwork panels together with spiral reinforcement to reduce local concrete failure, as described in Section 2.3.1. The anchorage system was connected to the duct, see Figure 3.3b. The duct was

placed within the reinforcement cages following a parabolic profile.

3.2.2 DOFS and Monitoring System Configuration

The structural response of the specimens was monitored using a distributed optical fibre sensing system. Strain measurements were acquired with an Optical Distributed Sensor Interrogator (ODiSI) 6000 series from Luna Inc., which has been based on Rayleigh backscattering and provides high-resolution distributed strain measurements along the fibre (Luna Innovations, 2022). The gauge pitch was 2.6 mm giving strain measurements every 2.6 mm along the fibre length.

A BRUsens DSS V9 sensing cable from Solifos was used as the optical fibre sensor. The cable has a fibre-in-Metal-Tube construction with an SS316L protective tube and an external polymeric sheath with a structured surface, which makes it robust and suitable for use in reinforced concrete applications (Solifos AG, 2025).

3.2.3 DOFS Placement

The DOFS were attached to the reinforcement system using zip ties. The fibres were positioned at the level of the top and bottom passive reinforcement bars, as well as on top of the duct, and were aligned along the longitudinal direction of the beam. The layout is illustrated in Figure 3.4, where the DOF is marked in blue.

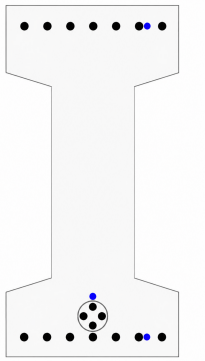

Figure 3.4: Cross-section of beam showing the placement of DOFS marked in blue, along the top and bottom reinforcement and on top of the duct.

To enable an accurate identification of the start and end of each sensor section along the beam, localized heat pinches were applied at the ends of the DOFS prior to data acquisition, see the orange cables in Figure 3.3. These heat pinches introduce distinct strain signatures in the recorded signals, which can be clearly identified in the post-processing phase.

3.2.4 Casting

The casting of the 3 specimens was performed at different occasions due to the different concrete mixes and the availability of only two forms. The curing time for the low-CO_2 concrete was longer than for the conventional concrete, which resulted in different schedules for formwork removal and post-tensioning. For the conventional concrete, the formwork removal and post-tensioning were carried out after 3 days of curing. For the low-CO_2 concretes, these operations were performed after 7 days of curing. For

the entirety of the experiment the beams were stored in the laboratory, with a mean temperature of 20.8°C and a mean relative humidity of 33%. The casting process and the storage during hardening is shown in Figure 3.5.

Simultaneously with the casting of each concrete beam, nine cubes, three small cylinders, and two large cylinders were cast, see Figure 3.5a. These specimens were used for the compressive strength tests, modulus of elasticity tests, and long-term cylindrical tests.

After casting, the exposed top surface of the concrete was covered with plastic wrap to reduce plastic shrinkage, as described in Section 2.4.2. This can be seen Figure 3.5b.

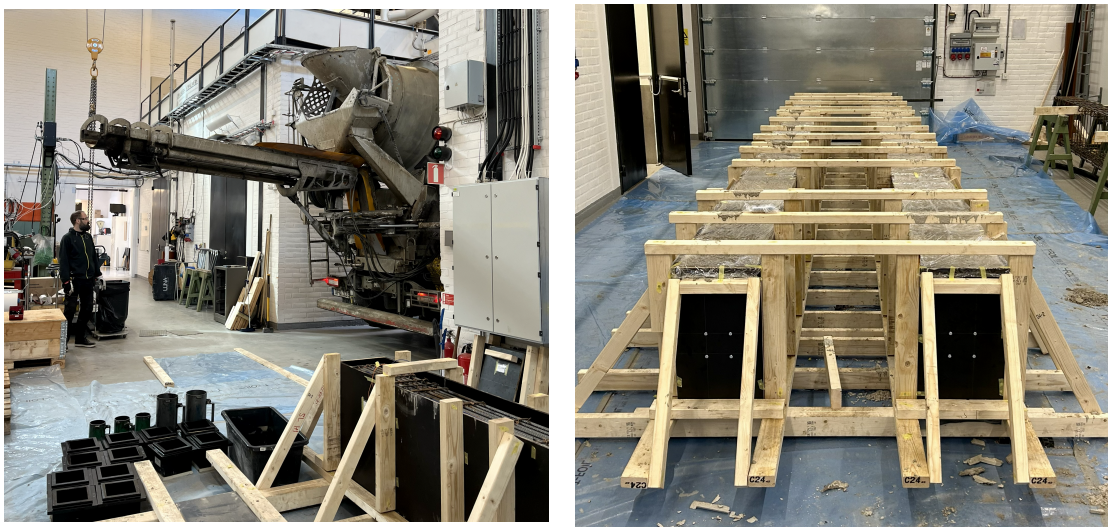

Figure 3.5: a) Casting the forms for beam, cubes and cylinders. b) Concrete hardening in the laboratory.

3.2.5 Post-Tensioning

The post-tensioning system consisted of a live end and a dead end. This means that the hydraulic jack tensioned the strands from one side while the opposite side resists the applied force. The strands consisted of seven steel wires twisted together. They were threaded through the ducts and tensioned in an X-pattern in order to achieve force symmetry.

The target prestressing force was 160 kN per strand. However, to achieve this final force level, the first strand needed to be tensioned to a higher force than the later stands due to stiffness losses occurring as additional strands were tensioned. Anchorage set losses and relaxation losses in the strands were also taken into account. The prestressing force applied during tensioning for each tendon is presented in Table 3.4, and the post-tensioning setup is shown in Figure 3.6

Before tensioning, the formework was removed and the beams were lifted into place on one pinned support and one roller support in order to create a simply supported system. The supports were positioned to obtain a free span of 8 meters. The roller support can be seen in Figure 3.6.

Table 3.4: Cable tensioning force.

Cable	Tensioning force
1	190 kN
2	188 kN
3	186 kN
4	184 kN

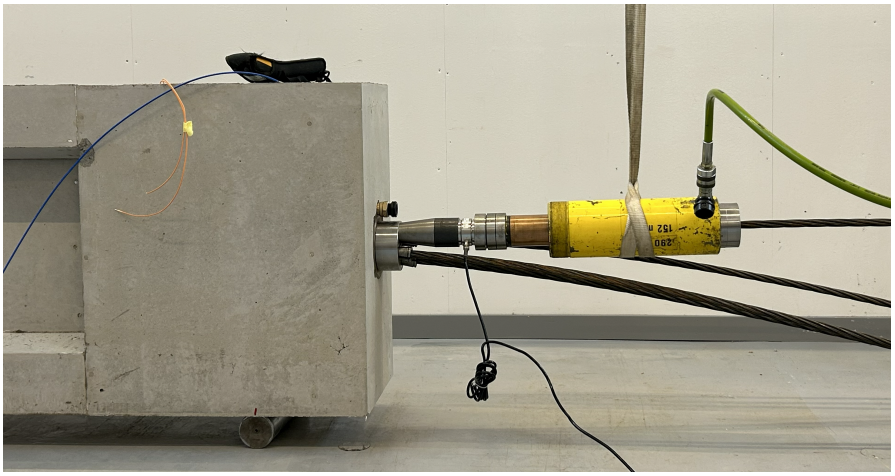

Figure 3.6: Post-tensioning system and hydraulic jack.

Lastly after all strands were tensioned, the duct was grouted using a cement-based grout. The grout was injected into the ducts by connecting a hydraulic pump to the cement mixer and continuously filling the ducts until grout emerged from the outlet at the dead end. This ensured that the ducts were completely filled and that no air voids remained within the system.

3.2.6 Compressive Strength Test of Cube Specimens

The compressive strength tests were performed in accordance with EN 12390-3 (European Committee for Standardization, 2019c) for the respective concrete mixes. The cube specimens had dimensions of $150 \times 150 \times 150$ mm. At 3, 7, and 28 days after casting, three specimens were tested, and the mean compressive strength was determined. The results are presented in Table 3.5, while Figure 3.7a illustrates a cube specimen during the compressive strength test.

Table 3.5: Compressive strength of the three concrete mixes at 3, 7 and 28 days.

P-RC	**Test 1**	**Test 2**	**Test 3**	**Mean value**	**Unit**
Day 3	43.3	44.3	44.3	44.0	MPa
Day 7	49.5	48.8	50.8	49.7	MPa
Day 28	57.6	56.3	58.7	57.6	MPa
P-RC^{CO_2}	**Test 1**	**Test 2**	**Test 3**	**Mean value**	**Unit**
Day 3	33.0	32.9	33.4	33.1	MPa
Day 7	49.6	49.2	49.3	49.4	MPa
Day 28	58.5	58.6	60.2	59.1	MPa
P-FRC^{CO_2}	**Test 1**	**Test 2**	**Test 3**	**Mean value**	**Unit**
Day 3	26.0	26.2	26.3	26.2	MPa
Day 7	39.7	39.7	39.5	39.6	MPa
Day 28	53.6	51.7	52.6	52.6	MPa

Figure 3.7: a) Compressive strength cube test. b) Modulus of elasticity cylindrical test. Both tests where performed in a Toni Technik machine.

3.2.7 Determination of Modulus of Elasticity of Cylinder Specimens

The modulus of elasticity in compression was determined for the respective concretes in accordance with EN 12390-13 (European Committee for Standardization, 2021), see Figure 3.7b for the test setup. The obtained results are presented in Table 3.6. However, the measured values were considered unreliable and were therefore not used in the calculations. Instead, they were only used as reference values for comparison and validation purposes.

Table 3.6: Determination of secant modulus of elasticity in compression for the three concrete mixes at 3, 7 and 28 days.

P-RC	**Test 1**	**Test 2**	**Test 3**	**Mean value**	**Unit**
Day 3	23.5	24.5	22.4	23.5	GPa
Day 7	26.7	26.7	25.7	26.4	GPa
Day 28	26.4	28.3	26.5	27.1	GPa
P-RC^{CO_2}	**Test 1**	**Test 2**	**Test 3**	**Mean value**	**Unit**
Day 3	21.6	20.0	21.3	21.0	GPa
Day 7	25.6	23.9	24.0	24.5	GPa
Day 28	28.1	29.9	27.1	28.4	GPa
P-FRC^{CO_2}	**Test 1**	**Test 2**	**Test 3**	**Mean value**	**Unit**
Day 3	20.3	18.6	19.4	19.4	GPa
Day 7	22.4	22.7	24.7	23.3	GPa
Day 28	27.2	26.7	26.1	26.7	GPa

The modulus of elasticity at t days, E_t, was calculated by converting the compressive strength of the cube specimens according to Eurocode 2:

$$E_t = 22 \cdot (\frac{f_{cm.cube.t}}{1.2} \cdot \frac{1}{10})^{0.3} \tag{3.1}$$

where:

- $f_{cm.cube.t}$ is the compressive cube strength at a specific day.

The resulting modulus of elasticity is presented in Table 3.7. It should be noted that the concrete used in this study was SCC with a maximum aggregate size of 8 mm. As the equations used to estimate the modulus of elasticity were developed for conventional concrete, the predicted values may be slightly higher than the actual modulus of elasticity of the beams. This can be attributed to the lower aggregate content and higher paste content, including binder, water, and limestone filler, in SCC.

Table 3.7: The calculated modulus of elasticity for the three concrete mixes at 3, 7 and 28 days.

Concrete type	**Day 3**	**Day 7**	**Day 28**	**Unit**
P-RC	32.5	33.7	35.2	GPa
P-RC^{CO_2}	29.8	33.6	35.5	GPa
P-FRC^{CO_2}	27.8	31.5	34.3	GPa

3.2.8 Determination of Shrinkage and Creep of Concrete

Shrinkage and creep were determined experimentally using concrete cylinders stored in a climate room with controlled environmental conditions of 50% relative humidity and a temperature of 20 °C. DOFS were attached to the specimens in order to measure the time-dependent strains due to shrinkage and creep. The experimental setup followed EN 12390-16 (European Committee for Standardization, 2019a) and EN 12390-17 (European Committee for Standardization, 2019b), however, since DOFS were used for strain measurements, the test procedure did not fully comply with the standard specifications.

Shrinkage strain was obtained from an unloaded concrete cylinder, while the total strain from creep and shrinkage was measured on a cylinder subjected to a sustained compressive stress of approximately 4.5 MPa. Figure 3.8 shows the loaded cylinders used in the experiment. The test was conducted for the P-RC and P-RC^{CO_2} specimens.

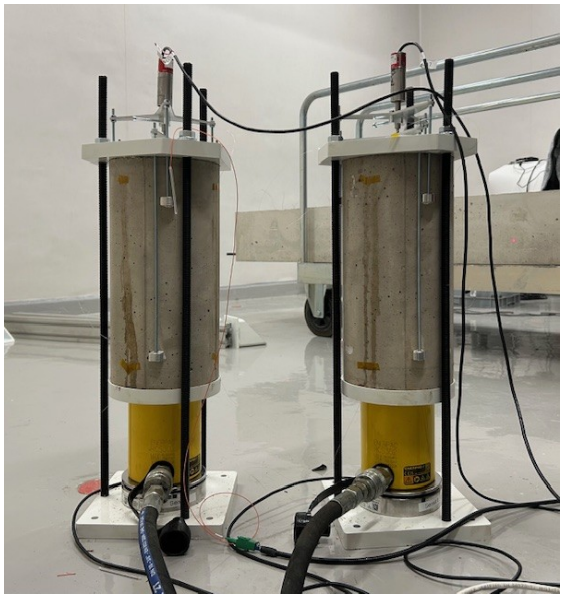

Figure 3.8: Cylinder experiment measuring total strain from creep and shrinkage.

3.3 Post Processing and Analysis Phase

This section describes the post-processing and analysis of the strain data acquired using DOFS. The numerical processing and structural evaluations were conducted using Python and MATLAB. The purpose of the post-processing phase was to transform the measured strain data into meaningful structural response parameters, including curvature, rotation, deflection, bending moment, and post-tensioning force. The section first presents the post processing for the beam specimens, followed by the post processing of the cylinder specimens for the creep and shrinkage experiment.

3.3.1 Post Processing for Beam Specimens

The post-processing procedure aimed to capture the structural behavior of the beam by deriving curvature, rotation, deflection, bending moment, and post-tensioning force from the strain obtained with the DOFS. This methodology followed the approach presented by Fernandez et al. (2025), where the beam response was reconstructed using simplified mechanical assumptions.

The curvature of the beam section could be calculated assuming plane sections remain plane, according to Euler–Bernoulli beam theory. Using the strains measured at the top and bottom fibres, the curvature, $\chi(x,t)$, was given by:

$$\chi(x,t) = \frac{\varepsilon_{\text{bottom}}(x,t) - \varepsilon_{\text{top}}(x,t)}{z} \tag{3.2}$$

where:

- $\varepsilon_{\text{bottom}}(x,t)$ is the measured strain in the bottom fibre,

- $\varepsilon_{\text{top}}(x,t)$ is the measured strain in the top fibre, and
- z is the vertical distance between bottom and top fibre.

The rotation, $\theta(x,t)$, of the beam section was obtained by integration of the curvature along the beam length:

$$\theta(x,t) = \int_0^x \chi(x,t)\,\mathrm{d}x \tag{3.3}$$

where:

- x is the longitudinal coordinate along the specimen.

Subsequently, the vertical deflection, $y(x,t)$, of the beam was calculated as the integral of the rotation. In this work, deflections were obtained by double integration of the curvature, which has been shown to provide accurate results when compared to displacement transducers for serviceability-level deformations (Fernandez et al., 2025).

$$y(x,t) = \int_0^x \theta(x,t)\,\mathrm{d}x = \int_0^x \int_0^x \chi(x,t)\,\mathrm{d}x\,\mathrm{d}x \tag{3.4}$$

Based on the calculated curvature, the bending moment, $M(x,t)$, along the beam could be derived using Euler–Bernoulli beam theory:

$$M(x,t) = \chi(x,t)\,EI \tag{3.5}$$

where:

- EI is the flexural stiffness of the section.

Knowing the bending moment, the post-tensioning force $P(x,t)$ could be estimated by relating the sectional moment to the eccentricity of the tendon according to Fernandez et al. (2025):

$$P(x,t) = \frac{M(x,t)}{e(x)} \tag{3.6}$$

where:

- $e(x)$ is the tendon eccentricity.

This relationship assumes that the bending moment was predominantly generated by the post-tensioning force acting at an eccentricity e with respect to the centroidal axis of the section. Following this approach, the variation of post-tensioning force along the beam could be evaluated, which enables the quantification of instantaneous losses due to friction and seating effects.

The instantaneous losses were evaluated by comparing the strain levels at specific stages of the tensioning process. The seating loss was identified in the strain data as a distinct drop immediately following the peak tensioning force, as illustrated in Figure 3.9.

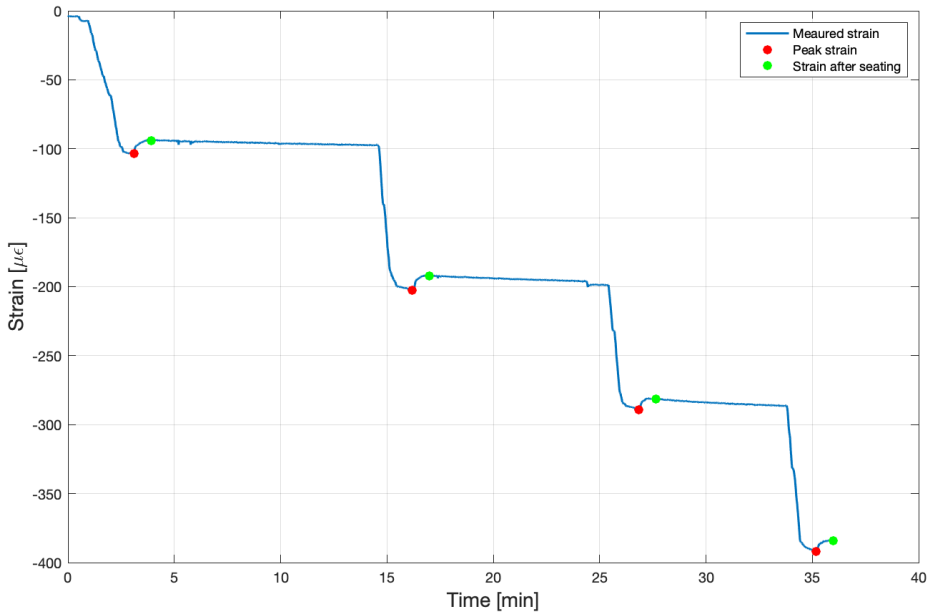

Figure 3.9: Example of points used for calculation

Furthermore, friction losses along the tendon were evaluated by comparing the tendon force derived from the strain measurements (Equation 3.6) with the actual force applied at the jack, as measured by the load cell.

For the long-term prestressing force loss the following relationship could be used to calculate the force loss:

$$\Delta P = E_p A_p \Delta \varepsilon_{\text{DOFS}} \tag{3.7}$$

where:

- ΔP is the post-tensioning force loss,
- E_p is the modulus of elasticity of the prestressing steel,
- A_p is the area of prestressing steel, and
- $\Delta \varepsilon_{\text{DOFS}}$ is the strain measured from DOFS at the prestressing steel level.

The strain at the prestressing level, $\Delta \varepsilon_{\text{DOFS}}$, could either be obtained directly from DOFS attached at the duct or calculated from the curvature derived using the top and bottom DOFS measurements. According to Fernandez et al. (2025), both approaches yield comparable results. In this study, both methods were initially applied to verify this consistency; however, the curvature-based method was subsequently used for further analysis.

For further comparison the force loss was also calculated using the following equation from Eurocode 2:

$$\Delta P = A_p \Delta \sigma_p = A_p \frac{E_p \varepsilon_{cs} + 0.8 \chi_t \, \sigma_{pi} + \frac{E_p}{E_{cm}} \varphi(t, t_0) \, \sigma_{cpi}}{1 + \frac{E_p}{E_{cm}} \frac{A_p}{A_c} \left(1 + \frac{A_c}{I_c} e^2\right) (1 + 0.8 \, \varphi(t, t_0))} \tag{3.8}$$

where:

- σ_{pi} is the initial stress in prestressing steel,
- σ_{cpi} is the initial concrete stress at prestressing steel level,
- χ_t is the relaxation factor,
- A_c is the area of concrete cross section, and
- E_{cm} is the modulus of elasticity for concrete.

It should be noted that this equation is simplified, as it does not account for the presence of normal reinforcement. Reinforcement introduces internal restraint, which reduces the effects of shrinkage and creep. Consequently, the prestress loss is likely to be overestimated over time.

Equation 3.8 has also been used in combination with the methods presented in the next Section 3.3.2. The shrinkage and creep strains from the cylinder test were converted into force loss for the beam.

3.3.2 Post Processing for Creep and Shrinkage Test

The data acquired from the creep and shrinkage tests were utilized to decouple the total measured strain in the beams into its individual components: shrinkage, creep, relaxation, and elastic strain. By isolating these components, the long-term behavior of the different concrete mixes could be compared and evaluated. To convert the strains two methods were developed: the Experimental Interpolation Method and the Eurocode-Scaled Experimental Method, which were then compared to the Eurocode 2 calculations.

To convert the measured shrinkage strains from the cylinder to the beam, the notional size h_0, introduced in Section 2.4.2, was used for both methods. This to account for the differences in geometry between the cylinders and the full-scale beams. The conversion of the shrinkage strain was performed according to:

$$\varepsilon_{cs,beam}(t) = \varepsilon_{cs,cyl}(t)\,\frac{h_{0,beam}}{h_{0,cyl}} \tag{3.9}$$

where:

- $\varepsilon_{cs,beam}(t)$ is the total shrinkage strain in the beam,
- $\varepsilon_{cs,cyl}(t)$ is the total shrinkage strain measured in the cylinder,
- $h_{0,beam}$ is the notional size of the beam, and
- $h_{0,cyl}$ is the notional size of the cylinder.

Regarding creep, the strain measured on the cylinders was converted to the corresponding strain in the beam by assuming a linear relationship between the cylinder and beam responses. The conversion for both methods, Experimental Interpolation Method and Eurocode-Scaled Experimental Method, rely on the assumption of a proportional relationship expressed as:

$$\frac{\varphi_{exp,beam}}{\varphi_{EC,beam}} = \frac{\varphi_{exp,cyl}}{\varphi_{EC,cyl}} \tag{3.10}$$

where:

- $\varphi_{exp,beam}$ is the creep coefficient obtained from the measured beam strains,
- $\varphi_{EC,beam}$ is the creep coefficient derived for the beam with Eurocode,
- $\varphi_{exp,cyl}$ is the creep coefficient obtained from the measured cylinder strains, and
- $\varphi_{EC,cyl}$ is the creep coefficient derived for the cylinder with Eurocode.

The Experimental Interpolation Method was based on the assumption of a linear relationship trend presented in the new Eurocode (EN 1992-1-1:2023). A linear curve was fitted to the tabulated values, and the 50-year creep coefficient for the cylinder, calculated according to (EN 1992-1-1:2023), was used to determine the corresponding creep coefficient for the beam through interpolation. Figure 5.11 illustrates the workflow applied to both P-RC and P-RC^{CO_2} concretes.

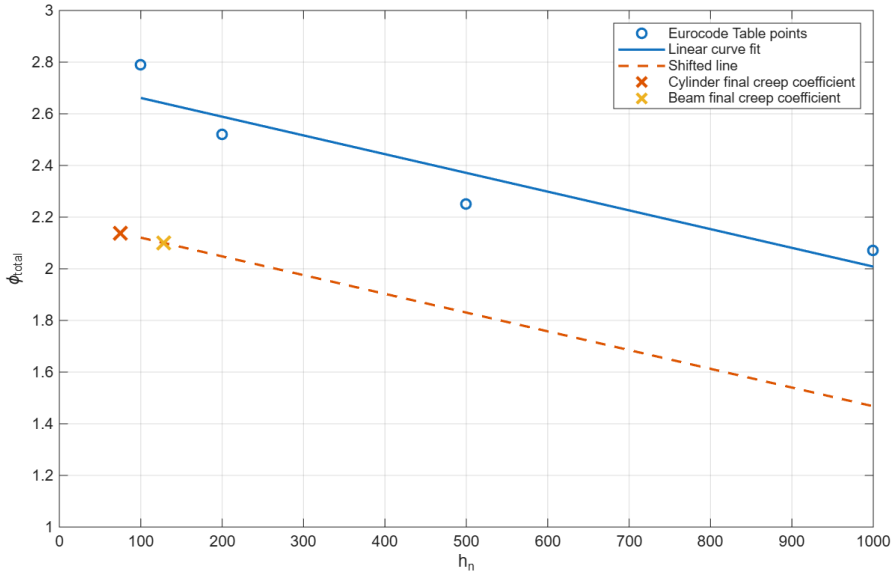

Figure 3.10: Total strain calculated with three different methods. For both P-RC and P-RC^{CO_2} gets same values.

The experimental cylinder creep coefficient was subsequently scaled using the ratio between the 50 year creep coefficients of the beam and the cylinder. The resulting value was then converted into the beam creep strain $\varepsilon_{creep,beam}$ using the measured elastic strain of the beam according to the following relationship:

$$\varepsilon_{creep,beam} = (\varphi_{exp,cyl} \cdot k_\varphi + 1) \cdot \varepsilon_{el,beam} \tag{3.11}$$

$$\varepsilon_{creep,beam} = (\varphi_{exp,cyl} \cdot \frac{\varphi_{50y,beam}}{\varphi_{50y,cyl}} + 1) \cdot \varepsilon_{el,beam} \tag{3.12}$$

where:

- k_φ is the ratio of 50 year creep coefficients, given by $\frac{\varphi_{50y,beam}}{\varphi_{50y,cyl}}$, and
- $\varepsilon_{el,beam}$ is the measured elastic strain of the beam.

The Eurocode-Scaled Experimental Method followed the Eurocode (EN 1992-1-1:2004) formulation more closely by explicitly calculating the governing parameters and applying a scaling approach based on the ratio of creep coefficients. In this method, the experimentally obtained cylinder creep coefficient was amplified to estimate the corresponding beam creep strain $\varepsilon_{creep,beam}$. The relationship was expressed as:

$$\varepsilon_{creep,beam} = (\varphi_{exp,cyl} \cdot k_{notional} \cdot k_{\beta_c} + 1) \cdot \varepsilon_{el,beam} \tag{3.13}$$

$$\varepsilon_{creep,beam} = (\varphi_{exp,cyl} \cdot \frac{\varphi_{0,beam}}{\varphi_{0,cyl}} \cdot \frac{\beta_{c,beam}}{\beta_{c,cyl}} + 1) \cdot \varepsilon_{el,beam} \tag{3.14}$$

where:

- $k_{notional}$ is the ratio of notional creep coefficients, given by $\frac{\varphi_{0,beam}}{\varphi_{0,cyl}}$, and
- k_{β_c} is the ratio of the creep development functions, given by $\frac{\beta_{c,beam}}{\beta_{c,cyl}}$.

The reference values were based only on Eurocode calculations (EN 1992-1-1:2004), with the exception that the elastic strain, $\varepsilon_{el,beam}$, was obtained from measured beam strains rather than calculated values.

$$\varepsilon_{c,creep} = (\varphi_{creep,EC} + 1) \cdot \varepsilon_{el,beam} \tag{3.15}$$

where:

- $\varepsilon_{c,creep}$ is the creep strain, and
- $\varphi_{creep,EC}$ is the creep coefficient calculated for the beam with Eurocode.

The relaxation strain was determined according to Eurocode 2 (EN 1992-1-1:2004) for both methods and therefore remained identical to the values obtained from the reference Eurocode approach. The calculations were based on the equations presented in Section 2.4.3.

Additional calculations were made using the Annex B calculation method in the new Eurocode (EN 1992-1-1:2023) to compare with the measured creep and shrinkage strains.

4 Results

This section presents the results from the experimental monitoring, which are divided into two primary phases: tensioning and long-term behaviour. The tensioning phase encompasses the period during which the four tendons were sequentially stressed and concludes prior to the grouting of the duct, while the long-term phase covers the subsequent period were the beams were fully post-tensioned, grouted, and monitored in their stored positions. Throughout these phases, the DOFS provided measurements of the total strain, while the load cell recorded the force applied by the hydraulic jack during the tensioning. For the cylindrical creep and shrinkage experiment, the applied load was obtained from the pressure testing machine, complemented by the strains recorded from the DOFS.

4.1 Tensioning

A comparison between the applied jacking force and the resulting strain response at midspan of the P-RC beam is presented in Figure 4.1. The strains were measured using the DOFS sensors attached to the bottom reinforcing bar. While the load cell recordings showed that the force at the jack returned to zero following the release of each tendon, as shown in Figure 4.1(a), the DOFS data captured the stepwise increase in strain corresponding to the prestressing force transferred to the beam, as shown in Figure 4.1(b).

As shown in Figure 4.1, the strain increased during the tensioning of each tendon, with an additional increase observed between successive tensioning stages. During these intermediate periods, the strain exhibited a slight upward trend rather than remaining perfectly constant. This gradual increase was relatively small but consistent and was mainly attributed to creep effects.

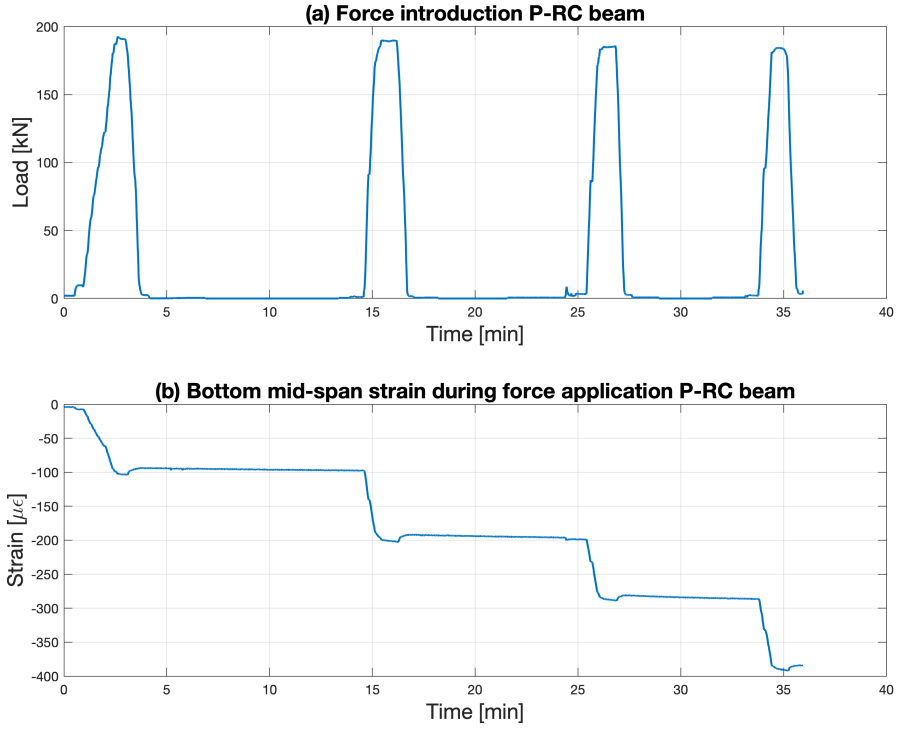

Figure 4.1: Load introduction in P-RC beam.

The strain distribution along the beams during the tensioning process is illustrated in Figure 4.2. The figure is divided into top strain (a-c) and bottom strain (d-f) for the three beam specimens. A clear increase in strain was observed as each of the four tendons was tensioned, indicated by the darkening gradient.

For the P-RC beam, the bottom strain reached a peak value of approximately -400 $\mu\epsilon$ at midspan after all four tendons had been tensioned, while the top strain reached approximately 30 $\mu\epsilon$. A similar trend was observed in the other two beams, although the measured strains were slightly lower.

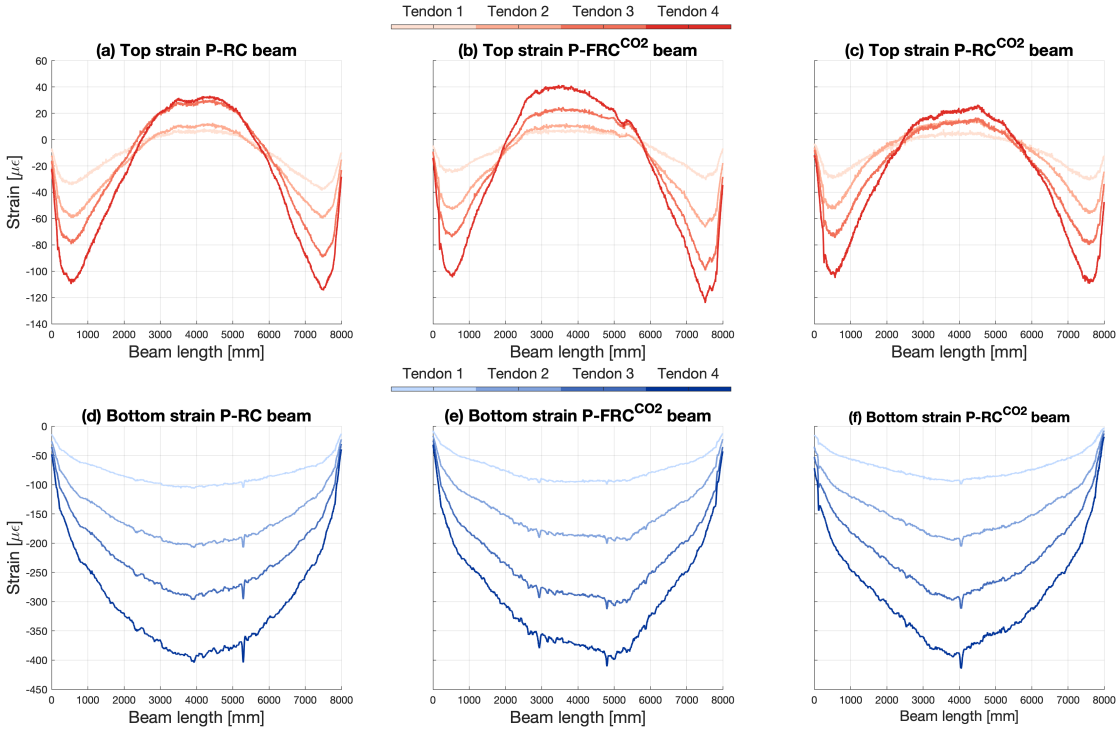

Figure 4.2: Strain evaluation as each of the four tendons is tensioned

4.2 Early Long-Term Effects

Figure 4.3 presents the long-term strain development along the beam length for all three beam specimens. The figure is divided into top strains (a-c) and bottom strains (d-f). As observed, the strain magnitude increased over time due to the effects of creep and shrinkage. For instance, the bottom strain in the P-RC beam increased from approximately -400 $\mu\epsilon$ to -900 $\mu\epsilon$ during the 60-day monitoring period. The results further showed that the P-RC beam exhibited 18-20% greater total bottom strain than the low-CO_2 concrete beams.

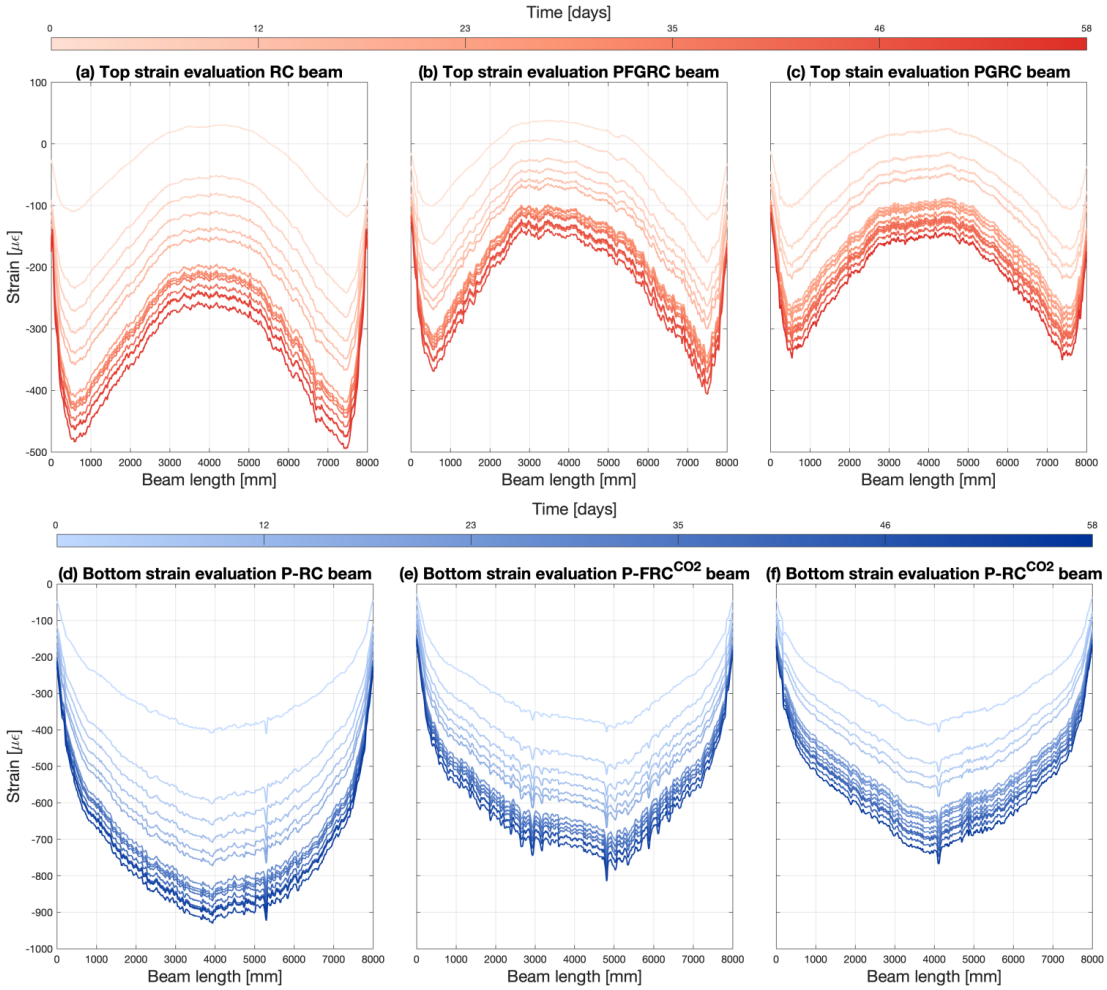

Figure 4.3: Strain evaluation over time for all three beams

The long-term creep and shrinkage experiment provided strain measurements associated with the long-term behaviour of the P-RC specimen and the P-RC^{CO_2} specimen. Figure 4.4(a) presents the strain development for the P-RC specimen, including creep strain, shrinkage strain, and total strain. Figure 4.4(b) presents the corresponding results for the P-RC^{CO_2} specimen.

Both the creep and shrinkage strains exhibited a more rapid development during the first few days, after which the rate of increase gradually stabilised over time. Figure 4.4(c) presents a comparison of the creep strains measured in the P-RC specimen and the P-RC^{CO_2} specimen. The drop at time zero represented the initial elastic strain and had a magnitude of -135 $\mu\epsilon$ for the P-RC specimen and -133 $\mu\epsilon$ for the P-RC^{CO_2} specimen. After 40 days, the total strain measured in the P-RC specimen was approximately 10% greater than that measured in the P-RC^{CO_2} specimen.

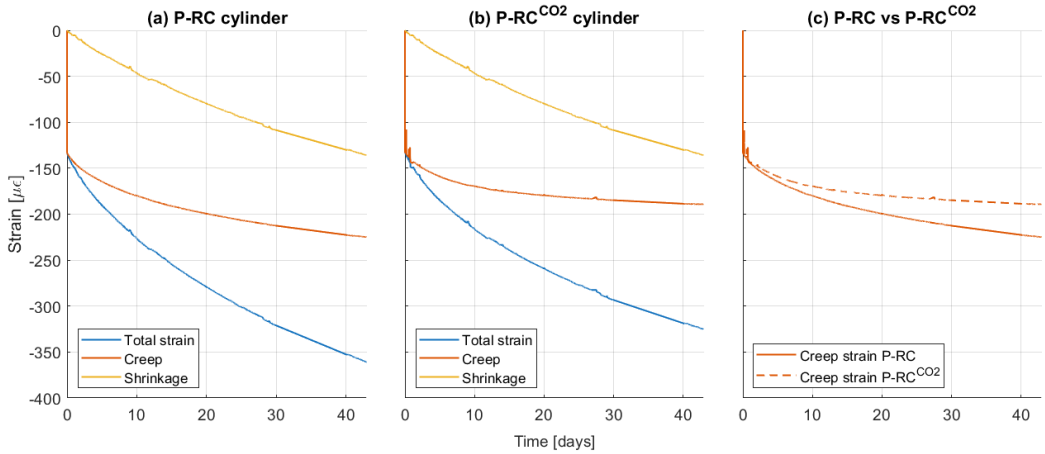

Figure 4.4: a) Creep, shrinkage and total strain for P-RC cylinder. b) Creep, shrinkage and total strain for P-RC^{CO_2} cylinder. c) Creep strain in both P-RC and P-RC^{CO_2} cylinders over time.

Figure 4.5 presents the pressure measured by the testing equipment during the creep and shrinkage cylinder experiment. As shown in Figure 4.5, the pressure in the creep-shrinkage testing machine gradually decreased over time. This reduction was attributed to creep and shrinkage shortening of the specimens during the test. As the specimens shortened, the loading system required continuous adjustment to maintain the applied force. This resulted in pressure losses within the hydraulic oil system and consequently a gradual decrease in the measured pressure over time. The effect became more pronounced as the accumulated deformation increased.

Nevertheless, the observed pressure reduction of less than 2.6% during the first 45 days remained within an acceptable range for the test setup. The pressure measured by the equipment, for example 157 kPa, corresponded to an applied stress of 4.2 MPa in the specimen.

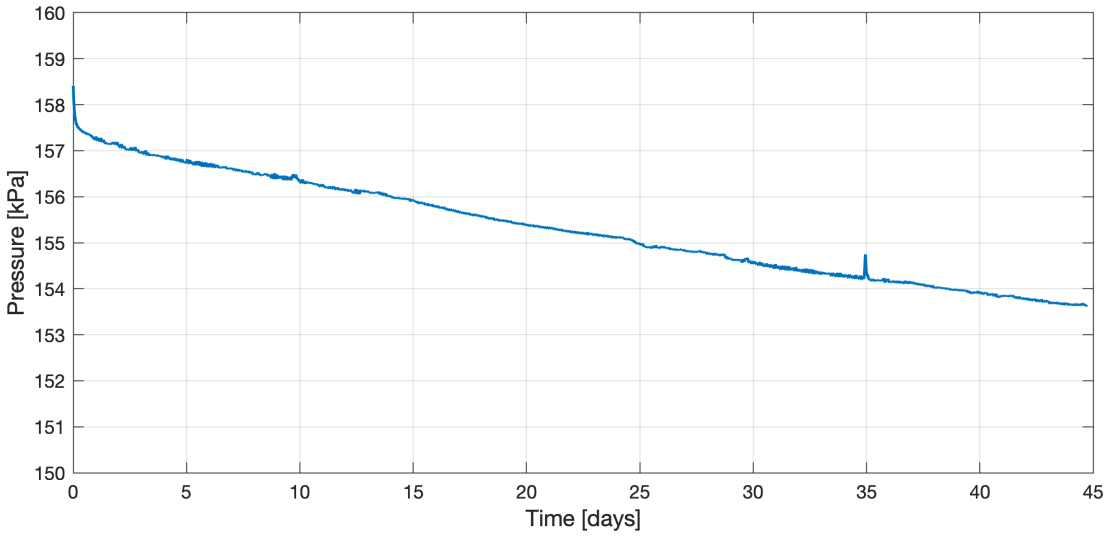

Figure 4.5: The pressure for the creep-shrinkage-cylinder experiment over time.

5 Discussion

This section presents the post-processing and analysis of the strains obtained from the DOFS. The discussion is structured to first address the tensioning phase, including force transfer and initial prestress losses. Then, the long-term response is evaluated with focus on creep, shrinkage, and force loss, and compared with Eurocode predictions. Finally, experimental limitations and implications for design are presented.

5.1 Tensioning

With the strain measurements obtained from the DOFS system during tensioning the behavior of the beam could be analysed further. Using Equation 3.4, the midspan deflection during the tensioning stage was calculated from the strain measurements obtained by the DOFS. The evolution of the midspan deflection during tensioning is presented in Figure 5.1. For all specimens, an upward deflection is observed to increase incrementally with each tensioned tendon, reflecting the stepwise introduction of prestressing force. Between successive tensioning steps, distinct plateaus in the deflection response can be identified, indicating stabilisation of the deformation after each load increment. The final midspan deflection at the end of the tensioning stage was 4.78 mm for the P-RC specimen, 4.76 mm for the P-FRC^{CO_2} specimen, and 4.54 mm for the P-RC^{CO_2} specimen. Despite minor differences, the results demonstrate a comparable global structural response during tensioning for all three beams. The slightly smaller final deflection observed for the P-RC^{CO_2} beam is consistent with its lower strain compared to the P-RC specimen, as previously shown in Figure 4.2.

The tensioning procedure for the P-RC beam was carried out according to the intended methodology. However, for the P-FRC^{CO_2} and P-RC^{CO_2} beams, practical issues related to the hydraulic jack and load cell led to deviations from the planned tensioning process. During the tensioning of certain tendons, the hydraulic jack reached its maximum extension before the target prestressing force was achieved. As a result, the jack had to be released, repositioned, and reattached in order to complete the tensioning. These interruptions are reflected in the midspan deflection histories shown in Figure 5.1, most notably during the tensioning of the first tendon in the P-FRC^{CO_2} beam and the second tendon in the P-RC^{CO_2} beam.

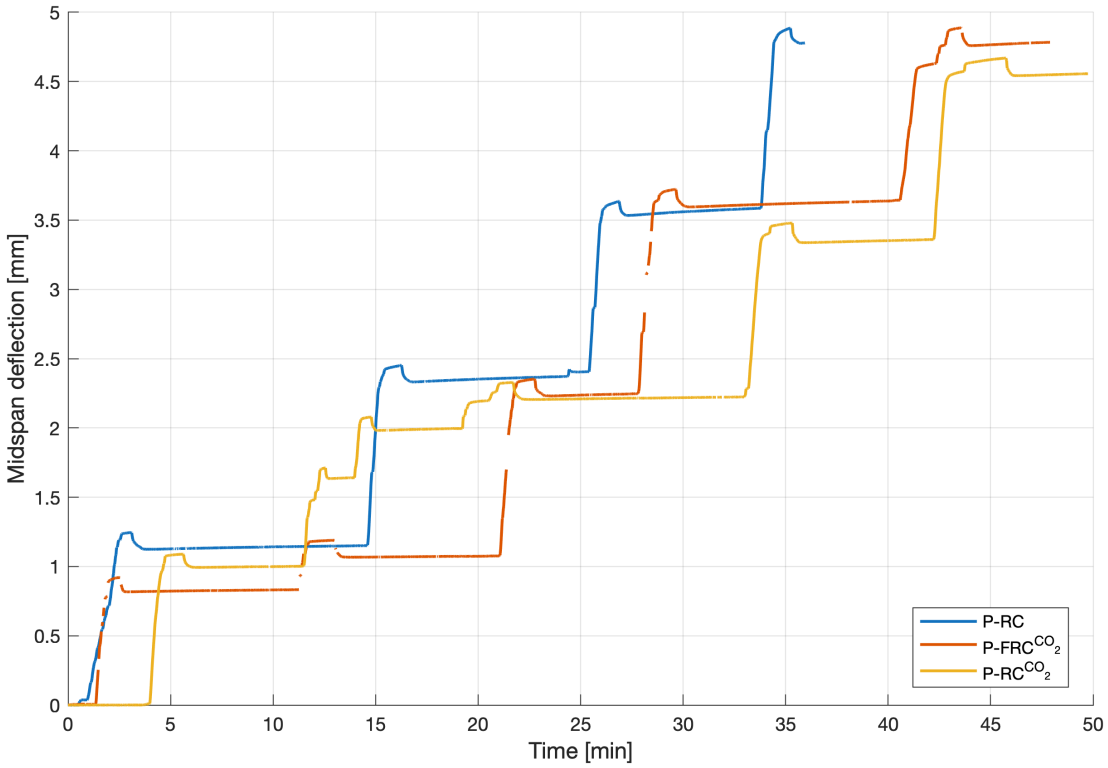

Figure 5.1: Midspan deflection during tensioning.

Figure 5.2 illustrates the evolution of prestressing force, calculated using Equation 3.6, during the tensioning of each tendon. A distinct drop in force is observed immediately after reaching the target force, which corresponds to the release of the jack and results in anchorage seating losses. This behaviour is highlighted in the zoomed view in Figure 5.2(b).

The magnitude of the seating losses is relatively consistent across all tendons, with an average force loss of approximately 15 kN. Notably, this consistency also applies to tendons for which the hydraulic jack had to be repositioned during tensioning. This suggests that the repositioning procedure had a limited influence on the anchorage seating loss.

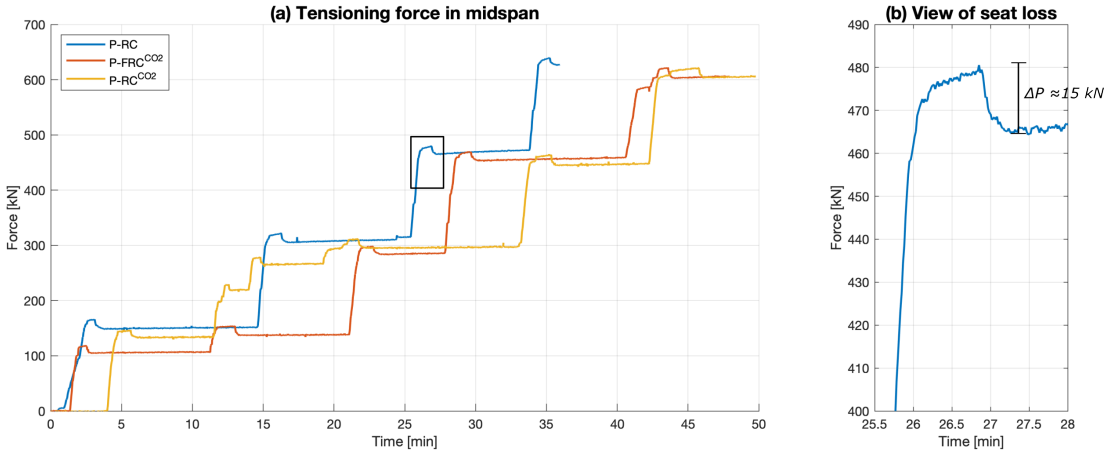

Figure 5.2: Prestressing force increasement and seating loss during post-tensioning.

The friction losses for the P-RC beam during the tensioning process are illustrated in Figure 5.3. The red markers represent the friction losses determined for each tendon based on the strain measurements, while the blue line shows a linear interpolation used to highlight the overall trend. A decreasing tendency in friction loss is observed for each subsequently tensioned tendon.

One possible explanation for this trend is a change in the frictional behaviour within the duct during the tensioning process. As the prestressing procedure progresses, the duct profile may gradually straighten due to the applied forces, reducing the angular deviations that contribute to friction losses. However, when applying the Eurocode 2 formulation for friction losses and considering the observed variation in midspan deflection during tensioning, the corresponding change in angular deviation results in only a marginal reduction in friction loss of approximately 0.02% from the first to the last tendon.Therefore, changes in duct geometry alone cannot explain the observed reduction in friction losses.

Another contributing factor may be the interaction between the tendons within the duct during the prestressing process. The first tendon is likely subjected to different contact conditions compared with the subsequently tensioned tendons. During stressing, the tendons may experience contact not only with the duct surface but also with neighbouring tendons, which can influence the effective friction behaviour. Such interaction may contribute to reduced friction for later tensioned tendons, as also suggested by Hong (2017), who reported that repeated movement within a duct may lead to reduced frictional resistance.

The friction coefficients provided in Eurocode 2 (EN 1992-1-1, Section 5.10.5.2) are primarily intended for conventional post-tensioning applications, that all tendons are tensioned simultaneously, and do not explicitly account for tendon-to-tendon interaction effects. Consequently, limited information could be found regarding variations in friction losses between sequentially tensioned tendons, and no specific tendon-to-tendon friction coefficient is provided. However, comparison of the friction coefficients for different material combinations, presented in Eurocode 2, indicates that the friction behaviour can vary significantly depending on the contact surfaces. For example, the difference between tendon-to-plastic and tendon-to-metal friction coefficients is approximately 38%, suggesting that material interaction influence the friction losses.

The observed reduction in friction losses from the first to the last tendon can also be related to the initial arrangement of the tendons within the duct. Before stressing, the tendons are likely be distributed irregularly within the duct and experience local contact and interlocking effects. During stressing of the first tendon, additional resistance may therefore arise as the tendon adjusts its position relative to neighbouring tendons. Once the first tendon has been tensioned, the tendon configuration within the tendons become more evenly arranged within the duct, potentially allowing the subsequent tendons to move with less resistance and thereby reducing the friction losses.

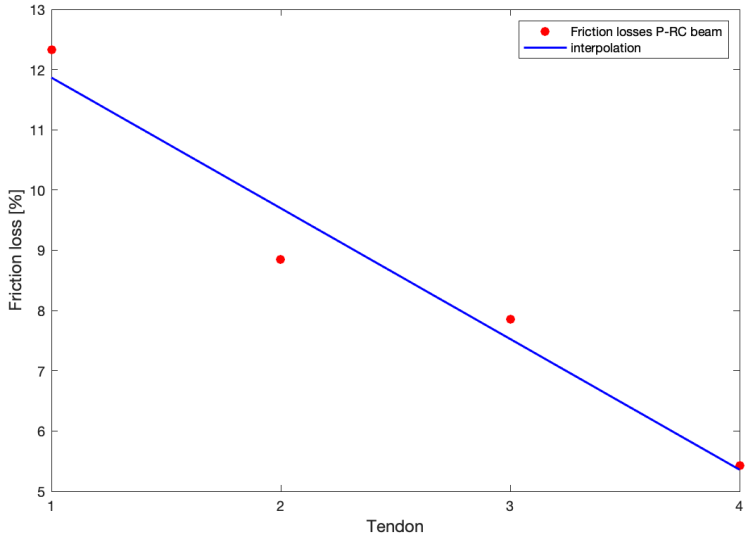

Figure 5.3: Interpolated and measured friction losses for the P-RC beam during the tensioning process.

Since reliable load cell data were only available for the P RC specimen, the prestressing forces in the P-FRC^{CO_2} and P-RC^{CO_2} beams could not be determined with the same level of accuracy. Instead, these forces were set based on hydraulic pressure and elongation measurements. Therefore, exact values for the tendon force were estimated based on strain measurements and the observed friction trends. The resulting tendon forces for each specimen are summarised in Table 5.1. The total prestressing force differs between the beams, with the P-RC beam exhibiting the highest prestressing level and the P-RC^{CO_2} beam the lowest. These differences are important when later comparing the long-term behavior of the beams, as higher prestressing forces increase both the immediate elastic strain and the time dependent creep deformation.

Table 5.1: Applied tendon forces for the different beam types including a comparison with load cell data for the P-RC beam.

Tendon	**P-FRC^{CO_2} [kN]**	**P-RC^{CO_2} [kN]**	**P-RC Load Cell [kN]**
1	175.59	165.42	192.80
2	181.97	197.33	190.07
3	207.22	180.83	186.04
4	176.83	184.65	184.36
Sum	**741.60**	**728.23**	**753.26**

Figure 5.4 illustrates the estimated instantaneous tendon losses along the beam, expressed as the percentage of prestressing force lost per unit of introduced load. The shaded orange region represents the anchorage seating losses, while the shaded blue region corresponds to friction losses. The maximum seating loss occurs closest to the jacking end (x = 0), resulting from the physical slip of the wedges as the jack releases the tendon. The seating loss then dissipates linearly as it moves towards the dead end and at this end the friction losses instead is at its maximum. The estimated force in the

tendon is represented by the continuous black line. In the central part of the beam, the prestressing force is assumed to be approximately constant due to the limited variation in tendon eccentricity, resulting in a nearly straight tendon profile in this region.

The tendon eccentricity has a significant impact on the estimation of the post-tensioning force, as the calculation becomes highly sensitive when the eccentricity approaches zero in the outer regions. As discussed by Fernandez et al. (2025), small uncertainties in tendon position may lead to substantial variations in the calculated force, particularly near the beam supports where the eccentricity approaches zero. Nevertheless, within the central regions of the beam, this approach provides a more reliable estimation of the post-tensioning force and the associated losses. Due to the parabolic tendon profile and the variation in both friction and seating losses along the beam, the prestressing force is not uniformly distributed. Instead, it varies significantly along the beam length. This non-uniform force distribution leads to a corresponding variation in stress and strain, which may influence the development of time-dependent effects such as creep and shrinkage.

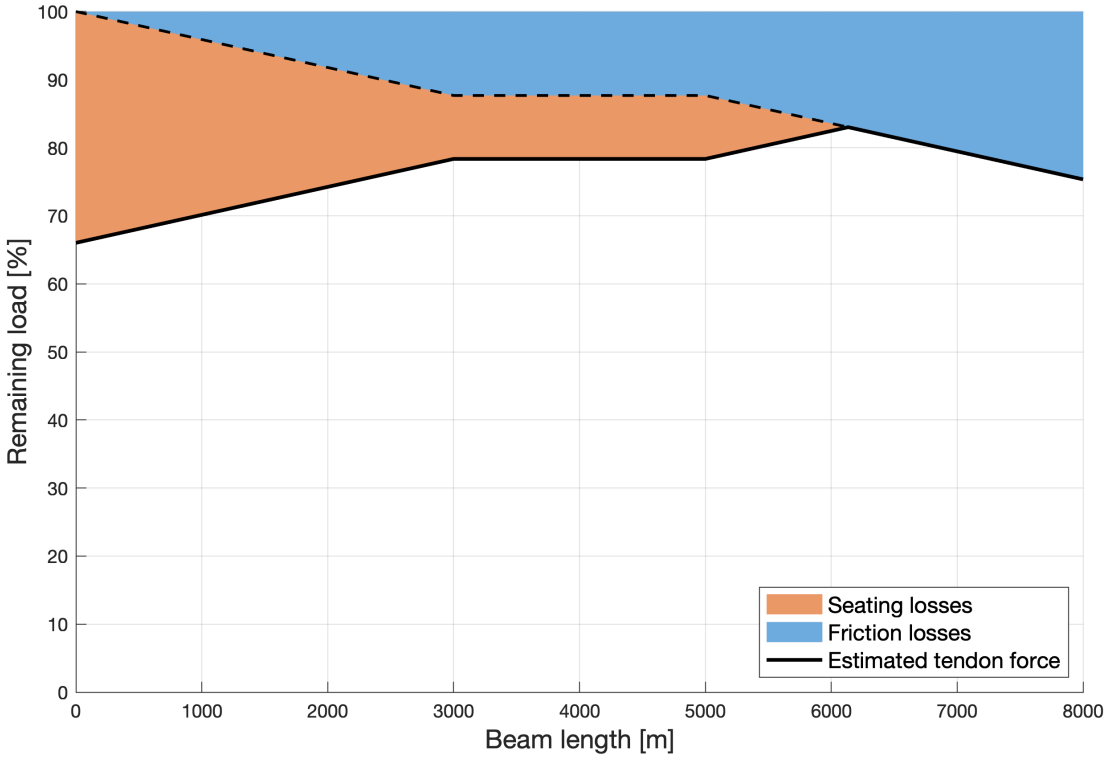

Figure 5.4: Estimated instantaneous tendon losses during tensioning of first tendon

5.2 Early Long-Term Response

The main focus of this section is on comparing the long-term behaviour of the conventional concrete beam, P-RC, the fibre-reinforced concrete beam, P-FRC^{CO_2}, and the low-CO_2 concrete beam, P-RC^{CO_2}. The long-term response of the beams is analysed in terms of curvature, deflection, the decoupling of creep and shrinkage effects from cylinder to beam behaviour, Eurocode predictions and prestress force losses.

5.2.1 Beam Response Over Time

The long-term response of the beam specimens is governed by time-dependent effects. These mechanisms influence the development of beam curvature and deflection over time. The change in curvature over time is shown in Figure 5.5 for all beam specimens. The overall shape of the curvature distribution remains consistent, while the magnitude becomes larger, indicating that the time-dependent effects primarily amplify the existing bending behaviour rather than altering the structural response.

The curvature distribution for the P-RC and P-RC^{CO_2} beams is relatively smooth and closely resembles the expected parabolic shape for a simply supported beam subjected to prestressing. In contrast, the P-FRC^{CO_2} beam exhibits a slightly flatter curvature profile in the midspan region. This difference can be related to the geometry of the tendon profile. For a perfectly parabolic tendon, the eccentricity varies along the beam, resulting in a bending moment distribution, and hence a curvature, that follows a parabolic shape. This behaviour is reflected in the P-RC and P-RC^{CO_2} beams. In contrast, if the tendon were perfectly straight, the eccentricity would remain constant, leading to a constant bending moment and therefore a nearly uniform curvature along the beam.

The slightly flatter curvature observed in the midspan region of the P-FRC^{CO_2} beam may therefore indicate deviations from an ideal parabolic tendon profile. Such deviations influence the bending moment distribution along the beam and result in a curvature profile that differs from the expected parabolic shape, particularly in the central region.

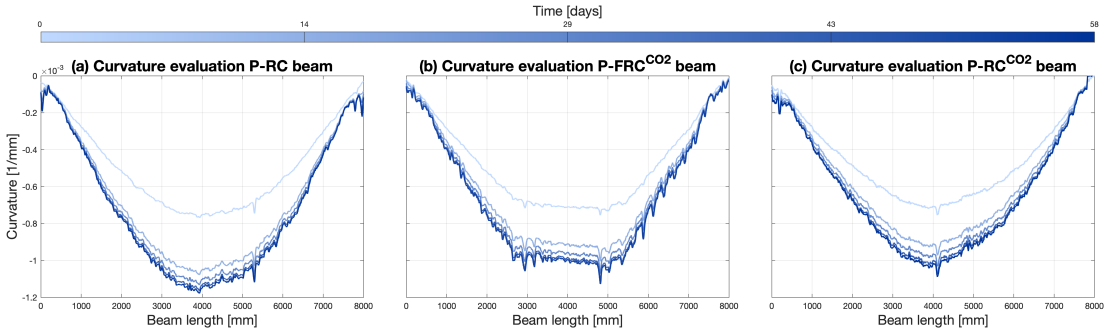

Figure 5.5: Curvature evaluation over time for all three beams.

Based on the curvature, the beam deflection was calculated using Equation 3.4. The midspan deflection over time is presented in Figure 5.6. As shown in the figure, the upward midspan deflection of the specimens increases with time. The measurements started after the placement of the specimens, meaning that the effects due to self-weight can be neglected. Therefore, the presented results reflect the effects of shrinkage, together with creep induced by the post-tensioning stresses and relaxation of the prestressing tendons. The gaps shown in the figure correspond to periods of missing data. The durations of the measurement interruptions are equal for all DOFS, as they were connected to the same machine. However, the interruptions appear offset in time because the time axis is referenced to the onset of the long-term monitoring phase. Since only two formworks were available and the concrete mixes required different curing periods, the long-term phase began at different times for the respective specimens.

Figure 5.6 further shows that the P-RC beam experience the largest uplift while the P-RC^{CO_2} beam shows the smallest. A plausible explanation for this behaviour is that the P-

RC specimen was subjected to higher stress levels from the prestressing force compared with the other two beams, which enhances time-dependent deformation. However, the differences in deflection cannot solely be attributed to the variations in prestressing force but also by differences in the time-dependent material properties, such as creep and shrinkage characteristics of the concrete mixes, as well as the modulus of elasticity for each concrete at tensioning.

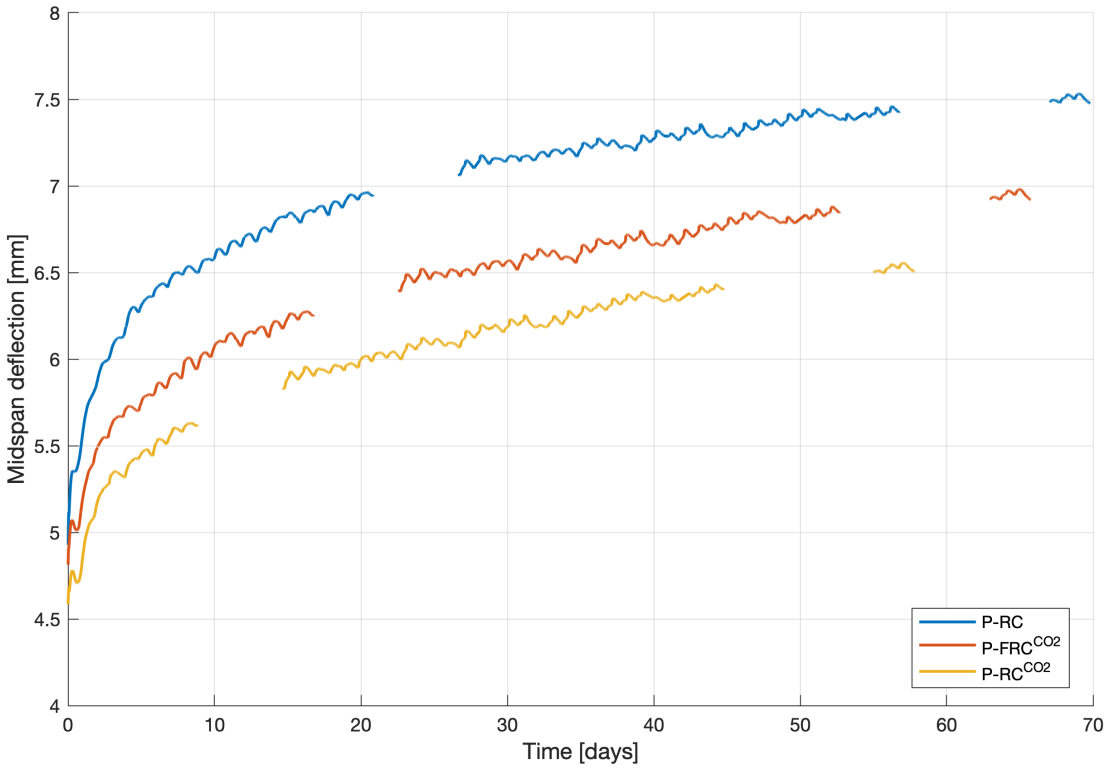

Figure 5.6: Midspan deflection over time for all three beam specimens.

The increase in upward deflection may initially appear counterintuitive, as the top of the beam gradually changes from being in tension to being in compression. This can be observed in Figure 4.3, where the beam starts with a small positive strain at the top of 20 to 40 $\mu\varepsilon$ and end with a compression strain of approximately -150 to -275 $\mu\varepsilon$, depending on the specimen. This behaviour is initially caused by concrete shrinkage, which generates compressive stresses throughout the cross-section, together with pre-stress relaxation, as the tendons gradually lose force and therefore induce less upward action on the beam.

Although the entire cross-section remains in compression, the stress distribution is not uniform. The bottom fibres are subjected to higher compressive stresses than the top fibres, resulting in different creep development throughout the section. Since creep follows the stress state and increases with stress level, the bottom fibres experience greater creep development than the top fibres. This differential creep causes an increase in curvature, leading to a continued upward bending of the beam over time, as seen in Figure 5.6.

5.2.2 Creep and Shrinkage Strain Over Time

The measured creep and shrinkage cylinder test strains were used to separate the time-dependent strain components. Due to experimental failure during testing of the P-RC^{CO_2} specimen, data for the shrinkage of the P-RC^{CO_2} was not obtained. Therefore, it was not possible to separate the measured strain into creep and shrinkage components, unlike for the P-RC specimen. Consequently, the creep strain could not be determined directly from experimental measurements. Instead, it was assumed that the P-RC^{CO_2} specimen exhibits a shrinkage development similar to that of the P-RC specimen.

Hooton et al. (2004) reported that concrete mixtures in which cement is partially replaced with slag exhibit slightly higher drying shrinkage compared with conventional Portland cement concrete. However, the study also emphasized that the investigated specimens differed in aggregate content, where the slag concrete contained a lower aggregate ratio than the conventional concrete. The authors therefore suggested that mixtures with similar aggregate contents would likely exhibit similar drying shrinkage behaviour. In the present master thesis, the concrete mixtures were designed to be nearly identical, as shown in Appendix B, with less than 0.1% difference in aggregate content per unit volume [kg/m^3] between the P-RC and P-RC^{CO_2} mixtures. Furthermore, ACI Committee 233 (2003) concluded that slag concrete generally exhibits drying shrinkage similar to that of conventional Portland cement concrete. Together, these studies support the assumption that the shrinkage development in P-RC and P-RC^{CO_2} can be considered equivalent.

Based on this assumption, the creep and shrinkage strains could be decoupled for both P-RC and P-RC^{CO_2}. The decoupled results, together with analytical predictions according to Eurocode 2:2004 and Eurocode 2:2023, are presented in Figure 5.7 and Figure 5.8. Both Eurocode versions overestimate the measured strain development, which can be expected since the models are based on empirical data and are conservative design estimates. However, the new Eurocode follows the experimental strain development slightly better than the current version. The difference between the two codes is relatively small, particularly for creep, where the predicted creep strain differs by only 3-3.5% after 40 days. In comparison, the shrinkage strain differs by approximately 10-16% after 40 days when comparing the calculated Eurocode 2004 and 2023 strains for both concrete types. Therefore, the remaining calculations in this thesis were performed according to Eurocode 2 (EN 1992-1-1:2004).

Autogenous shrinkage begins immediately after casting and continues during the water-curing period of the cylinder specimens. Since the cylinder strains were reset to zero at the start of the creep–shrinkage test, the Eurocode predictions were adjusted accordingly. To achieve comparable results, the autogenous shrinkage strain accumulated during the initial 29 days was removed from the total calculated strain so that the analytical curves also started at 0 $\mu\varepsilon$. Consequently, the experimentally measured strains shown in Figure 5.7 and 5.8 underestimate the total shrinkage strain.

The sudden decrease in strain at time zero in Figures 5.7 and 5.8 represents the instantaneous elastic strain caused by the applied load on the cylinders. This strain corresponds to approximately -135 $\mu\varepsilon$ and -133 $\mu\varepsilon$, which convert to stresses of approximately 4.7 MPa and 4.6 MPa, respectively, assuming a modulus of elasticity of 35 GPa. As described in Section 3.2.8, the cylinders were intended to be loaded to approximately 4.5 MPa. These results suggest that the actual modulus of elasticity may have been

slightly lower than expected, approximately 33 GPa and 34 GPa, respectively. When converting the measured hydraulic pressure in the creep–shrinkage setup, in Figure 4.5, to the stress applied to the cylinders, the estimated stress was approximately 4.2 MPa, which would indicate an even lower modulus of elasticity.

The mechanical strain represents the instantaneous elastic strain caused by loading and reflects the load-related response of the material. Over time, this strain gradually decreases due to stress redistribution associated with creep development. Since the measured strain exhibited small jumps immediately after loading for P-RC^{CO_2}, see Figure 5.8, the magnitude of the instantaneous elastic strain introduces some uncertainty in the estimated modulus of elasticity. Because the results from the secant modulus of elasticity tests were unreliable, no direct comparison could be made. Therefore, throughout this thesis, the modulus of elasticity was consistently determined from the measured compressive strength using the Eurocode relationships, resulting in a 28-day modulus of elasticity of approximately 35 GPa for both concrete types. It should be noted, as mentioned i Section 3.2.7, that the concretes used in this study were SCC with a maximum aggregate size of 8 mm. The predicted values in Table 3.7 may be slightly higher than the actual modulus of elasticity of the beams. This can be attributed to the lower aggregate content and higher paste content, including binder, water, and limestone filler, in SCC, which corresponds to the findings mentioned in the paragraph above, pointing to a lower modulus of elasticity than expected.

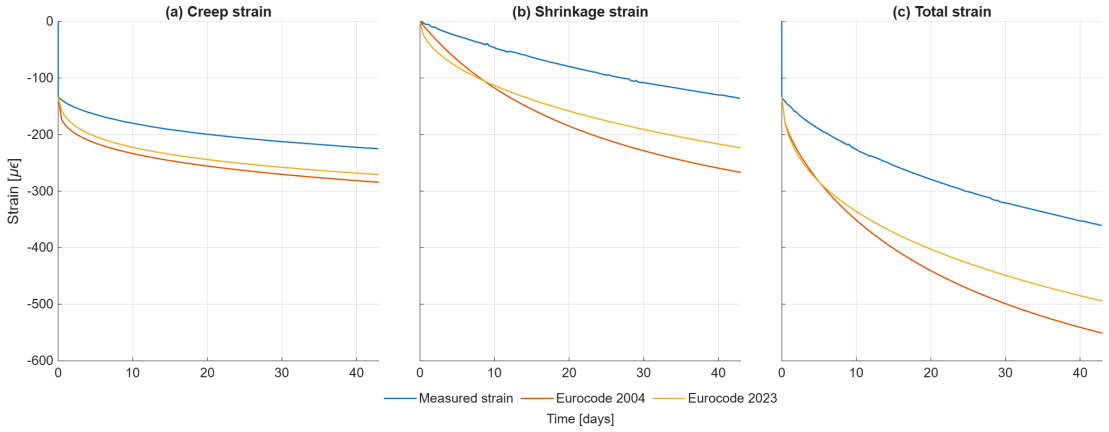

Figure 5.7: Measured strain for P-RC cylinder compared to Eurocode calculated strains from both current and new Eurocode. Figure a) shows the creep strain, figure b) shows the shrinkage strain and figure c) show the combined total strain.

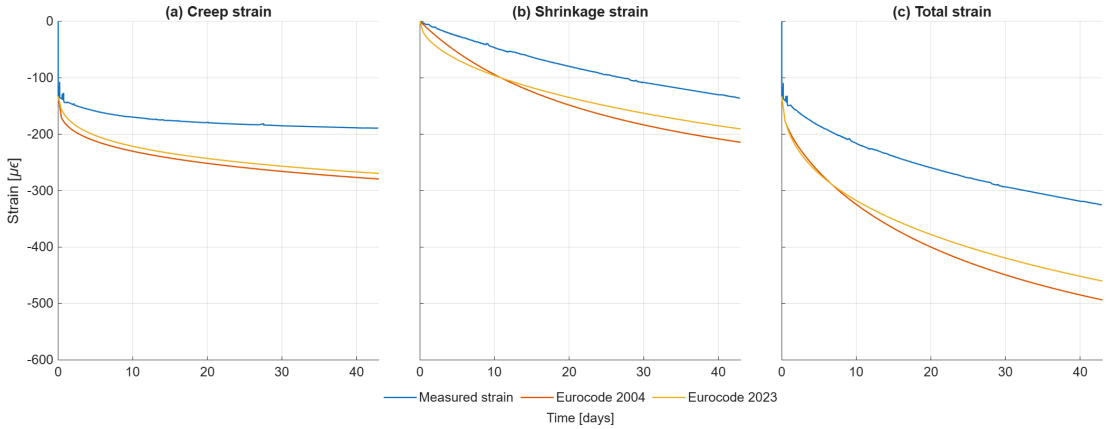

Figure 5.8: Measured strain for P-RC^{CO_2} cylinder compared to Eurocode calculated strains from both current and new Eurocode. Figure a) shows the creep strain, figure b) shows the shrinkage strain and figure c) show the combined total strain.

Regarding the different concrete cylinder specimens, the creep strain differed by approximately 16% after 40 days. This indicates that the creep development in the P-RC^{CO_2} specimen was lower than in the P-RC specimen. A similar trend can be observed for the beams where the total measured strain in the P-RC beam was approximately 20% greater after 40 days. It should be noted that differences in initial prestressing force also influence creep development. However, the P-RC beam was prestressed with a slightly larger prestressing force than the P-FRC^{CO_2} and P-RC^{CO_2} beam. Nevertheless, the creep–shrinkage cylinder tests indicated a difference in creep behaviour between the concrete types which is also reflected in the beam behaviour, despite the differences in initial prestressing force.

The measured cylinder strains were converted to the beam specimens according to the methods described in Section 3.3.2 in order to separate the beam strains into creep, shrinkage, and relaxation components. Figure 5.9 illustrates the resulting strain components for the P-RC beam, while Figure 5.10 presents the corresponding results for the P-RC^{CO_2} beam.

The relaxation strain is positive and therefore acts in the opposite direction to creep and shrinkage strains. Its magnitude is relatively small, making it the least influential strain component overall. The positive sign indicates that relaxation reduces the prestressing force in the tendons over time, thereby reducing the compressive stress in the concrete beam and partially counteracting the compressive strains caused by creep and shrinkage. The relaxation strain was calculated according to Eurocode 2:2004 for all evaluation methods (a-c). The difference regarding relaxation strains at 40 days between the concrete types was approximately 3%, primarily due to differences in the initial prestressing force. Compared with creep and shrinkage, relaxation contributed only marginally to the total strain development.

Among the individual strain components, creep had the largest contribution to the long-term deformation. The creep strain increased continuously over time, demonstrating that sustained loading caused significant additional deformation beyond the initial elastic response. According to ACI Committee 233 (2003), slag cement concrete cured in water exhibits a lower elastic modulus than conventional Portland cement concrete at early ages. However, at later ages, the slag concrete surpasses conventional concrete in

elastic modulus due to its more pronounced later-age strength development. The report also notes that specimens subjected to air drying do not exhibit the same relationship. This can explain why the P-RC^{CO_2} cylinder specimens experienced less creep than the P-RC specimens, since both were water-cured for 29 days.

A similar trend can be observed in Table 3.7, where the P-RC^{CO_2} concrete exhibited lower compressive strength than the P-RC concrete at 3 and 7 days, but slightly higer compressive strength than the P-RC concrete at 28 days. Since a higher elastic modulus generally results in lower creep strain, this behaviour supports the observed reduction in creep for the P-RC^{CO_2} concrete.

If the creep behaviour of air-dried slag concrete differs, as described by ACI Committee 233 (2003), this could imply that the converted creep strain in the P-RC^{CO_2} beam is underestimated. On the other hand, the experimental results indicate that the P-RC^{CO_2} beam exhibited a lower total measured strain overall and a flatter strain development curve compared with the P-RC beam, see Figure 5.9 and Figure 5.10. This behaviour can be related to the curing conditions, since the P-RC^{CO_2} beam remained in its form under plastic sheeting until day 7, whereas the P-RC beam remained covered only until day 3. Consequently, the P-RC^{CO_2} beam was protected from drying during the early ages, potentially producing effects similar to those observed for water-cured slag concrete in ACI Committee 233 (2003).

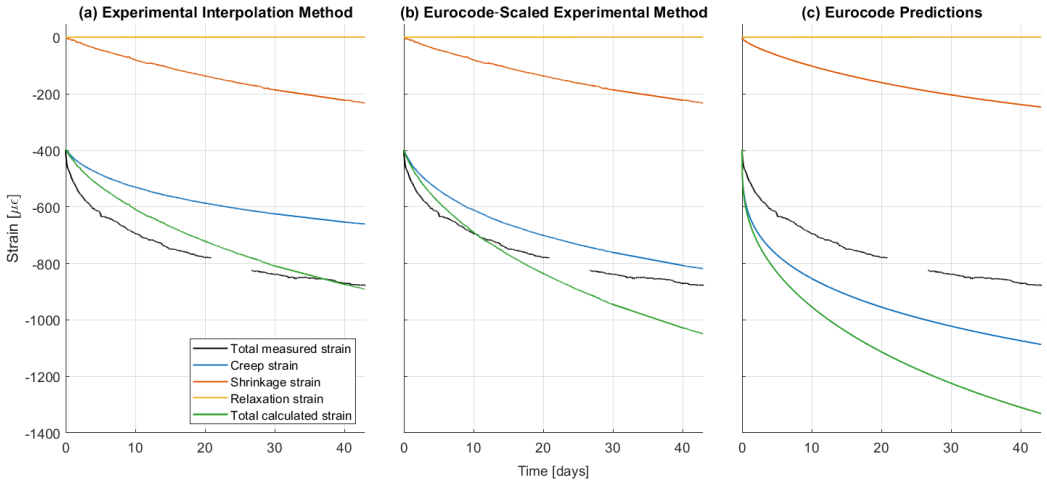

Figure 5.9: P-RC beam strains, showing creep, shrinkage and relaxation strains calculated with two different methods and Eurocode 2.

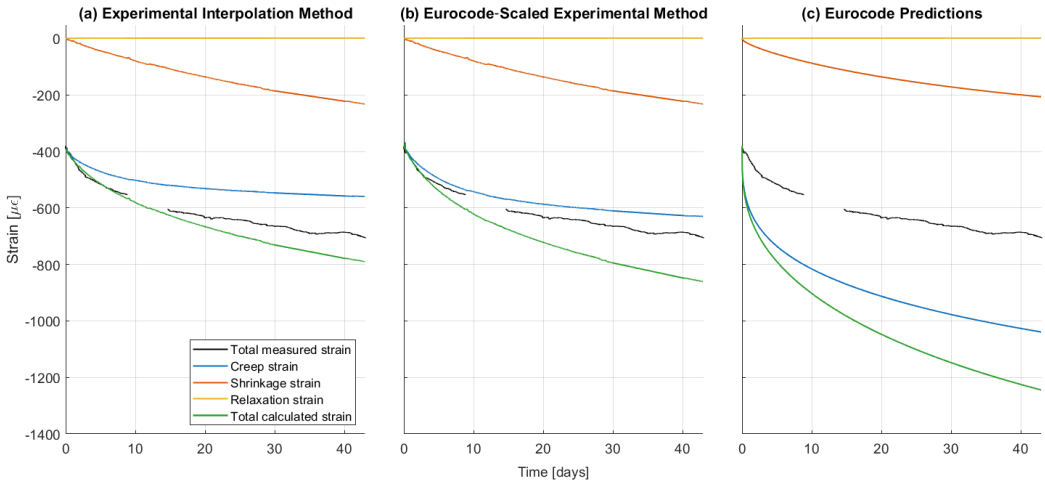

Figure 5.10: P-RC^{CO_2} beam strains, showing creep, shrinkage and relaxation strains calculated with two different methods and Eurocode 2.

The Experimental Interpolation Method and the Eurocode-Scaled Experimental Method produced strain developments that were more similar to the measured beam strains than the direct Eurocode predictions, as illustrated in Figure 5.11. This can be attributed to the fact that these methods depend on the actual strain behaviour of the concrete, whereas the Eurocode is primarily based on empirical data. However, both experimental methods underestimated the early-age behaviour of the P-RC beams and later overestimated the total strain. For the P-RC^{CO_2} beams, the total strain was consistently overestimated throughout the entire measurement period. Although the creep conversion methods account for differences in loading age through creep development functions, the results remain dependent on the measured strains and their rate of development. The creep strains were converted using data from cylinders loaded at 29 days, when the concrete had attained higher strength and stiffness than the beams loaded at 3 and 7 days. This may have led to an overestimation of the modulus of elasticity for the early-age beams and, consequently, an underestimation of the creep development during the early ages.

When comparing the concrete types, both the experimental conversion methods and the Eurocode predictions overestimated the strain development of the P-RC^{CO_2} beams more than that of the P-RC beams. This can be because both approaches are based on the 28-day compressive strength and therefore fail to account for the continued rapid strength gain of the P-RC^{CO_2} concrete. Consequently, the creep strains are overestimated to a greater extent for P-RC^{CO_2} than for P-RC.

The Eurocode predictions and the method conversions do not account for the amount of reinforcement or the stress transfer between the concrete and the reinforcing steel. According to Williams et al. (2024), heavily reinforced structures exhibit reduced time-dependent deformation due to the composite interaction between steel and concrete, which restrains the free creep and shrinkage strains assumed in the Eurocode models. Since the beams investigated in this thesis were heavily reinforced, the Eurocode models and conversion methods tended to overestimate the total strain development.

Furthermore, the Eurocode models do not consider the influence of the high-quality dense aggregates commonly used in Sweden. Such aggregates reduce deformation

within the cement paste and thereby limit the development of creep and shrinkage strains. In contrast, the conversion methods applied in this study were based on experimentally measured beam strains and therefore inherently accounted for the aggregate quality.

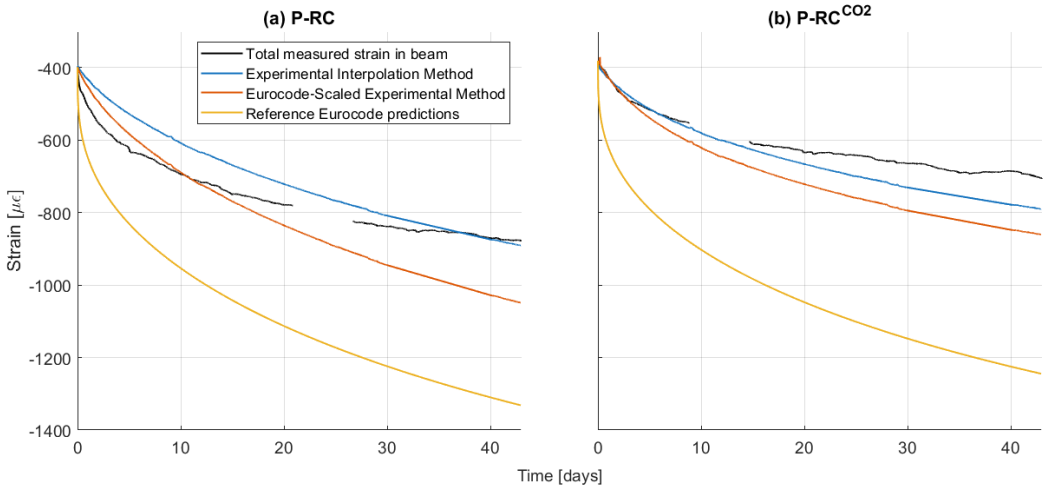

Figure 5.11: Total strain calculated with three different methods.

Overall, the results indicate that the P-RC^{CO_2} concrete exhibited reduced creep development compared to the conventional P-RC concrete, since lower time-dependent strains can reduce prestress losses and long-term deflections this is be beneficial for prestressed structures. While the experimentally based conversion methods provided a closer representation of the beam behaviour, the Eurocode models generally overestimated the measured strains indicating that the aggregate and reinforcement amount needs to be taken into account for a better prediction. However, uncertainties related to shrinkage assumptions and curing conditions should be considered when interpreting the results.

5.2.3 Force Loss Over Time

The prestress force losses over time are directly influenced by the time-dependent behaviour of the concrete and prestressing steel, as these mechanisms induce strains that gradually reduce the effective prestressing force. In general, larger induced strains result in greater force losses. This behaviour is illustrated in Figure 5.12, where the increase in force loss over time is shown for the different specimens. The force loss due to creep and shrinkage has been determined using Equation 3.7.

As shown in the figure, the P-RC specimen exhibits the largest force loss over time, whereas the P-FRC^{CO_2} and P-RC^{CO_2} specimens show the smallest. This trend corresponds to the stress levels in the beams, as the P-RC specimen was subjected to the highest prestressing stress. Higher stress levels are known to amplify creep effects, which explains the observed differences between the specimens.

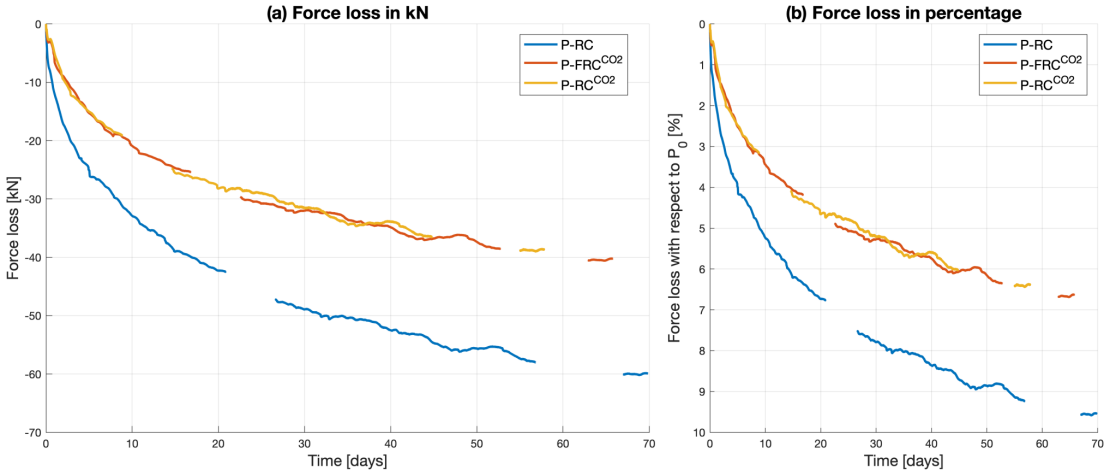

Figure 5.12: Force loss over time at the midspan cross section for all three beam types using curvature for the force loss calculation.

Figure 5.13 shows the difference between the two methods possible to use for calculating the force loss in the beam as presented in Fernandez et al. (2025). In the darker color the method based on the strain interpolated from the curvature derived from the top and bottom DOFS measurements and in the lighter shade the obtained results from directly using the DOFS attatched to the duct. As expected the curvature method gave a slightly larger force loss which matches the results in Fernandez et al. (2025). Both methods were initially applied to verify this consistency, however, the curvature-based method was subsequently used for further analysis. This approach was preferred due to its greater practicality, as it reduces the required length of DOFS only needing it at the top and bottom reinforcement. Hence, this is the method used in Figure 5.13 and consequently for the following figures.

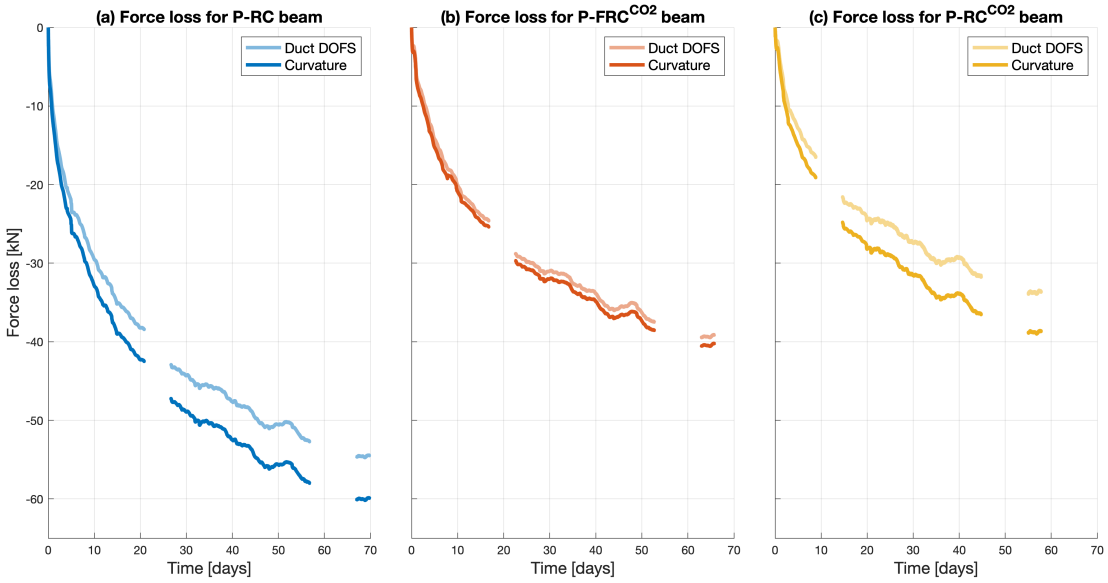

Figure 5.13: Force loss over time at the midspan cross section for (a) P-RC, (b) P-FRC^{CO_2} and (c) P-RC^{CO_2} for the two methods, curvature and duct DOFS, used in Fernandez et al. (2025).

The comparison between the curvature based force loss and analytical Eurocode 2 based

calculation is shown in Figure 5.14. For all of the specimens the Eurocode-based formulation results in higher estimated prestress losses compared to the curvature-based approach. This indicates that the Eurocode formulation provides a more conservative estimate than the experimentally derived response of the beams.

A possible explanation for this difference is that the Eurocode model does not fully account for structural effects, such as restraint within the cross-section due to reinforcement and the interaction between the prestressing steel and the surrounding concrete. As a result, the model tends to overestimate the strain development, leading to larger predicted force losses. In contrast, the curvature-based method is derived from measured strain distributions and therefore reflects the actual structural behaviour of the beam. This includes the influence of geometry, sectional stiffness, and internal restraint, which can limit the development of creep and shrinkage strains.

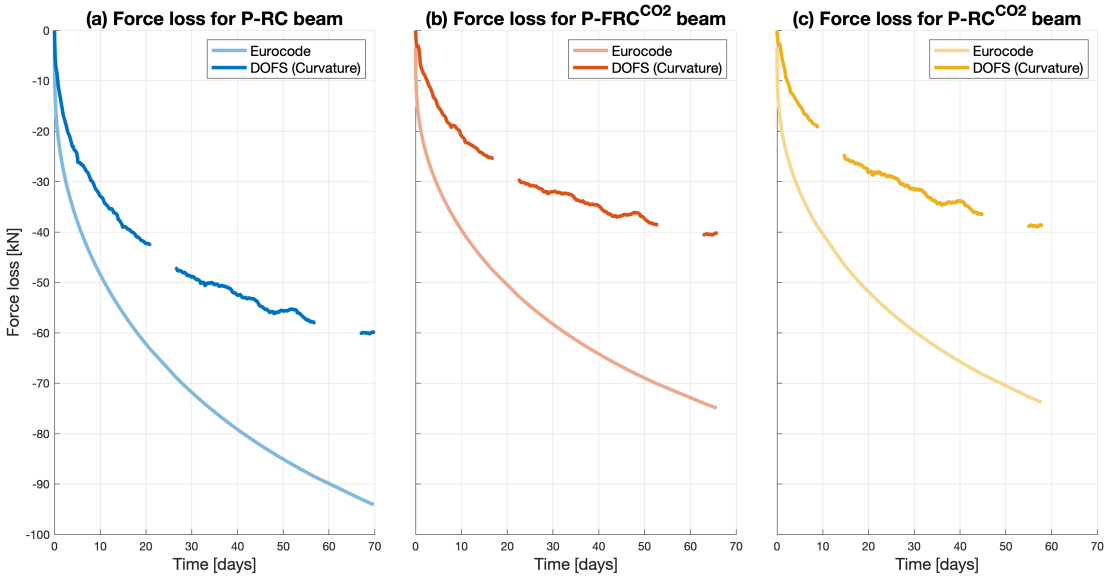

Figure 5.14: Force loss over time at the midspan cross section for (a) P-RC and (b) P-FRC^{CO_2} and (c) P-RC^{CO_2} comparing the obtained force loss for the beam with the one calculated using Eurocode 2.

The different methods used to determine the creep and shrinkage of the beam, see Section 3.3.2, have been applied to calculate the corresponding prestress force losses using Equation 3.8. The results are presented in Figure 5.15. For both beam types, a consistent trend is observed: the reference Eurocode prediction yields the highest estimated losses, followed by the Eurocode-scaled experimental method, and lastly the experimental interpolation method. A similar trend is evident in Figures 5.9 and 5.10, where larger estimated creep strains correspond to larger predicted force losses. This highlights the strong dependency of the calculated prestress force loss on the assumed creep behaviour.

It should be noted that the same force loss formulation, given by Equation 3.8, is used for all methods, including the reference Eurocode calculation. The differences between the approaches therefore originate from the input parameters, namely the shrinkage strain and the creep coefficient. While the shrinkage strains are identical for two of the methods and differ only from the Eurocode prediction, the creep coefficient varies across all three approaches.

As discussed previously, the differences observed between the P-RC and P-RC^{CO_2} specimens are mainly attributed to the initial prestressing force and the development of the modulus of elasticity, which influence both the stress level and the resulting time-dependent deformations.

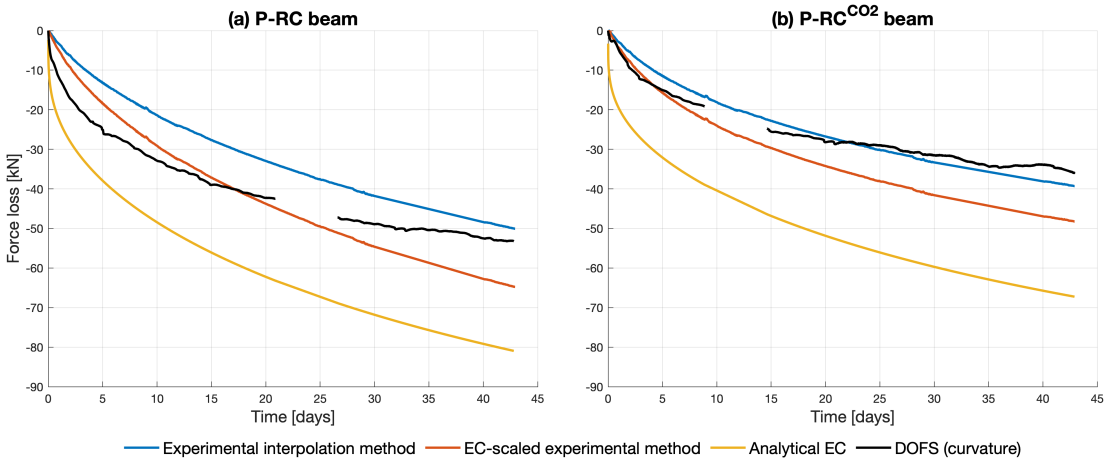

Figure 5.15: Comparison of prestress force losses for (a) P-RC, (b) P-RC^{CO_2} beams obtained using analytical, experimental, and curvature-based methods.

5.3 Experimental Limitations and Uncertainties

Several sources of uncertainty and limitations were identified in the experimental setup and subsequent analysis, which should be considered when interpreting the results. One important limitation, as discussed previously, was the absence of load cell data for the tensioning of the P-FRC^{CO_2} and P-RC^{CO_2} beams. As a result, the tendons were tensioned to an approximate pressure rather than an exact force indicated by the load cell. Consequently, the prestressing force introduced in each beam was not as consistent as initially intended. If the applied forces had been more similar, it would have been easier to compare the effect of creep, as it is directly load-dependent. Furthermore, complete load data would have allowed for a more detailed evaluation of friction losses, including whether the same trend of decreasing friction loss, as presented in Figure 5.3, was present for all beams and whether the assumed linear distribution is valid.

Another source of uncertainty was the lack of measured shrinkage data for the P-RC^{CO_2} beam. This required an assumption that the shrinkage behaviour is similar to that of the P-RC specimen. Although this assumption is supported by available literature, it cannot be verified with complete certainty, which introduces additional uncertainty into the results. In addition, the beams and the corresponding cylinders were loaded at different times, meaning that time-dependent effects had to be adjusted for differences in age at loading. This further contributes to the overall uncertainty and could have been reduced if all specimens had been loaded simultaneously.

The experimental setup itself also introduced uncertainties. Since the formwork was constructed manually, small deviations in geometry are unavoidable. Similarly, the placement of the duct and reinforcement cannot be assumed to be perfectly accurate. These factors may influence the stress distribution and contribute to variability in the calculated prestressing force.

Further uncertainties were associated with the determination of the modulus of elastic-

ity. The measured values were significantly lower than expected at the corresponding age of the concrete, indicating potential errors in the testing procedure. The measurement setup included only two displacement gauges, whereas at least three are typically required to minimise errors due to eccentric loading. As a result, there is a risk of either underestimating or overestimating the modulus of elasticity.

In addition, the specimens were stored in a horizontal position, which may have introduced eccentricities due to material inhomogeneities, such as segregation or an uneven distribution of air voids. These factors could have influenced the accuracy of the measurements and may partly explain the unexpectedly low values of the modulus of elasticity obtained from the tests.

Due to the relatively small size of the specimens and the uncertainty in the measurements, the modulus of elasticity used in the calculations was instead determined from the compressive strength tests using the conversion formula provided in Eurocode 2. This approach was considered to provide a reasonable approximation of the modulus of elasticity. However, a direct experimental determination would have been preferable, as it would better reflect the actual material behaviour of the specimens.

Finally, the limited number of specimens represented an important constraint. Only one beam of each type was tested, which restricts the ability to generalise the results. Additional specimens would have been required to assess the variability and reproducibility of both the structural behaviour and the material properties obtained from the cylinders.

5.4 Implications for Design and Practice

The results obtained in this study provide several important implications for the design and assessment of post-tensioned concrete structures. Firstly, the comparison between the different methods used for the analysis shows that the Eurocode-based approach consistently results in more conservative predictions than those derived from the DOFS measurements. While conservative assumptions are generally applied in structural design to ensure safety, the degree of conservatism should be well understood and reasonably bounded. In practical design, additional safety margins are already introduced through material models, characteristic values and partial safety factors. Therefore, an excessively conservative prediction of, for example, prestress losses may lead to an overestimation of losses beyond what is necessary for safe design. This may result in unnecessary material use and less efficient structural solutions. Consequently, it is important not only to identify that a method is conservative, but also to evaluate the magnitude of this conservatism in relation to experimental observations.

In the context of current environmental challenges, this aspect becomes particularly relevant. Minimising material consumption is essential to reduce environmental impact. The results therefore highlight the importance of critically assessing code-based predictions and, where possible, complementing them with experimental or monitoring data to achieve both safe and resource-efficient designs.

Secondly, the results demonstrate that DOFS is capable of accurately capturing the structural behaviour of post-tensioned beams. The ability to monitor strain distribution, prestress losses, and overall structural response suggests that DOFS has significant potential not only in research but also for practical engineering applications. In particular, large-scale implementation of such monitoring systems could enable continuous or real-time assessment of structural performance, providing valuable information for

both design validation and long-term structural health monitoring.

With regard to material selection, the results indicate a difference in behaviour between the conventional concrete and the low-CO_2 concrete in terms of long-term response. The low-CO_2 concrete exhibited a tendency toward reduced creep development compared to the conventional concrete. This suggests that climate-improved concrete not only serves as a sustainable alternative to traditional concrete through reduced cement-related carbon emissions, but may also provide structural engineering advantages in prestressed concrete applications. One limitation of the low-CO_2 concrete is its slower development of strength at early ages, which can pose challenges in construction scenarios where rapid strength gain is required. However, from a broader perspective, this trade-off may be acceptable given the potential environmental benefits. In cases where construction schedules allow, the use of such materials could contribute to a reduction in the environmental impact of concrete structures without compromising performance.

6 Conclusion

In conclusion, the results of this study demonstrate that distributed optical fibre sensors (DOFS) are capable of accurately capturing strain development and the overall structural response of the beams during both tensioning and long-term behaviour.

The results from the tensioning phase showed behaviour that was consistent with theoretical expectations. The measured strains increased progressively as each tendon was tensioned, indicating a successful transfer of prestressing force to the beam. In addition, a reduction in friction losses was observed for successive tendons, suggesting that the tendon configuration within the duct became more favourable as tensioning progressed. The anchorage seating losses were found to be similar for all beams, indicating a consistent performance of the anchorage system.

Regarding the long-term behaviour, the measured strains increased continuously over time, which was consistent with the expected effects of creep and shrinkage in concrete. The rate of strain development was higher at early ages and decreased over time, following the typical behaviour of time-dependent deformation. Furthermore, the results showed that larger initial prestressing forces resulted in greater prestress losses over time, highlighting the strong influence of stress level on creep behaviour.

The results obtained from the cylinder tests showed a similar general behaviour for both concrete types. However, slightly lower strain levels were observed for the low-CO_2 concrete. Assuming similar shrinkage behaviour, the results suggest that the low-CO_2 concrete exhibits a reduced creep response compared to conventional concrete.

Furthermore, the Eurocode-based approach was found to provide consistently higher estimates of prestress losses compared to the values derived from DOFS measurements, indicating a conservative prediction method.

Overall, the findings provide a consistent experimental basis for understanding both the immediate and time-dependent behaviour of post-tensioned concrete beams and highlight the importance of accurately accounting for prestress losses in structural design.

6.1 Recommendations for Future Work

To further validate the results presented in this study, additional experiments following a similar testing procedure are recommended. In particular, sources of uncertainty identified in the present study, such as missing load cell data, inaccuracies in the determination of the modulus of elasticity, and the lack of shrinkage data for the P-RC^{CO_2} specimen, should be addressed. Moreover, a larger dataset should be obtained in order to improve the reliability and statistical significance of the results.

Another area for future work is the implementation of the updated version of Eurocode (EN 1992-1-1:2023). In the present study, only a limited comparison was carried out for the cylinders. A more comprehensive evaluation of the updated provisions, particularly regarding creep and shrinkage modelling for the beams, could provide valuable insight into how these changes influence the estimation of prestress losses.

It would also be of interest to investigate how varying the amount and type of SCMs, such as GGBFS, affects the long-term behaviour of concrete. This could be achieved by testing a wider range of cylinder specimens with different proportions of slag, al-

lowing for a more detailed assessment of its influence on creep, shrinkage, and strength development.

As a continuation of the SBUF project (14134), the same experimental programme could be repeated using prestressing tendons made of fibre-reinforced polymer (FRP) instead of steel. This would enable a comparison of prestress losses over time between different tendon materials. Additionally, the use of non-corrosive tendons such as FRP could potentially contribute to an increased service life of structures, as deterioration due to corrosion may be significantly reduced.

7 References

ACI Committee 233. (2003). *ACI 233R-03: Slag Cement in Concrete and Mortar* (ACI Report). American Concrete Institute. Farmington Hills, MI.

ACI Committee 544. (2001). *ACI 544.1R-96: State-of-the-art report on fiber reinforced concrete* (tech. rep.) (Reapproved 2002). American Concrete Institute. Farmington Hills, MI.

Al-Emrani, M., Engström, B., Johansson, M., & Johansson, P. (2013). *Bärande konstruktioner del 1* (tech. rep. No. 2013:1). Chalmers University of Technology. Gothenburg, Sweden.

Almgren, T., Green, T., Norlén, B., Pyykkö, J., Rapp, T., Schoug, B., Sköld, M., & Åström, J. (2018). *Betong och armeringsteknik: Normer och standader, materialegenskaper och grundläggande hållfasthetslära, utförande och produktionsmetoder, kontroll och provning*. Sveriges Byggindustrier.

Belie, N. D., Soutsos, M., & Gruyaert, E. (2018). *Properties of frech and hardened concrete conatinging supplementary cementitious materials: State-of-the-art report of the rilem technical committee 238-scm, working group 4*. Springer Cham. doi: https://doi.org/10.1007/978-3-319-70606-1.

Berrocal, C. G., Fernandez, I., Bado, M. F., Casas, J. R., & Rempling, R. (2021). Assessment and visualization of performance indicators of reinforced concrete beams by distributed optical fibre sensing. *Structural Health Monitoring*, *20*(6), 3309–3326. doi: 10.1177/1475921720984431.

Berrocal, C. G., Fernandez, I., & Rempling, R. (2021). Crack monitoring in reinforced concrete beams by distributed optical fiber sensors. *Structure and Infrastructure Engineering*, *17*(1), 124–139. doi: 10.1080/15732479.2020.1731558.

Berrocal, C. G., Flansbjer, M., Ekström, D., Rempling, R., & Fernandez, I. (2025). Application of dofs for monitoring post-tensioned anchorage zones in reinforced and fibre reinforced concrete. *Journal of Civil Structural Health Monitoring*, *15*. doi: 10.1007/s13349-025-00937-7.

CCL International. (2021). *Ccl post-tensioning systems: Civil engineering construction* [Brochure].

Collins, M. P., & Mitchell, D. (1991). *Prestressed concrete structures*. Prentice-Hall.

de la Fuente, A., Monserrat-López, A., Tošic´, N., & Serna, P. (2023). Design of steel fibre reinforced concrete structures according to the annex l of the eurocode-2 2023. *Hormigón y Acero, the journal of the Spanish Association of Structural Engineering (ACHE)*, *74*(299-300), 169–186. doi: 10.33586/hya.2023.3124.

Engström, B. (2011). *Design and analysis of prestressed concrete structures* (tech. rep. No. 2011:7). Chalmers University of Technology. Gothenburg, Sweden.

Engström, B. (2014). *Restraint cracking of reinforced concrete structures* (tech. rep. No. 2007:10). Chalmers University of Technology. Gothenburg, Sweden.

European Committee for Standardization. (2004). EN 1992-1-1: Eurocode 2 - design of concrete structures. Part 1-1: General rules for buildings [European Standard].

European Committee for Standardization. (2009). EN 10138-3: Steel for the prestressing of concrete.Part 3: Strand [European Standard].

European Committee for Standardization. (2019a). EN 12390-16: Testing hardened concrete - Part 16: Determination of creep of concrete in compression [European Standard].

European Committee for Standardization. (2019b). EN 12390-17: Testing hardened concrete - Part 17: Determination of shrinkage of concrete [European Standard].

European Committee for Standardization. (2019c). EN 12390-3: Testing hardened concrete - Part 3: Compressive strength of test specimens [European Standard].

European Committee for Standardization. (2021). EN 12390-13: Testing hardened concrete - Part 13: Determination of secant modulus of elasticity in compression [European Standard].

European Committee for Standardization. (2023). EN 1992-1-1: Eurocode 2 - design of concrete structures. Part 1-1: General rules and rules for buildings, bridges and civil engineering structures [European Standard].

Fernandez, I., Ekström, D., Rempling, R., & Berrocal, C. G. (2025). Evaluation of post-tensioned reinforced and fiber reinforced concrete beams by using dofs. *Structural Concrete*, *26*(5), 6274–93. doi: 10.1002/suco.70224.

Glišić, B., Hubbell, D., Sigurdardottir, D. H., & Yao, Y. (2013). Damage detection and characterization using long-gauge and distributed fiber optic sensors. *Optical Engineering*, *52*(8), 087101. doi: 10.1117/1.OE.52.8.087101.

Glišić, B., & Inaudi, D. (2007). *Fibre optic methods for structural health monitoring*. John Wiley & Sons Ltd.

Hong, S. (2017). Effect of prestress levels and jacking methods on friction losses in curved prestressed tendons. *Applied Science*, *7(8)*(824), 169–186. doi: 10.3390/app7080824.

Hooton, R. D., Stanish, K., & Prusinski, J. (2004). *The effect of ground, granulated blast furnace slag (slag cement) on the drying shrinkage of concrete: A critical review of the literature* (tech. rep.). University of Toronto and Slag Cement Association.

Jeon, S.-J., Park, S. Y., Kim, S.-H., Kim, S. T., & Park, Y. (2015). Estimation of friction coefficient using smart strand. *International Journal of Concrete Structures and Materials*, *9*(3), 369–379. doi: 10.1007/s40069-015-0112-9.

Luna Innovations. (2022, March). *ODiSI 6000 Series: Optical Distributed Sensor Interrogators* [Product data sheet]. Luna Innovations.

Mathern, A., Fall, D., Larsson, T., Gil, C., Ekström, D., Dackman, D., Rempling, R., & Fernandez, I. (2024). *Fiberarmering i kombination med efterspänning* (tech. rep. No. 14134). Svenska Byggbranschens Utvecklingsfond (SBUF).

Monteiro, P. J. M., Miller, S. A., & Horvath, A. (2017). Towards sustainable concrete. *Nature Materials*, *16*, 698–699. doi: 10.1038/nmat4930.

Singh, H. (2016). *Steel fiber reinforced concrete: Behaviour, modelling and design*. Springer Singapore. doi: https://doi.org/10.1007/978-981-10-2507-5.

Solifos AG. (2025). *BRUsens - DSS V9 Strain Sensing Cable* [Product data sheet, DB5024 Rev. 07]. Solifos AG.

Svensk Betong. (2025). *Vägledning klimatförbättrad betong: Utgåva 2* (tech. rep.) (Published July 2025). Svensk Betong. Stockholm, Sverige.

Svensk Byggtjänst. (2017). *Betonghandboken material del 1: Delmaterial samt fäsk och hårdnande betong*.

Thomas Concrete Group. (2022). *Teknisk information: Slagg bremen* [Revised 2022-12-12]. Thomas Concrete Group. Gothenburg, Sweden.

Williams, M., Menon, D., & Prasad, A. M. (2024). Creep and shrinkage in prestressed concrete beams: An experimental study. *Structural Concrete*, *25*(4), 2400–2419. doi: https://doi.org/10.1002/suco.202300625.

A Design Calculations

Design calculations according to Eurocode 2 produced in MathCad.

1 Material

1.1 Concrete

$\rho_c := 2500 \ \frac{kg}{m^3}$

28 days

$f_{cm.kub} := 52.2 \ MPa$

$f_{cm} := \frac{f_{cm.kub}}{1.2} = 43.5 \ MPa$

$f_{ctm} := 0.3 \cdot \left(\frac{f_{cm} - 8 \ MPa}{MPa} \right)^{\frac{2}{3}} \cdot MPa = 3.2 \ MPa$

$E_{cm} := 22 \cdot \left(\frac{f_{cm}}{10 \ MPa} \right)^{0.3} GPa = 34.2 \ GPa$

$\varepsilon_{cu} := 3.5 \cdot 10^{-3}$

$\sigma_{cc\infty.max} := 0.6 \cdot f_{cm} = 26.1 \ MPa$

$\sigma_{cci.max} := 0.45 \cdot f_{cm} = 19.6 \ MPa$

$\sigma_{ct\infty.max} := f_{ctm} = 3.2 \ MPa$

$\sigma_{cti.max} := f_{ctm} = 3.2 \ MPa$

7 days

$\beta_7 := exp\left(0.25 \cdot \left(1 - \left(\frac{28}{7} \right)^{\frac{1}{2}} \right) \right) = 0.78$

$f_{cm7} := \beta_7 \cdot f_{cm} = 33.9 \ MPa$

$f_{ctm7} := 0.3 \cdot \left(\frac{f_{cm7} - 8 \ MPa}{MPa} \right)^{\frac{2}{3}} \cdot MPa = 2.6 \ MPa$

$E_{cm7} := 22 \cdot \left(\frac{f_{cm7}}{10 \ MPa} \right)^{0.3} GPa = 31.7 \ GPa$

$\sigma_{cci.max7} := 0.45 \cdot f_{cm7} = 15.2 \ MPa$

$\sigma_{cti.max7} := f_{ctm7} = 2.6 \ MPa$

$Beta := exp\left(0.25 \cdot \left(1 - \left(\frac{28}{14} \right)^{\frac{1}{2}} \right) \right) = 0.902$

$f_{cm14} := Beta \cdot f_{cm} = 39220812.9 \ \frac{N}{m^2}$

$f_{ctm14} := 0.3 \cdot \left(\frac{f_{cm14} - 8 \ MPa}{MPa} \right)^{\frac{2}{3}} \cdot MPa = 2974523.4 \ \frac{N}{m^2}$

$E_{cm14} := 22 \cdot \left(\frac{f_{cm14}}{10 \ MPa} \right)^{0.3} GPa = 33149551585.6 \ \frac{N}{m^2}$

$\sigma_{cci.max7} := 0.45 \cdot f_{cm14} = 17649365.8 \ \frac{N}{m^2}$

$\sigma_{cti.max7} := f_{ctm14} = 2974523.4 \ \frac{N}{m^2}$

1.2 Reinforcing steel

$f_{ym} := 550\ MPa$

$E_s := 200\ GPa$

$\phi := 16\ mm$ $\quad A_{s.i} := \frac{\phi^2}{4} \cdot \pi = 201\ mm^2$

$n_s = 7$ $\quad A_s := n_s \cdot A_{s.i} = 1407\ mm^2$

$n'_s = 7$ $\quad A'_s := n'_s \cdot A_{s.i} = 1407\ mm^2$

$A_{s.tot} := A_s + A'_s = 2815\ mm^2$

$\phi_w = 8\ mm$

$c := 20\ mm$

$\alpha_s := \frac{E_s}{E_{cm}} = 5.8$

$\rho_s := 7850\ \frac{kg}{m^3}$

1.3 Prestressing steel

Post-tensioning system - Strand properties.

Steel designation	Y1860S7
Nominal diameter	15.7 mm
Tensile strength, f_{puk}	1860 MPa
Steel area, A_{pi}	150 mm^2
Breaking load, $f_{puk} \cdot A_{pi}$	279 kN
0.1 % proof load	246 kN
Max strand load, $0.8 \cdot f_{puk} \cdot A_{pi}$	221 kN

$E_p := 195\ GPa$

$\mu := 0.19$

$k := 0.0075$

$f_{pum} := 1986\ MPa$ $\quad f_{p0.1m} := 0.88 \cdot f_{pum} = 1748\ MPa$ $\quad \varepsilon_{p0.1m} := \frac{f_{p0.1m}}{E_p} = 8.96 \cdot 10^{-3}$

$\varepsilon_{uk} := 3.5\%$

$\chi_{1000} := 2.5\%$

$\phi_p := 15.7\ mm$

$A_{p.i} := 150\ mm^2$

$n_p = 4$

$A_p := n_p \cdot A_{p.i} = 600\ mm^2$

$\alpha_p := \frac{E_p}{E_{cm}} = 5.7$

$P_{i.max} := 0.8 \cdot f_{pum} \cdot A_{p.i} = 238.3\ kN$

XM20 achorage from the manufacturer CCL.

$\phi_{duct.out} := 59\ mm$

$\phi_{duct.in} := 48\ mm$

$t_{duct} := 2\ mm$

$A_{duct} := 1800\ mm^2$

2 Geometry

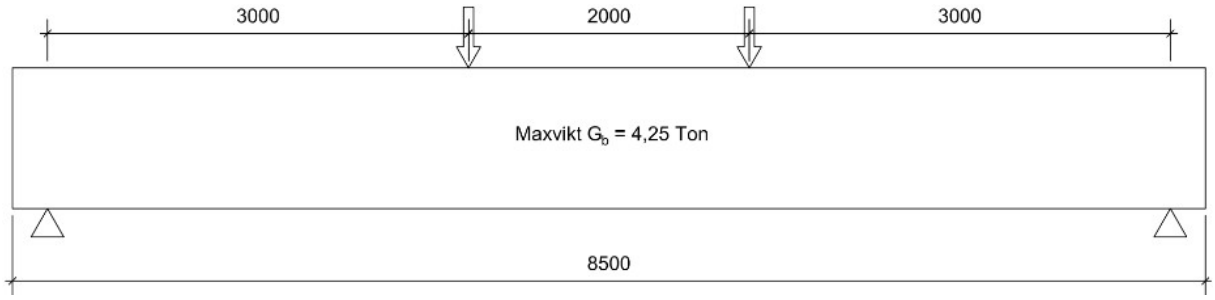

$l_{tot} := 8.5\ m$

$l := 8\ m$

$l_1 := 3\ m$

$l_2 := 2\ m$

$l_3 := 3\ m$

$b_{tf} = 320\ mm$	$h_{tf} = 120\ mm$	Top flange
$b_w = 150\ mm$	$h_w = 400\ mm$	Web
$b_{bf} = 0.3\ m$	$h_{bf} = 0.1\ m$	Bottom flange

Triangles:

$b_{t.trig} := \frac{b_{tf} - b_w}{2} = 85\ mm$	$h_{t.trig} := 25\ mm$	Top triangle
$b_{b.trig} := \frac{b_{bf} - b_w}{2} = 85\ mm$	$h_{b.trig} := 25\ mm$	Bottom triangle

$h := h_{tf} + h_w + h_{bf} = 640\ mm$ Total height

$d := h - c - \phi_w - \frac{\phi}{2} = 604\ mm$	$d' := c + \phi_w + \frac{\phi}{2} = 36\ mm$	Effective height

3 Sectional constants

$e_p = 230\ mm$ $P_{i.i} = 160\ kN$ $P_{i.I} := P_{i.i} \cdot n_p = 640\ kN$ Eccentricity of tendon and prestressing (iterative)

3.1 Areas and centroids

$A_{tf} := b_{tf} \cdot h_{tf} = 38400\ mm^2$ $y_{tf} := \frac{h_{tf}}{2} = 60\ mm$ Top flange

$A_w := b_w \cdot h_w = 60000\ mm^2$ $y_w := h_{tf} + \frac{h_w}{2} = 320\ mm$ Web

$A_{bf} := b_{bf} \cdot h_{bf} = 38400\ mm^2$ $y_{bf} := h_{tf} + h_w + \frac{h_{bf}}{2} = 580\ mm$ Bottom flange

$A_{t.trig} := \frac{b_{t.trig} \cdot h_{t.trig}}{2} = 1062.5\ mm^2$ $y_{t.trig} := h_{tf} + \frac{h_{t.trig}}{3} = 128.3\ mm$ Top triangle

$A_{b.trig} := \frac{b_{b.trig} \cdot h_{b.trig}}{2} = 1062.5\ mm^2$ $y_{b.trig} := h_{tf} + h_w - \frac{h_{b.trig}}{3} = 511.7\ mm$ Bottom triangle

$A_{duct} = 1800\ mm^2$ $y_{duct.net} := x_{net\_it} + e_p = 500.2\ mm$ Ducts

$y_{duct.I} := x_{I\_it} + e_p = 511.5\ mm$

$A_c := A_{tf} + A_w + A_{bf} + 2 \cdot A_{t.trig} + 2 \cdot A_{b.trig} = 0.14\ m^2$

$A_{net} := A_c - A_{duct} + (\alpha_s - 1) \cdot A_{s.tot} = 0.15\ m^2$

$A_I := A_c + (\alpha_p - 1) \cdot A_p + (\alpha_s - 1) \cdot A_{s.tot} = 0.16\ m^2$

$x_c := \frac{A_{tf} \cdot y_{tf} + A_w \cdot y_w + A_{bf} \cdot y_{bf} + 2 \cdot A_{b.trig} \cdot y_{b.trig} + 2 \cdot A_{b.trig} \cdot y_{b.trig}}{A_c} = 326\ mm$

$x_{net} := \frac{A_{tf} \cdot y_{tf} + A_w \cdot y_w + A_{bf} \cdot y_{bf} + 2 \cdot A_{b.trig} \cdot y_{b.trig} + 2 \cdot A_{b.trig} \cdot y_{b.trig} - A_{duct} \cdot y_{duct.net} + (\alpha_s - 1) \cdot A'_s \cdot d' + (\alpha_s - 1) \cdot A_s \cdot d}{A_{net}} = 323\ mm$

$x_I := \frac{A_{tf} \cdot y_{tf} + A_w \cdot y_w + A_{bf} \cdot y_{bf} + 2 \cdot A_{b.trig} \cdot y_{b.trig} + 2 \cdot A_{b.trig} \cdot y_{b.trig} + (\alpha_p - 1) \cdot A_p \cdot y_{duct.I} + (\alpha_s - 1) \cdot A'_s \cdot d' + (\alpha_s - 1) \cdot A_s \cdot d}{A_I} = 329\ m$

$e_{p.max} := h - x_c - c - \phi_w - \phi - \frac{\phi_{duct.out}}{2} = 241\ mm$

$e_{net} := h - x_{net} - c - \phi_w - \phi - \frac{\phi_{duct.out}}{2} = 243\ mm$

$e_I := h - x_I - c - \phi_w - \phi - \frac{\phi_{duct.out}}{2} = 238\ mm$

$d_p := x_c + e_p = 0.6\ m$

3.1.1 Control weight

$m_{beam} := \rho_c \cdot A_c \cdot l_{tot} = 2997.3\ kg$

$m_{beam} < 4.5\ tonne = 1$

3.2 Second moment of inertia

$$I_{tf} := \frac{b_{tf} \cdot h_{tf}^3}{12} + A_{tf} \cdot \left(x_c - y_{tf}\right)^2 \qquad I_{tf.net} := \frac{b_{tf} \cdot h_{tf}^3}{12} + A_{tf} \cdot \left(x_{net} - y_{tf}\right)^2 \qquad I_{tf.I} := \frac{b_{tf} \cdot h_{tf}^3}{12} + A_{tf} \cdot \left(x_I - y_{tf}\right)^2$$

$$I_w := \frac{b_w \cdot h_w^3}{12} + A_w \cdot \left(x_c - y_w\right)^2 \qquad I_{w.net} := \frac{b_w \cdot h_w^3}{12} + A_w \cdot \left(x_{net} - y_w\right)^2 \qquad I_{w.I} := \frac{b_w \cdot h_w^3}{12} + A_w \cdot \left(x_I - y_w\right)^2$$

$$I_{bf} := \frac{b_{bf} \cdot h_{bf}^3}{12} + A_{bf} \cdot \left(x_c - y_{bf}\right)^2 \qquad I_{bf.net} := \frac{b_{bf} \cdot h_{bf}^3}{12} + A_{bf} \cdot \left(x_{net} - y_{bf}\right)^2 \qquad I_{bf.I} := \frac{b_{bf} \cdot h_{bf}^3}{12} + A_{bf} \cdot \left(x_I - y_{bf}\right)^2$$

$$I_{t.trig} := \frac{b_{t.trig} \cdot h_{t.trig}^3}{36} + A_{t.trig} \cdot \left(x_c - y_{t.trig}\right)^2 = 41456613.1 \ mm^4$$

$$I_{t.trig.net} := \frac{b_{t.trig} \cdot h_{t.trig}^3}{36} + A_{t.trig} \cdot \left(x_{net} - y_{t.trig}\right)^2 = 40385791.7 \ mm^4$$

$$I_{t.trig.I} := \frac{b_{t.trig} \cdot h_{t.trig}^3}{36} + A_{t.trig} \cdot \left(x_I - y_{t.trig}\right)^2 = 42650918.5 \ mm^4$$ Top triangle

$$I_{b.trig} := \frac{b_{b.trig} \cdot h_{b.trig}^3}{36} + A_{b.trig} \cdot \left(x_c - y_{b.trig}\right)^2 = 36752281.2 \ mm^4$$

$$I_{b.trig.net} := \frac{b_{b.trig} \cdot h_{b.trig}^3}{36} + A_{b.trig} \cdot \left(x_{net} - y_{b.trig}\right)^2 = 37774073.6 \ mm^4$$

$$I_{b.trig.I} := \frac{b_{b.trig} \cdot h_{b.trig}^3}{36} + A_{b.trig} \cdot \left(x_I - y_{b.trig}\right)^2 = 35644320.4 \ mm^4$$ Bottom triangle

$$I_c := I_{tf} + I_w + I_{bf} + 2 \cdot I_{t.trig} + 2 \cdot I_{b.trig} = 0.00624 \ m^4$$

$$I_{net} := I_{tf.net} + I_{w.net} + I_{bf.net} + 2 \cdot I_{t.trig.net} + 2 \cdot I_{b.trig.net} - A_{duct} \cdot \left(x_{net} - y_{duct.net}\right)^2 = \left(6.18518 \cdot 10^9\right) \ mm^4$$

$$I_I := I_{tf.I} + I_{w.I} + I_{bf.I} + 2 \cdot I_{t.trig.I} + 2 \cdot I_{b.trig.I} + \left(\alpha_p - 1\right) \cdot A_p \cdot \left(y_{duct.I} - x_I\right)^2 = 0.00634 \ m^4$$

3 Load effects

$P_{qp} = 83\ kN$ $P_{Ed} := 300\ kN$

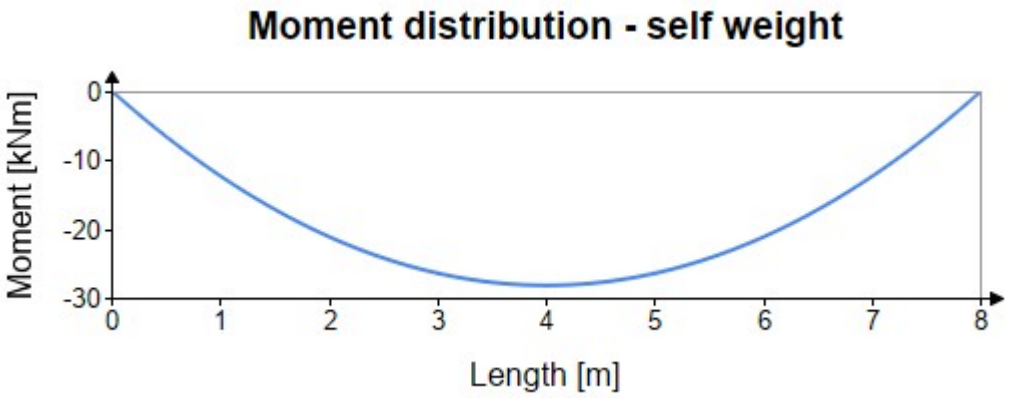

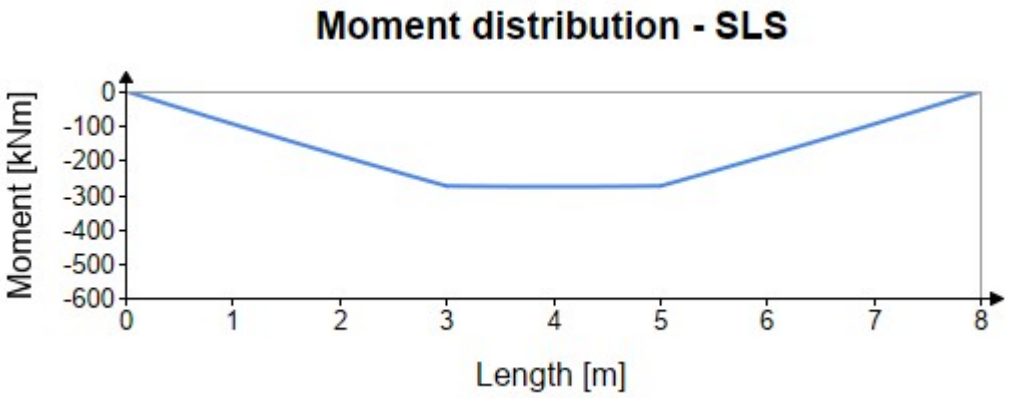

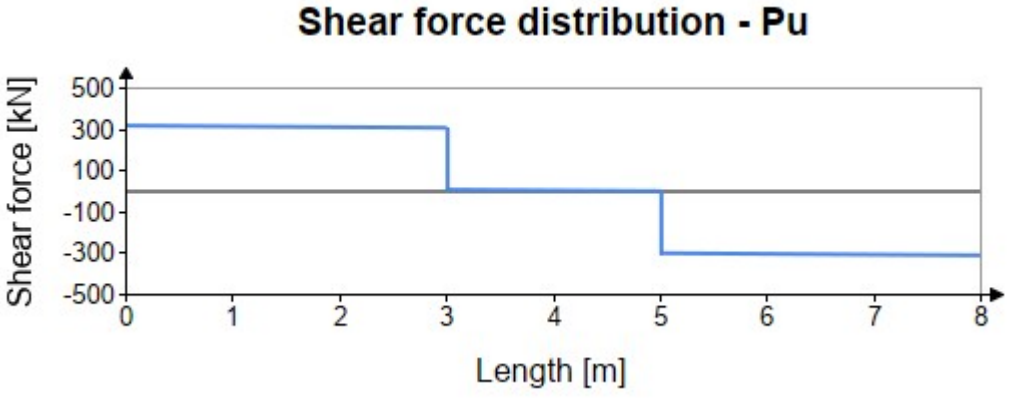

$M_{g0.max} = 28.2\ kN \cdot m$

$M_{qp.max} = 277.2\ kN \cdot m$

$V_{Ed.max} = 314.1\ kN$ $M_{Ed.max} = 928.2\ kN \cdot m$ for $P_u := P_{Ed} = 300\ kN$

---

4 Accurate design

4.1 Tendon force

$\mu = 0.19$ $k = 0.0075$ $\alpha := atan\left(\frac{e_p}{l_1}\right) = 4.4\ °$

$P_i := P_{i.1} \cdot e^{-\mu \cdot \left(\alpha + k \cdot \frac{l}{2\ m}\right)} = 627.2\ kN$

$\sigma_{cpi} := \frac{-P_i}{A_{net}} + \frac{-P_i \cdot e_{net} + M_{g0.max}}{I_{net}} \cdot e_{net} = -9\ MPa$

$\varepsilon_{p0i} := \frac{P_i}{E_p \cdot A_p} - \frac{\sigma_{cpi}}{E_{cm}} = 5.62 \cdot 10^{-3}$

$P_{0i} := E_p \cdot \varepsilon_{p0i} \cdot A_p = 658\ kN$

4.2 Before grouting (tensioning)

$\sigma_{cti} := \frac{-P_{0i}}{A_{net}} + \frac{-P_{0i} \cdot e_{net} + M_{g0.max}}{I_{net}} \cdot -x_{net} = 2.6\ MPa$ $\sigma_{cti.max7} = 2.6\ MPa$ $\sigma_{cti} \le \sigma_{cti.max7} = 1$

$\sigma_{cci} := \frac{-P_{0i}}{A_{net}} + \frac{-P_{0i} \cdot e_{net} + M_{g0.max}}{I_{net}} \cdot \left(h - x_{net}\right) = -11.1\ MPa$ $\sigma_{cci.max7} = 15.2\ MPa$ $\sigma_{cci.max7} \ge \left|\sigma_{cci}\right| = 1$

4.3 After grouting

$RH := 50$

Relaxation class 2

$\chi_{1000} = 2.5\%$ $\mu := 0.7$

$\chi_t(t) := 0.66 \cdot \chi_{1000} \cdot e^{9.1\,\mu} \cdot \left(\frac{t}{1000}\right)^{0.75 \cdot (1-\mu)} \cdot 10^{-3}$

$t_\infty := 500000$ $t := 100 \cdot 24 = 2400$

$\chi_\infty := \chi_t(t_\infty) = 0.039$ $\chi_t := \chi_t(t) = 0.0117$

Shrinkage

$\varepsilon_{cdi} := 0.280 \cdot 10^{-3}$ Class N

$\beta_{RH} := 1.36$ RH = 50%

$$u := 2 \cdot \left(\frac{b_{tf}}{2} + h_{tf} + \left(h_w - h_{t.trig} - h_{b.trig} \right) + h_{bf} + \frac{b_{bf}}{2} + \sqrt{b_{t.trig}{}^2 + h_{t.trig}{}^2} + \sqrt{b_{b.trig}{}^2 + h_{b.trig}{}^2} \right) = 2.2 \ m$$

$$h_0 := \frac{2 \cdot A_c}{u} = 130 \ mm$$

$$k_h := \left\| \begin{array}{l} \text{if } h_0 < 0.1 \cdot m \\ \quad \| 1 \\ \text{else if } 0.1 \cdot m \le h_0 \le 0.2 \cdot m \\ \quad \left\| 1.0 - 0.15 \cdot \frac{\left(h_0 - 100 \cdot mm \right)}{100 \cdot mm} \right. \\ \text{else if } 0.2 \cdot m \le h_0 \le 0.3 \cdot m \\ \quad \left\| \left(0.85 - 0.1 \cdot \frac{\left(h_0 - 200 \cdot mm \right)}{100 \cdot mm} \right) \right. \\ \text{else if } 0.3 \cdot m \le h_0 \le 0.5 \cdot m \\ \quad \left\| \left(0.75 - 0.05 \cdot \frac{\left(h_0 - 300 \cdot mm \right)}{200 \cdot mm} \right) \right. \\ \text{else if } h_0 > 0.5 \cdot m \\ \quad \| 0.7 \end{array} \right\| = 0.96$$

$\varepsilon_{cd\infty} := k_h \cdot \beta_{RH} \cdot \varepsilon_{cdi} = 3.64 \cdot 10^{-4}$

$\varepsilon_{ca\infty} := 0.1 \cdot 10^{-3}$

$\varepsilon_{cs\infty} := \varepsilon_{cd\infty} + \varepsilon_{ca\infty} = 4.64 \cdot 10^{-4}$

$t := 100$ $t_s := 4$

$$\beta_{ds} := \frac{t - t_s}{t - t_s + 0.04 \cdot \sqrt{\left(\frac{h_0}{mm} \right)^3}} = 0.62$$

$\beta_{as} := 1 - e^{-0.2 \, t^{0.5}} = 0.86$

$\varepsilon_{cs} := \beta_{ds} \cdot \varepsilon_{cd\infty} + \beta_{as} \cdot \varepsilon_{ca\infty} = 3.12 \cdot 10^{-4}$

$F_{cs.p} := E_p \cdot \varepsilon_{cs} \cdot A_p = 36.5 \ kN$

$F_{cs.s} := E_s \cdot \varepsilon_{cs} \cdot A_s = 87.7 \ kN$

$F'_{cs.s} := E_s \cdot \varepsilon_{cs} \cdot A'_s = 87.7\ kN$

Creep

$$\varphi_{RH} := \left(1 + \frac{1 - RH\%}{0.1 \cdot \sqrt[3]{\frac{h_0}{mm}}} \cdot \left(\frac{35 \cdot MPa}{f_{cm}}\right)^{0.7}\right) \cdot \left(\frac{35 \cdot MPa}{f_{cm}}\right)^{0.2} = 1.77$$

$$\beta_{fcm} := \frac{16.8}{\sqrt{\frac{f_{cm}}{MPa}}} = 2.5$$

$$h_0 := \frac{2 \cdot A_c}{u} = 130\ mm$$

$t = 100$ $t_0 := 28$

$$\beta_{t0} := \frac{1}{0.1 + t_0^{0.2}} = 0.49$$

$$\alpha_3 := \left(\frac{35}{\frac{f_{cm}}{MPa}}\right)^{0.5} = 0.9$$

$$\beta_H := min\left(1.5 \cdot \left(1 + \left(0.012 \cdot RH\right)^{18}\right) \cdot \frac{h_0}{mm} + 250 \cdot \alpha_3, 1500 \cdot \alpha_3\right) = 418.9$$

$$\beta_c := \left(\frac{t - t_0}{\beta_H + t - t_0}\right)^{0.3} = 0.6$$

$\varphi_0 := \varphi_{RH} \cdot \beta_{fcm} \cdot \beta_{t0} = 2.2$

$\varphi := \varphi_0 \cdot \beta_c = 1.2$

$$\alpha_{s.ef} := \frac{E_s}{E_{cm}} \cdot (1 + \varphi) = 13.1$$

$$\alpha_{p.ef} := \frac{E_p \cdot (1 - \chi_t)}{E_{cm}} \cdot (1 + \varphi) = 12.6$$

4.4 Effective sectional constants

$A_{I.ef} := A_c + (\alpha_{p.ef} - 1) \cdot A_p + (\alpha_{s.ef} - 1) \cdot A_{s.tot} = 0.18\ m^2$

$$x_{I.ef} := \frac{A_{tf} \cdot y_{tf} + A_w \cdot y_w + A_{bf} \cdot y_{bf} + 2 \cdot A_{b.trig} \cdot y_{b.trig} + 2 \cdot A_{b.trig} \cdot y_{b.trig} + (\alpha_{p.ef} - 1) \cdot A_p \cdot y_{duct.I} + (\alpha_{s.ef} - 1) \cdot A'_s \cdot d' + (\alpha_{s.ef} - 1) \cdot A_s \cdot d}{A_{I.ef}} = 332\ mm$$

$$I_{tf.I.ef} := \frac{b_{tf} \cdot h_{tf}^3}{12} + A_{tf} \cdot (x_{I.ef} - y_{tf})^2 \qquad \frac{b_{b.trig} \cdot h_{b.trig}^3}{36} = 0.000000036892\ m^4$$

$$I_{w.I.ef} := \frac{b_w \cdot h_w^3}{12} + A_w \cdot (x_{I.ef} - y_w)^2$$

$$I_{bf.I.ef} := \frac{b_{bf} \cdot h_{bf}^3}{12} + A_{bf} \cdot (x_{I.ef} - y_{bf})^2$$

$$I_{t.trig.I.ef} := \frac{b_{t.trig} \cdot h_{t.trig}^3}{36} + A_{t.trig} \cdot (x_{I.ef} - y_{t.trig})^2 = 44024485.5\ mm^4$$

$$I_{b.trig.I.ef} := \frac{b_{b.trig} \cdot h_{b.trig}^3}{36} + A_{b.trig} \cdot (x_{I.ef} - y_{b.trig})^2 = 34409593.3\ mm^4$$

$$I_{I.ef} := I_{tf.I.ef} + I_{w.I.ef} + I_{bf.I.ef} + 2 \cdot I_{t.trig.I.ef} + 2 \cdot I_{b.trig.I.ef} + (\alpha_{p.ef} - 1) \cdot A_p \cdot (y_{duct.I} - x_{I.ef})^2 = 0.006\ m^4$$

$e_{p.ef} := d_p - x_{I.ef} = 224\ mm$

$e_{s.ef} := d - x_{I.ef} = 272\ mm$

$M_{qt.max} = 249\ kN \cdot m$

$e'_{s.ef} := x_{I.ef} - d' = 296\ mm$

$$\sigma_{cc.t} := \frac{-(1-\chi_t) \cdot (P_{0i} - F_{cs.p}) + F_{cs.s} - F'_{cs.s}}{A_{I.ef}} + \frac{-(1-\chi_t) \cdot (P_{0i} - F_{cs.p}) \cdot e_{p.ef} + F_{cs.s} \cdot e_{s.ef} - F'_{cs.s} \cdot e'_{s.ef} + M_{g0.max} + M_{qt.max}}{I_{I.ef}} \cdot -x_{I.ef} = -10.4\ MPa$$

$$\sigma_{ct.t} := \frac{-(1-\chi_t) \cdot (P_{0i} - F_{cs.p}) + F_{cs.s} - F'_{cs.s}}{A_{I.ef}} + \frac{-(1-\chi_t) \cdot (P_{0i} - F_{cs.p}) \cdot e_{p.ef} + F_{cs.s} \cdot e_{s.ef} - F'_{cs.s} \cdot e'_{s.ef} + M_{g0.max} + M_{q.max}}{I_{I.ef}} \cdot (h - x_{I.ef}) = 3.2\ MPa$$

$\sigma_{cc\infty.max} = 26.1\ MPa$ $\quad \sigma_{cc\infty.max} > |\sigma_{cc.t}| = 1$

$\sigma_{ct\infty.max} = 3.2\ MPa$ $\quad \sigma_{ct\infty.max} > \sigma_{ct.t} = 1$ $\quad \frac{\sigma_{ct\infty.max}}{\sigma_{ct.t}} = 1.02$ Cracking will start at P_{qp}=83kN

$\sigma_{ct.t} = 3.2\ MPa$

$$\sigma_{cp.t} := \frac{\begin{matrix} -(1-\chi_t)\cdot(P_{0i}-F_{cs.p}) \\ +F_{cs.s}-F'_{cs.s} \end{matrix}}{A_{I.ef}} + \frac{\begin{matrix} -(1-\chi_t)\cdot(P_{0i}-F_{cs.p})\cdot e_{p.ef} \\ +F_{cs.s}\cdot e_{s.ef}-F'_{cs.s}\cdot e'_{s.ef} \\ +M_{g0.max}+M_{qt.max} \end{matrix}}{I_{I.ef}} \cdot (d_p - x_{I.ef}) = 1.4\ MPa$$

$$\sigma_{p0.t} := \frac{(1-\chi_t)\cdot(P_{0i}-F_{cs.p})}{A_p} + \alpha_{p.ef}\cdot\sigma_{cp.t} = 1041\ MPa$$

$$\varepsilon_{p0.t} := \frac{\sigma_{p0.t}}{E_p} = 5.3\cdot10^{-3}$$

$$\Delta\varepsilon_p := \varepsilon_{pd} - \varepsilon_{p0.t} = 3.6\cdot10^{-3}$$

4.5 Moment capacity

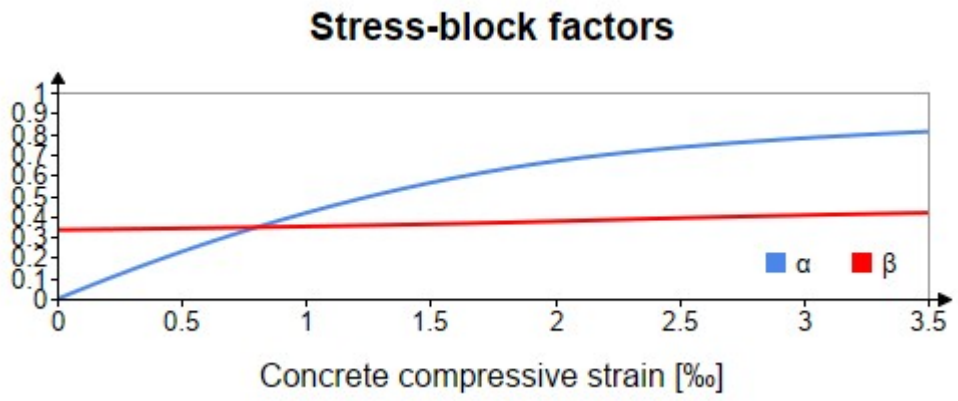

$\varepsilon_{cc} := \varepsilon_{cu} = 3.5\cdot10^{-3}$ $\quad \alpha := \alpha_R(\varepsilon_{cc}) = 0.81$ $\quad \beta := \beta_R(\varepsilon_{cc}) = 0.42$

$x := 100\ mm$

$$x := \mathbf{root}\left(\alpha\cdot f_{cm}\cdot b_{tf}\cdot x + \frac{x-d'}{x}\cdot\varepsilon_{cc}\cdot E_s\cdot A'_s - f_{p0.1m}\cdot A_p - f_{ym}\cdot A_s, x\right) = 104\ mm$$

$z := d - \beta\cdot x = 561\ mm$

$x < h_{tf} = 1$

$\varepsilon'_s := \frac{x-d'}{x}\cdot\varepsilon_{cc} = 2.3\cdot10^{-3}$ $\quad \varepsilon_{sy} = 2.75\cdot10^{-3}$ $\quad \varepsilon'_s < \varepsilon_{sy} = 1$

$\varepsilon_s := \frac{d-x}{x}\cdot\varepsilon_{cc} = 1.7\cdot10^{-2}$ $\quad \varepsilon_{sy} = 2.75\cdot10^{-3}$ $\quad \varepsilon_s < \varepsilon_{sy} = 0$

$\varepsilon_p := \frac{d_p-x}{x}\cdot\varepsilon_{cc} + \varepsilon_{p0.t} = 2\cdot10^{-2}$ $\quad \varepsilon_{p0.1m} = 9\cdot10^{-3}$ $\quad \varepsilon_p > \varepsilon_{p0.1m} = 1$

$M_{Rd} := \alpha \cdot f_{cm} \cdot b_{tf} \cdot x \cdot \left(d_p - \beta \cdot x\right) + \varepsilon'_s \cdot E_s \cdot A'_s \cdot \left(d_p - d'\right) + f_{ym} \cdot A_s \cdot \left(d - d_p\right) = 976\ kN \cdot m$

$M_{Ed.max} = 928\ kN \cdot m$

$M_{Rd} \geq M_{Ed.max} = 1$

$\frac{M_{Ed.max}}{M_{Rd}} = 0.95$

Assumed to crack at just at the ULS force

Minimum reinforcement amount

$A_{s.min} := 0.26 \cdot \frac{f_{ctm}}{f_{ym}} \cdot b_w \cdot d = 139\ mm^2$ $A_{s.max} := 0.04 \cdot A_c = 5642\ mm^2$

$A_s = 1407\ mm^2$ $A_{s.min} \leq A_s \leq A_{s.max} = 1$

Shear between web and flanges

$\Delta x := \frac{l}{4} = 2\ m$

$F_{c1} := \frac{M_{Ed}\left(\Delta x\right)}{z} = 1108\ kN$

$\Delta F_1 := \frac{b_{tf} - b_w}{2 \cdot b_{tf}} \cdot F_{c1} - \frac{V_{Ed}\left(\Delta x\right)}{2} = 140.8\ kN$

$v_{Ed1} := \frac{\Delta F_1}{h_{tf} \cdot \Delta x} = 0.6\ MPa$ $0.4 \cdot f_{ctm} = 1.3\ MPa$ $v_{Ed1} < 0.4 \cdot f_{ctm} = 1$

$F_{c2} := \frac{M_{Ed.max}}{z} = 1656\ kN$

$\Delta F_2 := \frac{b_{tf} - b_w}{2 \cdot b_{tf}} \cdot \left(F_{c2} - F_{c1}\right) = 146\ kN$

$v_{Ed2} := \frac{\Delta F_2}{h_{tf} \cdot \Delta x} = 0.6\ MPa$ $0.4 \cdot f_{ctm} = 1.3\ MPa$ $v_{Ed2} < 0.4 \cdot f_{ctm} = 1$

4.6 Crack width

$x_{II} = 521\ mm$

$A_{cc} := b_{tf} \cdot h_{tf} + 2 \cdot A_{t.trig} + b_w \cdot \left(x_{II} - h_{tf}\right) = 0.101\ m^2$

$A_{II} := A_{cc} + \left(\alpha_s - 1\right) \cdot A'_s + \alpha_s \cdot A_s + \alpha_p \cdot A_p = 0.119\ m^2$

$$x_{tp} := \frac{\frac{b_{tf} \cdot h_{tf}^2}{2} + b_w \cdot \left(x_{II} - h_{tf}\right) \cdot \left(\frac{x_{II} - h_{tf}}{2} + h_{tf}\right) + 2 \cdot A_{t.trig} \cdot \left(h_{tf} + \frac{h_{t.trig}}{2}\right) + \left(\left(\alpha_s - 1\right)\right) \cdot A'_s \cdot d' + \alpha_s \cdot A_s \cdot d + \alpha_p \cdot A_p \cdot d_p}{A_{II}} = 243\ mm$$

$$I_{II} := \frac{b_{tf} \cdot h_{tf}^3}{12} + b_{tf} \cdot h_{tf} \cdot \left(\frac{h_{tf}}{2} - x_{tp}\right)^2 + \frac{b_w \cdot \left(x_{II} - h_{tf}\right)^3}{12} + b_w \cdot \left(x_{II} - h_{tf}\right) \cdot \left(\frac{x_{II} - h_{tf}}{2} + h_{tf} - x_{tp}\right)^2 + 2 \cdot \left(\frac{b_{t.trig} \cdot h_{t.trig}^3}{36} + A_{t.trig} \cdot \left(x_{tp} - y_{t.trig}\right)^2\right) + \left(\alpha_s - 1\right) \cdot A'_s \cdot \left(x_{tp} - d'\right)^2 + \alpha_s \cdot A_s \cdot \left(d - x_{tp}\right)^2 + \alpha_p \cdot A_p \cdot \left(d_p - x_{tp}\right)^2 = 0.0042\ m^4$$

$e_{II} := d_p - x_{tp} = 312\ mm$

$$\sigma_c(z) := \frac{-P_i}{A_{II}} + \frac{-P_i \cdot e_{II} + M_{qp.max}}{I_{II}} \cdot z$$

$\sigma_c\left(x_{II} - x_{tp}\right) = 0.1\ MPa$ $\sigma_c\left(-x_{tp}\right) = -9.9\ MPa$ $\sigma_s := \alpha_s \cdot \sigma_c\left(d - x_{tp}\right) = 9.7\ MPa$

$a_y := c + \frac{\phi}{2} = 28\ mm$

$h_{c.eff} := min\left(a_y + 5 \cdot \phi, 10 \cdot \phi, 3.5 \cdot a_y, h - x_{II}, \frac{h}{2}\right) = 98\ mm$ $A_{eff} := h_{c.eff} \cdot b_w = 0.01\ m^2$

$\xi := 0.5$ $\xi_1 := \sqrt{\xi \cdot \frac{\phi}{\phi_p}} = 0.7$

$\rho_{p.ef} := \frac{A_s + \xi_1 \cdot A_p}{A_{eff}} = 0.12$

$k_{fl} := \frac{h - h_{c.eff}}{h} = 0.8$ $k_b := 0.9$ $k_w := 1.7$ $k_{1r} := \frac{h - x_{II}}{h - a_y - x_{II}} = 1.3$

$s_{r.max} := k_w \cdot k_{1r} \cdot min\left(\left(1.5 \cdot c + \frac{k_{fl} \cdot k_b}{7.2} \cdot \frac{\phi}{\rho_{p.ef}}\right), \frac{1.3}{k_w} \cdot \left(h - x_{II}\right)\right) = 97\ mm$

$k_t := 0.6$

$$\Delta\varepsilon := max\left(\frac{\sigma_s - k_t \cdot \frac{f_{ctm}}{\rho_{p.ef}} \cdot \left(1 + \alpha_s \cdot \rho_{p.ef}\right)}{E_s}, \left(1 - k_t\right) \cdot \frac{\sigma_s}{E_s}\right) = 19.5 \cdot 10^{-6}$$

$w_k := \Delta\varepsilon \cdot s_{r.max} = 0.0019\ mm$

4.7 Shear capacity

$P_d := \sigma_{p0.t} \cdot A_p = 625\ kN$ $\alpha_p := atan\left(\frac{e_p}{l_1}\right) = 4.4\ °$

$V_{ipd} := P_d \cdot tan\left(\alpha_p\right) = 47.9\ kN$

$V_{Ed.net} := V_{Ed.max} - V_{ipd} = 266.2\ kN$

$\tau_{Ed.net} := \frac{V_{Ed.net}}{b_w \cdot z} = 3.2\ MPa$ $\tau_{Ed} := \frac{V_{Ed.max}}{b_w \cdot z} = 3.7\ MPa$

Shear capacity of cracked concrete without shear reinforcement

$a_{cs} := \frac{M_{Ed.max}}{V_{Ed.max}} = 3\ m$

$k_1 := min\left(\frac{0.7}{a_{cs}} \cdot \left(e_p + \frac{d}{3}\right) \cdot \frac{A_c}{b_w \cdot z}, 0.25 \cdot \frac{A_c}{b_w \cdot z}\right) = 0.2$

$k_{vp} := 1 + \frac{-P_i \cdot d}{V_{Ed.max} \cdot 3 \cdot a_{cs}} = 0.9$

$d := \frac{d^2 \cdot A_s + {d_p}^2 \cdot A_p}{d \cdot A_s + d_p \cdot A_p} = 590.4\ mm$

$\rho_l := \frac{d \cdot A_s + d_p \cdot A_p}{b_w \cdot d^2} = 0.0223$

$\sigma_{cp} := min\left(\frac{P_i}{A_c}, 0.2 \cdot f_{cm}\right) = 4.4\ MPa$

$\tau_{Rdc.0} := 0.66 \cdot \left(100 \cdot \rho_l \cdot \frac{f_{cm}}{MPa} \cdot \frac{40\ mm}{d}\right)^{\frac{1}{3}}\ MPa = 1.2\ MPa$

$\tau_{Rd.c} := \tau_{Rdc.0} + k_1 \cdot \sigma_{cp} = 2\ MPa$

$\frac{\tau_{Ed.net}}{\tau_{Rd.c}} = 158\%$

Shear capacity of cracked concrete with shear reinforcement

$\theta := 21.8\ deg$

$s_w := 260\ mm$

$A_{sw} := \frac{\phi_w^{\ 2}}{4} \cdot \pi = 50\ mm^2$

$\rho_w := \frac{2 \cdot A_{sw}}{b_w \cdot s_w} = 0.00258$

$\tau_{Rd.sy} := \rho_w \cdot f_{ym} \cdot cot(\theta) = 3.5\ MPa$

$\frac{\tau_{Ed.net}}{\tau_{Rd.sy}} = 89\%$

$n_w := 2 \cdot \left(\frac{l_1}{s_w} + 1 \right) = 25.1$

$l_w = 1.5\ m$

Minimum shear reinforcement amount

$\rho_{w.min} := 0.08 \cdot \frac{\sqrt{\frac{f_{cm}}{MPa}}}{\frac{f_{ym}}{MPa}} = 0.001$

$\alpha := 90\ °$

$s_{w.max} := \frac{2 \cdot A_{sw}}{b_w \cdot sin(\alpha) \cdot \rho_{w.min}} = 699\ mm$

$s_{l.max} := 0.75 \cdot d \cdot (1 + cot(\alpha)) = 443\ mm$

$s_w < min(s_{w.max}, s_{l.max}) = 1$

4.8 Anchorage zone

Calculated for XM20 achorage from the manufacturer CCL.

$\gamma_p := 1.2$

$P := \gamma_p \cdot P_{i.1} = 768\ kN$

$0.2 \cdot h = 128\ mm$

$\phi_{p.achorage} := 105\ mm$

$\sigma_{cc} := \frac{P}{\left(\frac{\phi_{p.achorage}}{2}\right)^2 \cdot \pi} = 88.7\ MPa \qquad f_{cm} = 43.5\ MPa \qquad 3 \cdot f_{cm} = 130.5\ MPa$

Vertical reinforcement

$a := \phi_{p.achorage} = 105\ mm \qquad h = 640\ mm \qquad b := \frac{h}{2} = 320\ mm$

$T := \frac{1}{4} \cdot \frac{b - a}{b} \cdot P = 129\ kN$

$A_v := \frac{T}{f_{ym}} = 235\ mm^2$

$n_v := ceil\left(\frac{A_v}{2 \cdot \frac{(8\ mm)^2}{4} \cdot \pi}\right) = 3$

4.9 Buckling

$l_0 := l_{tot} = 8500\ mm$

$i := \sqrt{\frac{I_c}{A_c}} = 210.4\ mm$

$\lambda := \frac{l_0}{i} = 40.4$

$n := \frac{P}{f_{cm} \cdot A_c} = 0.13$

$\lambda_{lim} := \frac{10.8}{\sqrt{n}} = 30.5$

$A := \frac{1}{1 + 0.2 \cdot \varphi} = 0.8$

$\omega := \frac{A_s \cdot f_{ym}}{A_c \cdot f_{cm}} = 0.1$

$B := \sqrt{1 + 2 \cdot \omega} = 1.12$

$C := 0.7$

$\lambda_{lim} := \frac{20 \cdot A \cdot B \cdot C}{\sqrt{n}} = 35.5$ $\lambda < \lambda_{lim} = 0$

B Concrete mixes

Table B.1: Concrete mix for Conventional concrete (strength class C40/50 and vct 0,40).

Delmaterial	**40/50 08 vct 0,40 SF1 Std. Cem** [kg/m^3]
Byggcement CEM II/A–LL 42,5R	468
Slagg Bremen	—
0/4 sand	765
0/4 Kross (Swerock Arendal)	170
4/8 (Swerock Arendal)	685
Kalkfiller (Limus 40)	103
MasterGlenium 51/18	5,3 (0,9 torrsubstans)
MasterEase	1,8 (0,5 torrsubstans)
Effektivt vatten	186 (inkl tillsatsmedel)
Dramix 4D 65/35	—

Table B.2: Concrete mix for low-CO_2 concrete with fibres (strength class C40/50 and vct 0,40).

Delmaterial	**40/50 08 vct 0,40 SF1 Std. Cem ThomaGrön 4** [kg/m^3]
Byggcement CEM II/A–LL 42,5R	230,2
Slagg Bremen	232,2
0/4 sand	753
0/4 Kross (Swerock Arendal)	163
4/8 (Swerock Arendal)	680
Kalkfiller (Limus 40)	118
MasterGlenium 51/18	3,1 (0,5 torrsubstans)
MasterEase	0,9 (0,3 torrsubstans)
Effektivt vatten	186 (inkl tillsatsmedel)
Dramix 4D 65/35	40,5

Table B.3: Concrete mix for low-CO_2 concrete without fibres (strength class C40/50 and vct 0,40)

Delmaterial	**40/50 08 vct 0,40 SF1 Std. Cem ThomaGrön 4** [kg/m^3]
Byggcement CEM II/A–LL 42,5R	232,7
Slagg Bremen	236,6
0/4 sand	763
0/4 Kross (Swerock Arendal)	167
4/8 (Swerock Arendal)	689
Kalkfiller (Limus 40)	97,5
MasterGlenium 51/18	2,6 (0,5 torrsubstans)
MasterEase	1,0 (0,3 torrsubstans)
Effektivt vatten	187 (inkl tillsatsmedel)
Dramix 4D 65/35	—

C Reinforcement Drawing

Reinforcement drawings produced in AutoCAD.

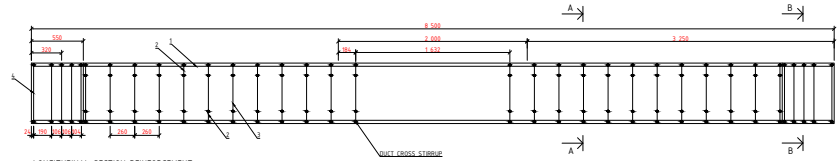

LONGITUDINAL SECTION REINFORCEMENT

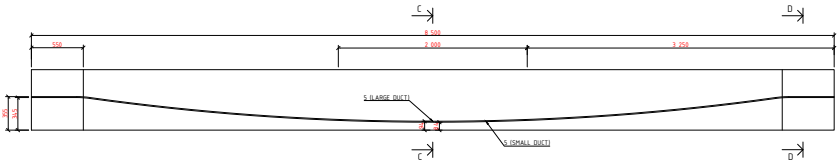

LONGITUDINAL SECTION POST-TENSIONING DUCT

NO	AMOUNT	DESCRIPTION	LENGTH (mm)
1	14	LONGITUDINAL Φ16	8400
2	68	TOP/BOTTOM STIRRUP Φ8	860
3	34	WEB STIRRUP Φ8	1540
4	10	ANCHORAGE STIRRUP Φ8	1880

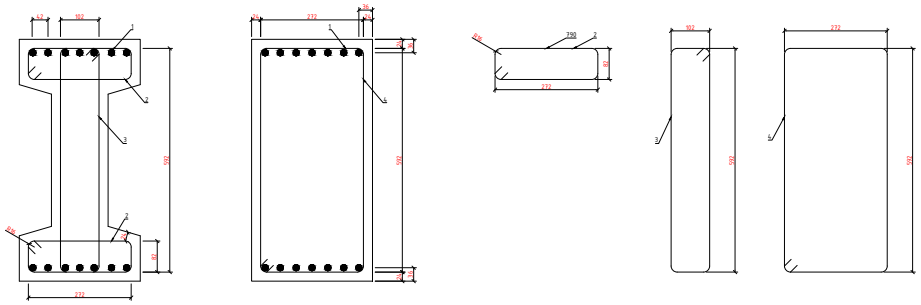

SECTION A-A

SECTION B-B

REINFOCEMENT DRAWING

2026-01-30

ELISABETH BRUHN

STINA DURLING

D Form Drawing

Form drawings produced in AutoCAD.

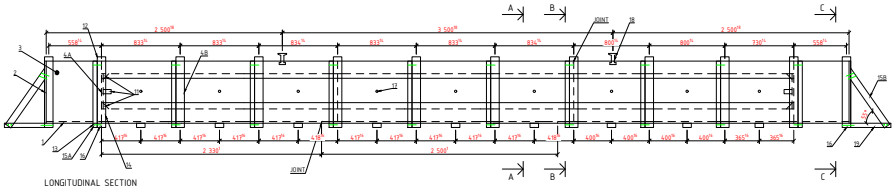

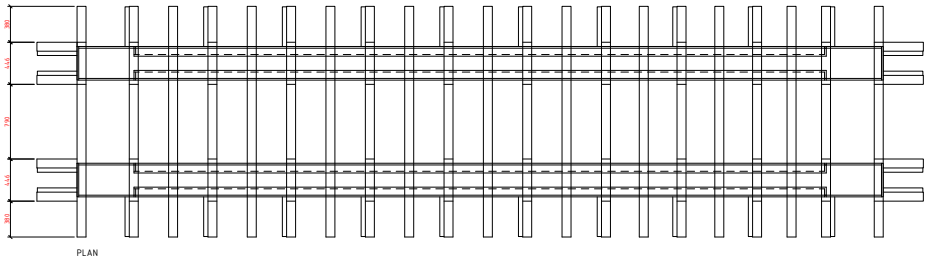

NO	AMOUNT A	AMOUNT B	DESCRIPTION
1	2	1	BOTTOM
2	2		EDGE BOX SIDE
3	4		BOX SIDE
4	4	16	BOX SIDE INSIDE I-PART
5	4	2	BEAM SIDE BOTTOM
6	8	4	BEAM SIDE TRIANGLE
7	4	2	BEAM SIDE MIDDLE
9	4	2	BEAM SIDE TOP
11	12		SCREW AREA BOX/BEAM
12	10 el. 12		TOP
13			SCREW
14	24		STUD
15	20	4	STAG
16	21		BASE STUD LONG
17	9		FORM TIE
18	2		SPHERICAL HEAD ANCHORS
19	4		BASE STUD SHORT

FORM DRAWING

2026-01-30

ELISABETH BRUHN

STINA DURLING

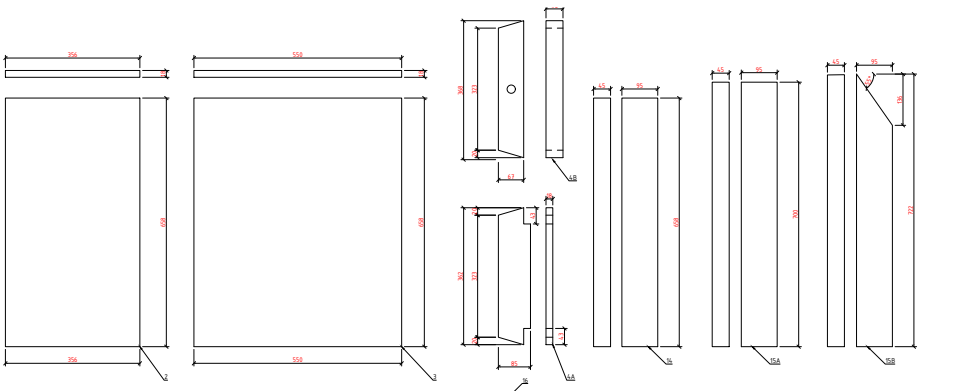

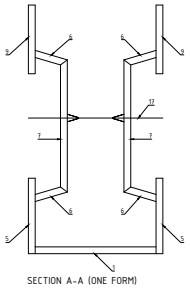

SECTION A-A (ONE FORM)

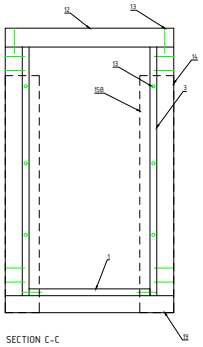

SECTION C-C

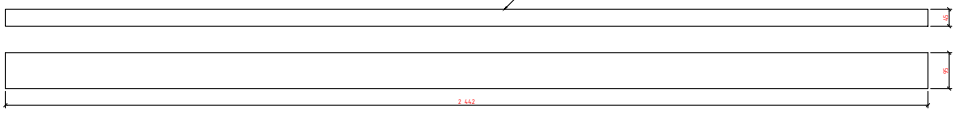

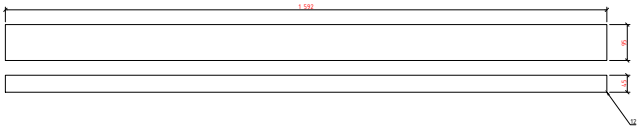

FORM DRAWING
2026-01-30
ELISABETH BRUHN
STINA DURLING

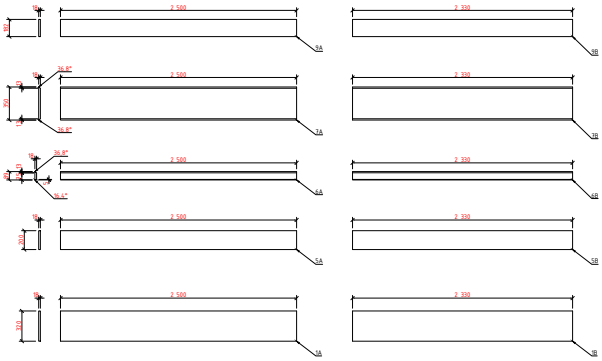

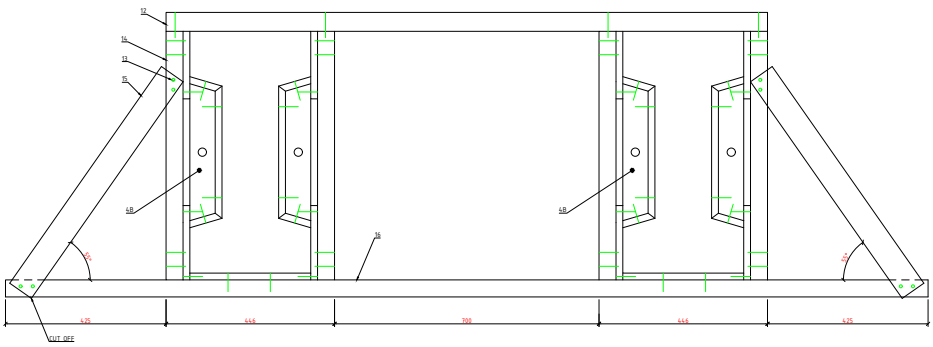

SECTION B-B

DEPARTMENT OF ARCHITECTURE AND
CIVIL ENGINEERING
CHALMERS UNIVERSITY OF TECHNOLOGY
Gothenburg, Sweden 2026
www.chalmers.se

CHALMERS
UNIVERSITY OF TECHNOLOGY